Characterisation and Error Analysis of H_2O Retrievals from the UARS Microwave Limb Sounder Experiment

Martin R. Suttie

PhD Thesis

1995

Department of Meteorology
University of Edinburgh

Declaration

I hereby declare that this thesis has been composed by myself and the work it contains is my own.

I dedicate this thesis to my parents.

Acknowledgments

I thank R.S. Harwood for his guidance, supervision, encouragement and support throughout the duration of this work. I gratefully acknowledge the comments of H.C. Pumphrey on draft versions of this thesis and thank him for his assistance in the printing and submission of the thesis. I also acknowledge the valuable comments from, and the numerous useful discussions with, H.C. Pumphrey and M.J. Filipiak throughout the duration of the work. I wish to thank J.W. Waters, L. Froidevaux, W.G. Read and T.A. Lungu of the Jet Propulsion Laboratory, for their cooperation and assistance concerning details of the MLS instrument and retrieval scheme. I thank my friends for beer and banter. Finally, I thank my parents; without their enduring support, both moral and financial, this thesis would not exist.

Contents

1 Introduction 12

1.1 Introduction and Aims of the thesis 12

1.2 Upper Atmosphere Research Satellite 13

1.3 UARS MLS Experimental Objectives 15

1.4 UARS MLS Instrument Characteristics 17

2 Atmospheric Limb Sounding and Retrieval 22

2.1 Introduction to Limb Sounding 22

2.1.1 Geometry of Limb Sounding 23

2.1.2 Radiative Transfer 25

2.2 Retrieval Problem 28

2.2.1 Introduction 28

2.2.2 Optimal Estimation 30

2.2.3 MLS Retrieval Scheme 32

2.3 Characterisation and Error Analysis 34

2.3.1 Characterisation of the Retrieval 34

2.3.2 Error Analysis 35

3 Characterisation and Error Analysis of UARS MLS 183 GHz H_2O Retrievals 41

3.1 Introduction 41

3.2 Retrieval Contribution Functions 47

3.3 Averaging kernels and *a priori* contribution 51

3.4 Error Analysis 57
3.4.1 Random errors 57
3.4.2 Systematic errors 66
3.4.3 Summary of Error Analysis 71
3.5 Chapter Summary 74

4 Possible improvements to H_2O retrievals in the lower stratosphere 76
4.1 Introduction 76
4.2 Proposed method to improve retrievals in the lower stratosphere 84
4.2.1 Cause of loss of measurement information 84
4.2.2 Development of channel-dependent opacity criterion . . 86
4.3 Test retrievals 89
4.3.1 With simulated radiances 89
4.3.2 With MLS measured radiances 94
4.4 Summary and Discussion 100

5 Possibility of retrieving H_2O at higher vertical resolution 103
5.1 Introduction 103
5.2 With nominal MLS scan pattern 104
5.2.1 Nominal retrieval grid 105
5.2.2 Retrieval grid of resolution 2 x nominal 110
5.2.3 Retrieval grid of resolution 4 x nominal 114
5.3 With simulated high resolution scan pattern 119
5.3.1 Nominal retrieval grid 120
5.3.2 Retrieval grid of resolution 2 x nominal 125
5.3.3 Retrieval grid of resolution 4 x nominal 129
5.4 Discussion and Summary 133

6 Discussion and Further Work 138

A Transformation of Optimal Estimation Equations 142

List of Figures

1.1 Signal-flow block diagram of the MLS instrument 18

2.1 Geometry of limb sounding 23
2.2 Radiative transfer geometry 26

3.1 Calculated limb emission in the spectral region 182–187 GHz . 42
3.2 Measured limb radiance profiles for channels 1–8 of band 5 . . . 43
3.3 Measured limb radiance spectra for channels 1–8 of band 5 . . . 45
3.4 Influence functions for band 5 with respect to H_2O 46
3.5 H_2O contribution functions for band 5 50
3.6 Averaging kernels for H_2O retrieval 51
3.7 Vertical resolution of H_2O retrieval 53
3.8 Sensitivity of the H_2O retrieval to *a priori* 54
3.9 Eigenvectors of H_2O averaging kernel matrix 56
3.10 Random errors for H_2O retrieval 58
3.11 Error patterns for measurement noise 60
3.12 Precision estimates for H_2O. For meaning of lines see text. . . . 61
3.13 Smoothing error for H_2O retrieval 63
3.14 Error patterns for smoothing error 65
3.15 Systematic errors for H_2O retrieval 67
3.16 Errors for H_2O retrieval 72
3.17 Percentage errors for H_2O retrieval 72

4.1 Zonal mean error ratio for H_2O on 10th January 1992, 8th August 1992 and 30th August 1992 78

4.2 Temperature and Error ratio for H_2O at 46 hPa on 10th January 1992 80
4.3 Temperature and Error ratio for H_2O at 22 hPa on 10th January 1992 81
4.4 Averaging kernels for H_2O retrieval at high latitude during winter 82
4.5 Smoothing error for H_2O retrieval during polar winter and for typical mid-latitude 83
4.6 Effect of opacity criterion. Left panel for typical limb scan at mid-latitude, right panel for limb scan at high latitude in winter. The plots show the radiance measurements which are included in the retrieval (*) and those which are not (.) 85
4.7 Temperature and H_2O cross-sections, along part of an orbit, of assumed distributions based on smoothed versions of the MLS Version 3 retrievals on 17th September 1992 (UARS day 372). See text for details. 91
4.8 H_2O retrievals at 46 hPa based on simulated data. The plots are for a chosen orbit track which crosses over the southern polar region. Dotted line - scenario (a), dashed line - scenario (b), dash-dot line - scenario (c), solid line - true mixing ratio. See text for details. 92
4.9 H_2O retrievals at 22 hPa based on simulated data. The plots are for a chosen orbit track which crosses over the southern polar region. Dotted line - scenario (a), dashed line - scenario (b), dash-dot line - scenario (c), solid line - true mixing ratio. See text for details. 93
4.10 Temperature and H_2O cross-sections, along part of an orbit, for the MLS Version 3 retrieval on 30th August 1992 (UARS day 354). The white dashed lines represent the 0.5 contour for the error ratio. See text for details. 95

4.11 H_2O retrievals at 46 hPa based on measured radiances on 30th August 1992 (UARS day 354). The plots are for a chosen orbit track which crosses over the southern polar region. Solid line - scenario (a), dotted line - scenario (b), dashed line - scenario (c). See text for details. 96

4.12 H_2O retrievals at 22 hPa based on measured radiances on 30th August 1992 (UARS day 354). The plots are for a chosen orbit track which crosses over the southern polar region. Solid line - scenario (a), dotted line - scenario (b), dashed line - scenario (c). See text for details. 98

4.13 Mean retrieved profiles of H_2O within selected latitude bands for 30th August 1992. Solid line - scenario (a), dotted line - scenario (b), dashed line - scenario (c). See text for details. . . 99

4.14 Mean retrieved profiles of H_2O within selected latitude bands for 10th January 1992. Solid line - scenario (a), dotted line - scenario (b). See text for details. 100

5.1 Averaging kernels for H_2O retrieval on nominal grid. A correlation length scale of 5–6 km was assumed. 106

5.2 Vertical resolution of H_2O retrieval on nominal grid; (a) no inter-level correlations, (b) correlation length of 5–6 km. 107

5.3 Smoothing error for H_2O retrieval on nominal grid; (a) no inter-level correlations, (b) correlation length of 5–6 km. 108

5.4 Error due to measurement noise for H_2O retrieval on nominal grid; (a) no inter-level correlations, (b) correlation length of 5–6 km. 109

5.5 Total error for H_2O retrieval on nominal grid; (a) no inter-level correlations, (b) correlation length of 5–6 km. 110

5.6 Averaging kernels for H_2O retrieval on a grid of twice the nominal resolution. No inter-level correlations have been assumed. Alternate rows of the averaging kernel matrix are plotted. . . . 111

5.7 Averaging kernels for H_2O retrieval on a grid of twice the nominal resolution. A correlation length scale equivalent to 5–6 km has been assumed. Alternate rows of the averaging kernel matrix are plotted. 112
5.8 Vertical resolution of H_2O retrieval on a grid of twice the nominal resolution; (a) no inter-level correlations, (b) correlation length of 2.5–3 km, (c) correlation length of 5–6 km. 113
5.9 Total error for H_2O retrieval on a grid of twice the nominal resolution; (a) no inter-level correlations, (b) correlation length of 2.5–3 km, (c) correlation length of 5–6 km. 114
5.10 Selected averaging kernels for H_2O retrieval on a grid of four times the nominal resolution. No inter-level correlations have been assumed. 115
5.11 Selected averaging kernels for H_2O retrieval on a grid of four times the nominal resolution. A correlation length scale of 5–6 km has been assumed. 116
5.12 Vertical resolution of H_2O retrieval on a grid of four times the nominal resolution; (a) no inter-level correlations, (b) correlation length of 2.5–3 km, (c) correlation length of 5–6 km. 117
5.13 Total error for H_2O retrieval on a grid of four times the nominal resolution; (a) no inter-level correlations, (b) correlation length of 2.5–3 km, (c) correlation length of 5–6 km. 118
5.14 Averaging kernels for H_2O retrieval on nominal grid. Measurements from a limb scan of ~ 1.5 km resolution have been simulated. The integration time for each limb view is 1.8 seconds. A correlation length scale of 5–6 km has been assumed. 121
5.15 Vertical resolution of H_2O retrieval on nominal grid; (a) measurements on nominal MLS limb scan, (b) simulated measurements with integration time of 1.8 seconds on limb scan of resolution 1.5 km, (c) as for (b) but integration time of 0.4 seconds. 122

5.16 Smoothing error for H_2O retrieval on nominal grid; (a) measurements on nominal MLS limb scan, (b) simulated measurements with integration time of 1.8 seconds on limb scan of resolution 1.5 km, (c) as for (b) but integration time of 0.4 seconds. 123
5.17 Error due to measurement noise for H_2O retrieval on nominal grid; (a) measurements on nominal MLS limb scan, (b) simulated measurements with integration time of 1.8 seconds on limb scan of resolution 1.5 km, (c) as for (b) but integration time of 0.4 seconds. 124
5.18 Total error for H_2O retrieval on nominal grid; (a) measurements on nominal MLS limb scan, (b) simulated measurements with integration time of 1.8 seconds on limb scan of resolution 1.5 km, (c) as for (b) but integration time of 0.4 seconds. 125
5.19 Averaging kernels for H_2O retrieval on a grid of twice the nominal resolution. Measurements from a limb scan of ~ 1.5 km resolution have been simulated. The integration time for each limb view is 1.8 seconds. A correlation length scale of 5–6 km has been assumed. 126
5.20 Vertical resolution of H_2O retrieval on a grid of twice the nominal resolution; (a) measurements on nominal MLS limb scan, (b) simulated measurements with integration time of 1.8 seconds on limb scan of resolution 1.5 km, (c) as for (b) but integration time of 0.4 seconds. 127
5.21 Total error for H_2O retrieval on a grid of twice the nominal resolution; (a) measurements on nominal MLS limb scan, (b) simulated measurements with integration time of 1.8 seconds on limb scan of resolution 1.5 km, (c) as for (b) but integration time of 0.4 seconds. 128

5.22 Averaging kernels for H_2O retrieval on a grid of four times the nominal resolution. Measurements from a limb scan of ~ 1.5 km resolution have been simulated. The integration time for each limb view is 1.8 seconds. A correlation length scale of 5–6 km has been assumed. 130

5.23 Vertical resolution of H_2O retrieval on a grid of four times the nominal resolution; (a) measurements on nominal MLS limb scan, (b) simulated measurements with integration time of 1.8 seconds on limb scan of resolution 1.5 km, (c) as for (b) but integration time of 0.4 seconds. 131

5.24 Total error for H_2O retrieval on a grid of four times the nominal resolution; (a) measurements on nominal MLS limb scan, (b) simulated measurements with integration time of 1.8 seconds on limb scan of resolution 1.5 km, (c) as for (b) but integration time of 0.4 seconds. 132

List of Tables

1.1 Primary retrievals for MLS spectral bands 19

1.2 Positions and widths of MLS spectral channels. The position refers to the channel centre and is given as a frequency offset from the band centre. 20

1.3 Typical MLS scan pattern 21

3.1 Estimated precision and accuracy for MLS Version 3 H_2O retrievals 73

4.1 Relative response, ω_{p_i}, of the principal sideband and values of τ_{c_i} for channel-dependent opacity criterion equivalent to using channel-independent opacity criterion as for MLS Version 3 retrievals 88

Abstract

The Upper Atmosphere Research Satellite (UARS) was launched on 12th September 1991 carrying a payload to measure the chemistry, dynamics and energy balance of the middle atmosphere. The Microwave Limb Sounder (MLS) onboard UARS makes measurements of atmospheric thermal emission at millimetre wavelengths which are used to infer molecular abundances throughout the stratosphere and mesosphere. Measurements made at 183.3 GHz are used to retrieve concentrations of water vapour (H_2O). Measurements of water vapour on a global scale are of particular importance to the study of stratospheric photochemistry, radiation budget and dynamics. MLS provides approximately 19 months of near continuous water vapour measurements on a global scale.

A characterisation and error analysis, based on the formalism of *Rodgers, [1990]*, is performed for the UARS MLS 183 GHz H_2O retrievals. The useful vertical range for scientific studies with MLS Version 3 H_2O retrievals is found to be 22–0.2 hPa at high latitudes and 46–0.2 hPa elsewhere. For this vertical range, the estimated vertical resolution of the retrievals is 5–6 km. In the error analysis, estimates of the contributions of both random errors, including the smoothing error, and systematic uncertainties to the overall error in retrieved H_2O are produced.

It is found that the retrievals at 46 hPa and 22 hPa contain an increased contribution from the *a priori* information at high latitudes during the polar winter which is due to a corresponding loss of information from the radiance measurements. This is linked to the use of an *opacity criterion* which does

not permit radiance measurements which arise from optically thick limb paths to be included in the retrieval. A new opacity criterion is developed in an attempt to improve the retrieval at 46 hPa and 22 hPa. Test retrievals show that it is possible to reduce the contribution from the *a priori* information to an acceptable level, but at 22 hPa a systematic increase in H_2O mixing ratio occurs which requires further investigation.

The possibility of retrieving H_2O at higher vertical resolution than nominal is investigated. Firstly, retrievals using measurements from the nominal MLS limb scan are studied. A vertical resolution of 3–4 km is attainable in the range 15–0.7 hPa with a corresponding retrieval error of less than 1 ppmv. Also, an investigation into the possibility of using measurements from a limb scan of higher vertical resolution than the nominal MLS scan is performed. Measurements from a limb scan of resolution ~ 1.5 km are simulated. Using these measurements significantly reduces the retrieval error at 46 hPa and above and improves the vertical resolution of the retrieval above 0.46 hPa and between 46 hPa and 4.6 hPa.

Chapter 1

Introduction

1.1 Introduction and Aims of the thesis

This thesis is concerned with the characterisation and error analysis of the water vapour (H_2O) profiles retrieved from the Microwave Limb Sounder (MLS) experiment onboard the Upper Atmosphere Research Satellite (UARS). With any remote sensing system, it is important to identify the sources of possible uncertainty in the system and to try and quantify the effects of these various uncertainties on the final product. This is important for estimating the precision and accuracy of the retrieved quantity. Without reliable estimates of both the precision and accuracy, the data is of limited use.

Firstly, in the remainder of Chapter 1, some background to the Upper Atmosphere Research Satellite project is given, and then details of the Microwave Limb Sounder experiment are presented.

Chapter 2, on Atmospheric Limb Sounding and Retrieval, gives an introduction to the concept of limb sounding and a discussion of the radiative transfer involved, particularly in the microwave region of the electromagnetic spectrum. A brief discussion on the problem of retrieving atmospheric parameters from remote measurements is given and then a formal method of characterisation and error analysis of such retrievals is described.

In Chapter 3, a characterisation and error analysis of the H_2O retrievals

from the 183 GHz radiometer of the MLS is presented. This includes estimates of the precision, accuracy and vertical resolution of the retrieved profiles.

Chapters 4 and 5 both present investigations of possible improvements to the H_2O retrievals from MLS. In Chapter 4, a problem of increased error in the retrieved H_2O amount in the lower stratosphere at high latitudes during winter is investigated. In Chapter 5, the possibility of retrieving H_2O profiles at higher vertical resolution than nominal is studied.

Finally, in Chapter 6, a summary and discussion of the main findings of the thesis are presented along with an indication of important or interesting topics for further work.

1.2 Upper Atmosphere Research Satellite

Increasing concern in recent years about the sensitivity of the Earth's atmosphere to external influences associated with natural phenomena and to change arising from byproducts of various human activities highlighted the need for a long-term program of scientific research directed towards improving knowledge of the physical and chemical processes occurring in the Earth's atmosphere.

The Upper Atmosphere Research Satellite (UARS) [*Reber et al., 1993*], launched in September 1991, is an important mission aimed at improving our knowledge of the atmosphere above the troposphere, including the regions that are known to be especially susceptible to substantial change by external agents. The UARS is providing a focus for the investigation of scientific questions related to the chemistry, dynamics and overall energy balance of these regions. With the combination of UARS measurements, theoretical studies and model analyses, substantial progress should be made towards the understanding of the physical and chemical processes taking place in these regions.

The goals of the UARS project are : to understand the mechanisms that control upper atmosphere structure and variability; to understand the response of the upper atmosphere to natural and anthropogenic perturbations; to define the role of the upper atmosphere in climate and climate variability. To accom-

plish these goals, several areas of scientific study are addressed by the UARS program: energy input and losses in the upper atmosphere; global photochemistry of the upper atmosphere; dynamics of the upper atmosphere; coupling among processes; coupling between the upper and the lower atmosphere.

To investigate the study areas mentioned above, it is required to measure parameters such as energy inputs and vertical profiles of temperature, species concentrations and winds. It is defined by the UARS program basic requirements that the measurements should be of a global nature and be essentially continuous in time. For a low orbit satellite, such as UARS, this implies a global map every 24 hours. The data should also allow the detection of local solar time effects from the background of latitudinal and seasonal effects. The spatial resolution requirements are half a scale height in the vertical (~ 2.5 to 3 km) and 500 km in latitude, while requirements on longitude resolution range from 1000 km to zonal means, depending on the specific study and the time scale of the measurement. The 500 km latitude resolution translates into about 1 minute time resolution along the satellite track, defining the basic requirements for the atmospheric sensors to be capable of making vertical profile measurements in 1 minute or less.

The UARS observatory was launched on 12th September 1991 by the NASA Space Shuttle Discovery into a near-circular orbit at 585 km and an inclination of 57° to the equator. At this altitude and inclination, the remote sensing instruments which view at 90° to the spacecraft velocity vector can 'see' to 80° latitude, providing nearly global coverage. This inclination also produces a precession of the orbit plane such that all local solar times can be sampled in about 36 days, thus allowing resolution of diurnal atmospheric effects in a period which is short relative to seasonal effects. Also, due to the precession of the orbital plane, UARS performs a yaw manoeuvre every ~ 36 days to keep the Sun on the same side of the satellite.

The UARS observatory consists of 10 scientific instruments, one of which is the Microwave Limb Sounder (MLS) which uses millimeter-wavelength heterodyne spectroscopy to perform atmospheric measurements. The following

two sections describe the experimental objectives and the instrument characteristics of the MLS.

1.3 UARS MLS Experimental Objectives

The Microwave Limb Sounder (MLS) onboard UARS uses millimetre-wave heterodyne spectroscopy [*Waters, 1992*] to measure atmospheric thermal emission spectra by scanning the instrument field-of-view through the limb from above. These spectra can then be analysed to retrieve atmospheric profiles of molecular abundances, temperature and pressure. The technique of microwave limb sounding and the retrieval process are discussed in more detail in Chapter 2. The MLS experiment on UARS, the first satellite-borne microwave limb sounder, is led by the Jet Propulsion Laboratory (JPL) in the United States with collaboration from Edinburgh and Heriot-Watt Universities and the Rutherford Appleton Laboratory (RAL) in the United Kingdom. The instrument was developed by JPL with the 183 GHz radiometer subsystem being provided by Heriot-Watt and RAL. The Department of Meteorology at Edinburgh University is involved in the data analysis from the 183 GHz radiometer. Prior development of MLS included both aircraft [*Waters et al., 1979; 1980*] and balloon borne [*Waters et al., 1981; 1984; 1988a; Robbins et al., 1990*] instruments.

The primary measurement objectives of UARS MLS are profiles of chlorine monoxide, ClO from $\sim$15–45 km, ozone, O_3 from $\sim$15–80 km, water vapour, H_2O from $\sim$15–85 km, temperature from $\sim$30–60 km and pressure (for pointing information) from $\sim$30–60 km

It has long been recognised that chlorine can catalytically destroy stratospheric ozone [*Molina et al., 1974*] which is of great concern as industrial chlorofluorocarbons (CFC's), the major source of atmospheric chlorine, have led to a pronounced increase in stratospheric chlorine content [*WMO, 1990*].The discovery of the Antarctic ozone hole [*Farman et al., 1985*] and subsequent measurements of this phenomena have brought to light the important role of

stratospheric heterogeneous chemistry [*Molina et al., 1987a*] taking place in polar stratospheric clouds [*Solomon, 1990*] which leads to greatly enhanced chlorine and subsequent destruction of ozone. Observations of enhanced chlorine correlated with reduced ozone abundance have also been made in the Arctic [*Proffitt et al., 1990*] and are thought to be the result of similar heterogeneous processes. ClO is the rate limiting molecule in the chlorine destruction of ozone [*Molina et al., 1987b*], and its abundance gives a measure of the rate at which chlorine destroys ozone. UARS MLS is the first instrument to measure ClO on a global scale, and coupled with its measurements of stratospheric O_3, is providing an important contribution to the understanding and monitoring of ozone destruction by chlorine [*Waters et al., 1993, Manney et al. 1994*].

Water vapour plays an important role in radiative and photochemical processes in the middle atmosphere, while its distribution may shed light on the dynamical processes operating in the stratosphere and mesosphere. Stratospheric water vapour is an important greenhouse gas through its absorption and emission of infrared radiation and so accurate knowledge of its distribution is required for global climate modelling.

In the upper mesosphere and thermosphere, water vapour photolyses by absorption at the Lyman-α line, which reduces the water vapour content and increases that of the hydrogen free radicals which recombine to produce molecular hydrogen. It is possible that this may influence the mixing ratio of stratospheric H_2O in some regions as a result of rapid downward transport of mesospheric air in high latitude winter allowing air rich in H_2 and poor in H_2O to reach the stratosphere [*Le Texier et al., 1988*].

Water vapour is one of the primary molecules involved in the production of hydrogen-oxygen (HO_x) compounds. These highly reactive HO_x compounds are of particular importance to stratospheric chemistry, especially OH, which plays a significant role in the photochemistry of stratospheric O_3 [*Shimazaki, 1985*]. MLS provides simultaneous measurements of middle atmosphere H_2O and O_3 to higher altitudes (up to ~ 80 km) than previously explored on a global basis and so should contribute valuable information on chemistry of the

stratosphere and mesosphere.

Middle atmosphere water vapour has a long chemical lifetime relative to the time constants for atmospheric transport processes [*Brassuer and Solomon, 1984*] and therefore may be used as a dynamical tracer, its distribution exhibiting variations related to atmospheric transport. Also, knowledge of the water vapour distribution of the lower stratosphere may give important insight into troposphere-stratosphere exchange mechanisms. Thus, the continuous, global observation of stratospheric and mesospheric water vapour by MLS should contribute to a better understanding of atmospheric transport processes.

MLS water vapour measurements are giving valuable information on the distribution and variability of stratospheric water vapour [*Harwood et al, 1993; Carr et al, 1995*] and, coupled with coincident measurements of O_3 and ClO from MLS, are providing important information on the chemistry of the polar stratosphere, both Arctic and Antarctic [*Santee et al., 1995*].

1.4 UARS MLS Instrument Characteristics

In this section a description of the Microwave Limb Sounder is presented emphasising the major characteristics of the instrument. *Barath et al., [1993]* gives a more detailed account of the design and performance of the instrument, and the instrument calibration is described by *Jarnot et al., [1994]*. Figure 1.1 shows a signal-flow block diagram of the MLS instrument. The antenna system consists of three mirrors: primary(paraboloidal), secondary (hyperboloidal) and tertiary(flat). The optics are diffraction-limited and the 1.6 metre vertical dimension of the primary reflector gives a 205 GHz field-of-view (FOV) with full width at half-maximum of 1.3 x 10^{-3} radians (0.07°), which corresponds to $\sim$ 3.5 km vertical extent at the limb. The primary mirror is mechanically scanned in the vertical and receives thermal radiation from the atmospheric limb. This radiation is then directed towards a switching mirror via the secondary and tertiary mirrors. The switching mirror accepts radiation from the antenna system or, for calibration, from an internal target

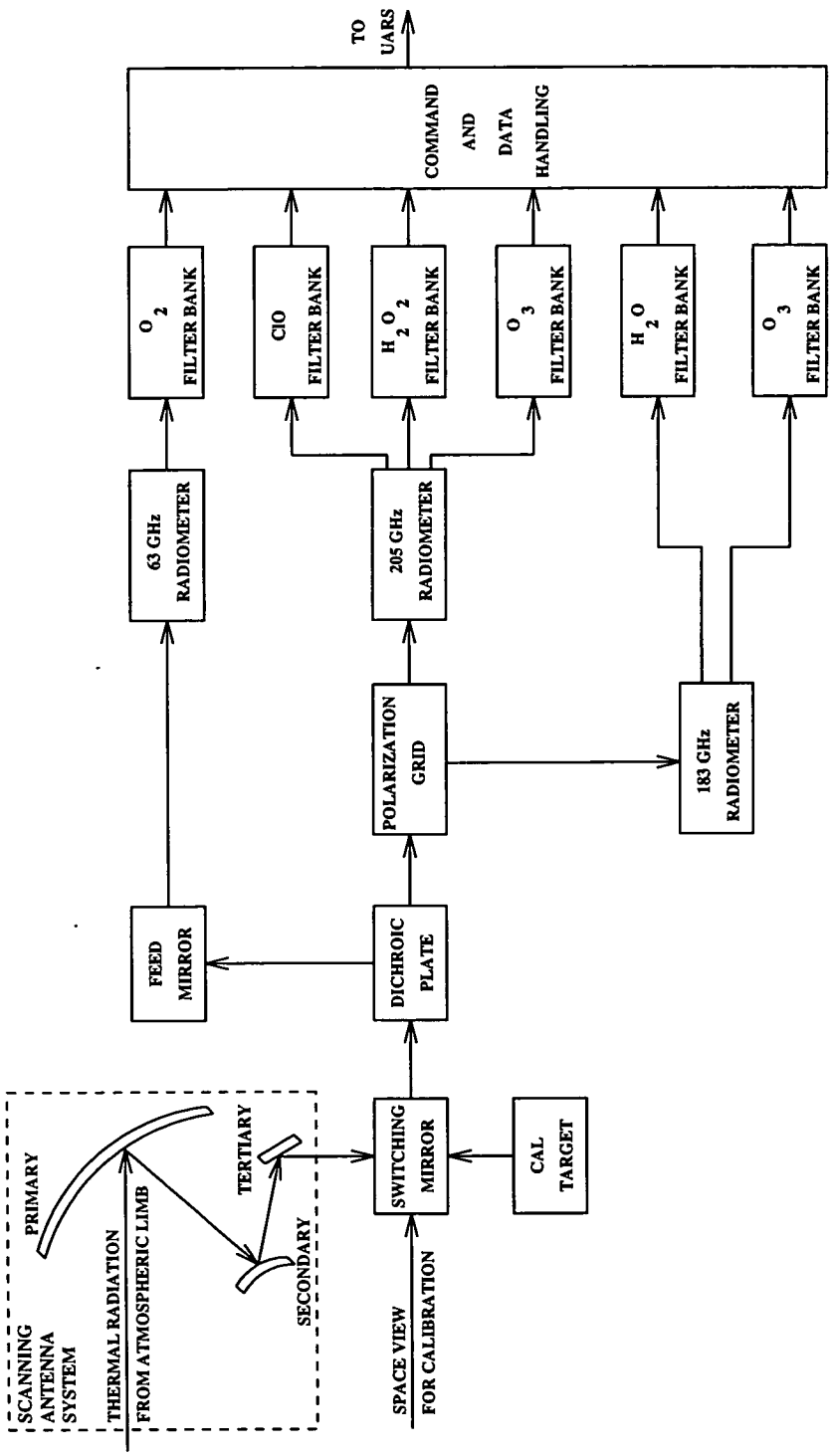

Figure 1.1: Signal-flow block diagram of the MLS instrument

($\sim$290 Kelvin) or a space view ($\sim$3 Kelvin). During each vertical scan space is observed once per $\sim$8 seconds and the internal target is observed once per $\sim$65 seconds. Algorithms have been developed [*Peckham, 1989*] which use the space and target views to optimise radiometric calibration of the instrument. A dichroic plate following the switching mirror separates a signal to the 63 GHz radiometer, a polarisation grid of finely spaced wires then separates signals to the 183 and 205 GHz radiometers.

Ambient-temperature Schottky-diode mixer radiometers down-convert the radiation to intermediate-frequency (IF) bands in the range 0–3 GHz. The radiometers have local oscillators at frequencies of 63.283, 184.777 and 203.267 GHz, and have approximately equal response at IF frequencies above and below the local oscillators. The 183 and 205 GHz local oscillators are generated by frequency tripling from phase-locked Gunn diode oscillators, and the signals are combined quasi-optically with the local oscillator in a folded Fabry-Perot ring resonator [*Pickett and Chiou, 1983*] to produce the IF bands. After amplification, the intermediate frequencies are further frequency-converted to six spectral bands (one for the 63 GHz radiometer, three for the 205 GHz radiometer, and two for the 183 GHz radiometer), each centred at 400 MHz with a width of 510 MHz. Table 1.1 shows the primary retrievals from each of the six spectral bands. These bands are input to six filter banks which split

Radiometer	Band	Retrieval
63 GHz	Band 1	Temperature, tangent pressure
205 GHz	Bands 2,3	ClO
	Band 4	O_3
183 GHz	Band 5	H_2O
	Band 6	O_3

Table 1.1: Primary retrievals for MLS spectral bands

the signal into 15 contiguous spectral channels. Table 1.2 gives the nominal

positions (offset from line centre) and widths of these 15 spectral channels. The power received in each of these channels is integrated, and the resulting

Channel	Frequency offset (MHz)	Channel bandwidth (MHz)	Channel	Frequency offset (MHz)	Channel bandwidth (MHz)
1	-191	128	9	2	2
2	-95	64	10	5	4
3	-47	32	11	11	8
4	-23	16	12	23	16
5	-11	8	13	47	32
6	-5	4	14	95	64
7	-2	2	15	191	128
8	0	2			

Table 1.2: Positions and widths of MLS spectral channels. The position refers to the channel centre and is given as a frequency offset from the band centre.

signal is digitised for transmission to the ground via the Command & Data Handling microprocessor.

All measurements are performed continuously, day and night, with an integration time of 1.8 seconds, and a vertical scan in discrete steps over the altitude range $\sim$ 5–95 km is performed every 65 seconds. Table 1.3 show the tangent pressures and corresponding tangent heights for a typical MLS limb scan.

The MLS antenna points in a direction that is 90° from the UARS orbital velocity and this allows measurements to be made with a latitudinal coverage of 34° on one side of the equator to 80° on the other side of the equator. UARS performs a 180° yaw manoeuvre ten times per year and this allows MLS (and other UARS instruments) to view both northern and southern high latitudes with a periodicity of $\sim$ 36 days.

Tangent pressure (hPa)	Tangent height (km)
0.0024	88.7
0.0084	82.4
0.018	77.9
0.043	72.3
0.10	66.2
0.22	60.3
0.48	54.4
0.78	50.6
1.3	46.7
2.1	42.7
3.1	39.6
4.6	36.5
7.0	33.6
11	30.7
17	27.7
24	25.4
29	24.0
37	22.6
46	21.2
57	19.7
72	18.3
100	16.1
142	13.9
243	10.5
403	7.0
702	2.9

Table 1.3: Typical MLS scan pattern

Chapter 2

Atmospheric Limb Sounding and Retrieval

2.1 Introduction to Limb Sounding

In this section a general introduction to the technique of limb sounding for the purpose of remote sensing of the atmosphere is given. Firstly, the geometry of limb sounding is described. This is followed by a discussion of the radiative transfer involved in limb sounding, with particular emphasis on the microwave region of the electromagnetic spectrum.

The technique of limb sounding from satellite-borne instruments has already been successfully applied to the measurement of vertical profiles of atmospheric temperature and of minor constituent abundances. These instruments include the first limb sounding infrared radiometer (LRIR), the Limb Infrared Monitor of the Stratosphere (LIMS) (for both LRIR and LIMS, see *Gille et al., [1980]*), and the Stratospheric and Mesospheric Sounder (SAMS) [*Drummond et al., 1980*]. All of these instruments measured atmospheric emission in the infrared. Current instruments which employ the limb sounding technique to measure atmospheric emission include the Cryogenic Limb Array Etalon Spectrometer (CLAES) [*Roche et al., 1993*], the Improved Stratospheric and Mesospheric Sounder (ISAMS) [*Taylor et al., 1993*], and the Microwave Limb

Sounder (MLS) (see Chapter 1), all on-board the Upper Atmosphere Research Satellite (UARS) (see Chapter 1). Both CLAES and ISAMS measure atmospheric emission in the infrared, whereas, MLS measures emission at microwave frequencies. MLS is the first satellite-borne microwave radiometer to use the limb sounding technique.

2.1.1 Geometry of Limb Sounding

Instruments which view the Earth's limb measure radiation which leaves the atmosphere nearly tangentially. Figure 2.1 shows a schematic diagram of the geometry of limb sounding. The instrument is located at the observation point

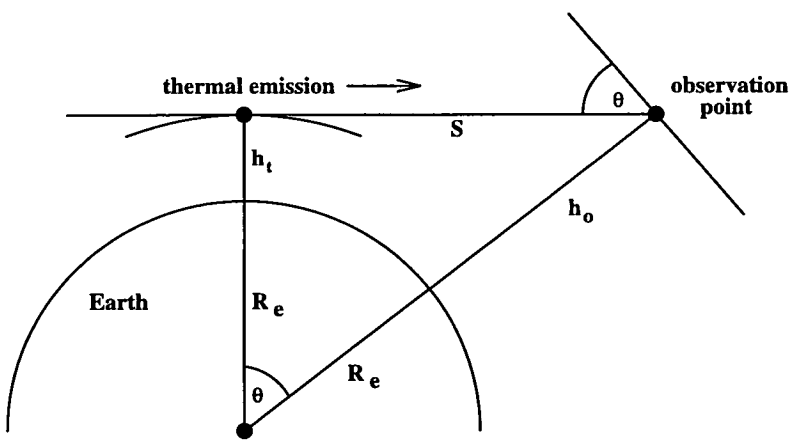

Figure 2.1: Geometry of limb sounding

at a height h_0 above the Earth's surface. Ignoring field-of-view (FOV) effects, the path of a ray of radiation incident upon the instrument, at an angle θ to the local horizontal, is characterised by the height h_t of its tangent point (the point at which the ray path is tangential to the atmosphere). The angle θ is also the great circle angle between the observation and tangent points. R_e represents the radius of the Earth. The distance between the observation point and the tangent point is given by

$$S = \sqrt{(R_e + h_0)^2 - (R_e + h_t)^2} \tag{2.1}$$

An indication of the scale of such a viewing geometry is now given using UARS as an example. For UARS, the altitude, h_0, is approximately 600 km. If a tangent height, h_t, of 20 km is considered and a value of $R_e = 6371$ km is used, then from equation (2.1), the distance S from tangent point to satellite is 2780 km. Waters [*1993*] states that, for an optically thin ray path, half of the total limb radiation arises from an atmospheric layer of 3.2 km vertical extent. Now consider an atmospheric layer of thickness 3.2 km; the tangent point being on the lower boundary of the layer. Using equation (2.1), but replacing h_0 by $(h_t + 3.2\,\text{km})$, now gives the distance, along the ray path, toward the satellite, from the tangent point to the point where the top of the layer crosses the ray path. Using the same values for R_e and h_t as above, this distance is approximately 200 km. Allowing for the spherical symmetry of the atmospheric layer, then the length of the optical path that gives rise to half of the radiation incident at the observation point (for an optically thin ray path) is approximately 400 km. The highest altitudes that can be measured are limited by low signal strengths. Tropospheric attenuation by water (both vapour and liquid), coupled with low signal strengths for other molecules, limits the lower altitudes which can be measured.

Limb sounding instruments tend to have a narrow vertical FOV and obtain vertical resolution by scanning the limb in contrast to nadir sounding instruments which observe radiation leaving the atmosphere in directions near to the local vertical and obtain vertical resolution by scanning spectroscopically. The vertical resolution of a limb sounder is generally better than that obtained by a nadir viewing instrument (*inter alia Houghton et al., 1984*) but the horizontal resolution is on the whole not as good. Limb sounders have the advantage of looking towards a background of 'cold space' whereas, in the nadir viewing geometry, the atmosphere is seen against the complex background of the Earth's surface. Another important aspect of limb sounding compared to nadir viewing is the longer path length through the atmosphere which provides higher sensitivity to molecules of low concentration. This is particularly important for the measurement of trace gases such as ozone.

2.1.2 Radiative Transfer

In this section a brief discussion of radiative transfer at microwave frequencies is given. A more complete treatment is presented by *Waters, [1993]*. For the case of gaseous absorption at microwave frequencies, the effects of scattering are negligible and the atmosphere can be assumed to be in thermal equilibrium. From *Chandrasekhar, [1960]*, the radiative transfer equation takes the form,

$$I_\nu(s) = I_\nu(0)exp[-\tau_\nu(0,s)] + \int_0^s B_\nu(T)exp[-\tau_\nu(s',s)]\kappa_\nu(s')ds' \qquad (2.2)$$

where $I_\nu(s)$ is the intensity of radiation at frequency ν and position s, $B_\nu(T)$ is the Planck function giving the intensity of radiation at frequency ν from a black body at temperature T, $\kappa_\nu(s')$ is the volume absorption coefficient at frequency ν and position s', and

$$\tau_\nu(s',s) = \int_{s'}^{s} \kappa_\nu(s'')ds'' \qquad (2.3)$$

is the optical thickness of the path between points s' and s. The volume absorption coefficient describes the interaction of radiation with the absorbing matter and is a function of the density of the absorbing medium and the temperature and pressure of the atmosphere [*Waters, 1976*], all of which can vary along the path of observation.

A schematic diagram of the geometry of the radiative transfer is shown in figure 2.2, where the absorbing medium extends from $s' = 0$ to $s' = s$, and the integral in equation (2.2) is taken along the observation path.

The first term on the right-hand side of equation (2.2) describes the attenuation of the radiation incident on the medium, $I_\nu(0)$, by the factor $exp[-\tau_\nu(0,s)]$ as it passes from $s' = 0$ to s. The factor $exp[-\tau_\nu(0,s)]$ is called the *transmittance* between 0 and s. In the case of limb sounding, the term $I_\nu(0)$ represents the 'cold' background of space. The second term on the right-hand side of equation (2.2) gives the emission, $B_\nu(T)\kappa_\nu(s')ds'$, from path element ds', attenuated by the factor $exp[-\tau_\nu(s',s)]$, as it passes from s' to s.

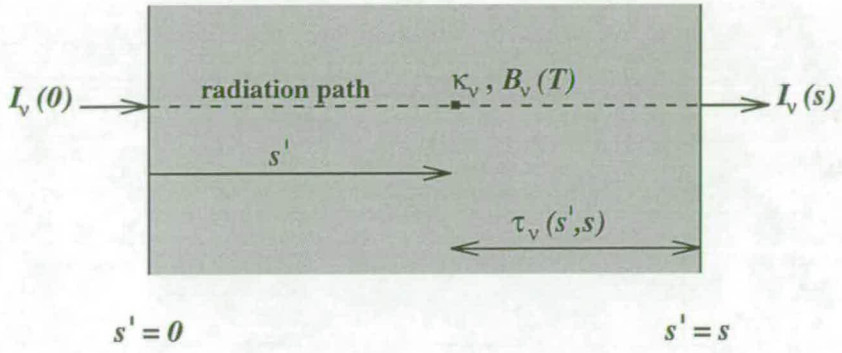

Figure 2.2: Radiative transfer geometry

For the purpose of illustration, it is instructive to assume that the temperature of the absorbing medium is independent of position, s'. Thus, using the definition, $d\tau_\nu(s',s) = -\kappa_\nu(s')ds'$, equation (2.2) can be written as,

$$I_\nu(s) = I_\nu(0)exp[-\tau_\nu(0,s)] + B_\nu(T)\int_{\tau_\nu(s,s)}^{\tau_\nu(0,s)} exp[-\tau_\nu(s',s)]d\tau_\nu(s',s) \quad (2.4)$$

Performing the integral and using the fact that $\tau_\nu(s,s) = 0$ gives,

$$I_\nu(s) = I_\nu(0)exp[-\tau_\nu(0,s)] + B_\nu(T)\{1 - exp[-\tau_\nu(0,s)]\} \quad (2.5)$$

For optically thick cases (defined by $\tau_\nu(0,s) \gg 1$), equation (2.5) becomes,

$$I_\nu(s) = B_\nu(T) \quad (2.6)$$

In this case the intensity of radiation at s only depends on the temperature of the medium and is not affected by the radiation incident at $s' = 0$ due to the large attenuation.

For optically thin cases (defined by $\tau_\nu(0,s) \ll 1$), keeping the first order term in the series expansion of the exponential in equation (2.5) and rearranging gives,

$$I_\nu(s) = I_\nu(0) + \tau_\nu(0,s)\{B_\nu(T) - I_\nu(0)\} \quad (2.7)$$

This shows that as $\tau_\nu(0,s) \to 0$, $I_\nu(s) \to I_\nu(0)$, as it must for a transparent medium.

So far, radiative transfer at a single frequency only has been considered. However, in practice, instruments accept radiation over a finite frequency-range (bandwidth) and a finite solid angle of field-of-view. Thus, the integrated irradiance, I^L, received by an instrument for a particular limb view, is given by an expression of the form,

$$I^L = \int_{\Delta\nu} \int_{\Omega} I_\nu(s) G(\Omega) H(\nu) d\Omega d\nu \tag{2.8}$$

where $I_\nu(s)$ is the monochromatic spectral irradiance given by equation (2.2), $G(\Omega)$ represents the normalised antenna response as a function of solid angle, Ω, and $H(\nu)$ represents the normalised filter response function over the bandwidth, $\Delta\nu$. Equation (2.8), along with equations (2.2) and (2.3), is generally known as the *forward* problem, i.e., how the intensity of radiation observed by the instrument depends on atmospheric properties such as temperature, pressure and, through the absorption coefficient, the density of the absorbing molecules.

Measuring thermal emission at microwave frequencies has certain advantages over measurements in other spectral regions. Firstly, clouds and aerosols have negligible effect on the signal due to the small particle size compared to the wavelength. Also, the spectroscopic database is generally more accurate than in other spectral regions. This is due to the ability to accurately measure line strengths in the laboratory. Stratospheric emission over the submillimeter spectral region has been surveyed to $\sim 100\,\mathrm{MHz}$ resolution [*Baldecchi et al., 1984, 1988*]. For composition measurements, spectral lines can be chosen which have limb thermal emission that is insensitive to temperature [*Waters, 1993*]. This means that highly-accurate simultaneous temperature measurements are not required for deducing molecular abundances.

There are also some disadvantages to making measurements at microwave frequencies. The instrument field-of-view is diffraction limited; a smaller diam-

eter antenna gives a wider field-of-view. Thermal emission in the microwave is less sensitive to temperature than that in the infrared. This is a disadvantage when measuring atmospheric temperature since, for microwaves, the accuracy of the radiance measurement must be higher than that in the infrared in order to gain the same accuracy of temperature measurement [*Houghton, 1984*].

2.2 Retrieval Problem

2.2.1 Introduction

In the previous section the radiative transfer of limb sounding, the so-called forward problem, was discussed. The main goal of remote sensing of the atmosphere is to deduce atmospheric properties, such as temperature and absorber amount, from the radiance observations made by the sensing instrument. This is known as an *inverse* problem as it requires the inverse solution of the forward problem. In relation to the retrieval of atmospheric properties, the inverse problem is usually known as the *retrieval* problem to avoid confusion with the meteorological term 'temperature inversion'.

The problem of deducing a profile of temperature or absorber amount from a set of radiances is formally ill-posed since the unknown profile is a continuous function of height whereas the set of radiance measurements is finite. Thus, the retrieval problem is under-constrained and an infinite number of solution profiles exist for any one set of radiance measurements. A criterion is needed in order to choose *a* solution which is the most appropriate for the particular problem under consideration. Adding to the problem of the uniqueness of a solution is the fact that radiance measurements are made to a finite accuracy. This means that, for any particular criterion used to choose a solution profile, an infinite number of profiles may exist which would be consistent, within the experimental error, with the set of radiance measurements. A successful retrieval method must include sufficient criteria for the choice of a 'best' or 'most appropriate' solution for the particular problem under consideration. Often, some form of *a priori* information is used as a constraint on the solution.

This tends to reduce the sensitivity to noise and to improve the stability of the solution.

The inverse problem, in general, is discussed in more detail by *Menke, [1984].* In relation to remote sensing, *Rodgers, [1976]* and *Twomey, [1977]* give reviews of possible retrieval methods. Further examples of inversion techniques which have been applied to the retrieval of atmospheric properties can be found in *Deepak, [1977]* and *Deepak et al., [1985].*

Before proceeding to discuss the particular method of retrieval applied to the MLS, a formal definition of both the forward and retrieval problem is given. In the following discussion, and throughout the remainder of this chapter, vector quantities will be denoted by lower case letters in bold type, and matrices will be denoted by upper case letters in bold type. The superscript 'T' on both vectors and matrices denotes the transpose, and the superscript '-1' on matrices denotes the matrix inverse. The notation below is consistent with that of *Rodgers, [1990].*

The forward problem, mentioned in the previous section, can be represented in a discrete schematic form as,

$$\mathbf{y} = F(\mathbf{x}, \mathbf{b}) + \epsilon_y \tag{2.9}$$

where F is the atmospheric *forward model* which represents the detailed physics of the measurement. The *state vector*, which contains the true values of the parameters to be retrieved, is represented by $\mathbf{x}$. Usually, this is a profile of some quantity, given at a finite number n of levels, where n is large enough to adequately represent the possible atmospheric variations. In principle, $\mathbf{x}$ may contain the true value of any relevant variable which is to be retrieved. The vector $\mathbf{b}$ represents quantities which affect the radiances but are not being retrieved, such as spectral line data and instrument calibration parameters. The vector $\mathbf{y}$ contains the set of radiance measurements and ϵ_y represents the noise on each radiance measurement.

The inverse problem involves finding an estimate, $\hat{\mathbf{x}}$ say, of the unknown

quantities, $\mathbf{x}$, given the measurements $\mathbf{y}$ with error ϵ_y, and can be formally represented as,

$$\hat{\mathbf{x}} = I(\mathbf{y}, \mathbf{b}, \mathbf{c}) \tag{2.10}$$

where $\mathbf{c}$ is a vector of parameters which are used in the retrieval scheme but are not used in the forward model, such as *a priori* data. The *inverse model*, I, describes how the estimate, $\hat{\mathbf{x}}$, is obtained given $\mathbf{y}$, $\mathbf{b}$ and $\mathbf{c}$.

2.2.2 Optimal Estimation

The inversion technique used in the MLS retrieval scheme is that of *optimal estimation.* A brief account of this technique follows. A more detailed discussion of optimal estimation is given by *Rodgers, [1976].*

Optimal estimation involves the combination of measurements and *a priori* information. The *a priori* information is usually in the form of a climatological mean profile, $\mathbf{x}_a$, with associated covariance, $\mathbf{S}_a$, which describes the expected variability of $\mathbf{x}$. These quantities can be derived from data sets of previous measurements of the quantity $\mathbf{x}$. In the absence of any previous measurements, estimates of $\mathbf{x}_a$ and $\mathbf{S}_a$ may have to be made from some other source, such as model calculations. The quantities $\mathbf{x}_a$ and $\mathbf{S}_a$ should represent the best *a priori* knowledge of the parameters to be retrieved.

The measurements are assumed to be of the form,

$$\mathbf{y} = \mathbf{K}\mathbf{x} + \epsilon_y \tag{2.11}$$

where ϵ_y has a mean of zero and covariance $\mathbf{S}_\epsilon$. Thus, $\mathbf{y}$ is assumed to be linearly related to $\mathbf{x}$ through the matrix kernel, $\mathbf{K}$. Now, $\mathbf{K}$ is formally defined as,

$$\mathbf{K} = \frac{\partial F}{\partial \mathbf{x}} \tag{2.12}$$

The matrix, $\mathbf{K}$ is known as the *influence function matrix* (or weighting function matrix) and describes the sensitivity of each radiance measurement to perturbations in each level of the parameter, $\mathbf{x}$. The influence function matrix

is central to the retrieval of the unknown quantity, and to the error analysis (see Section 2.3) of the retrievals. For MLS, examples of the influence function, showing sensitivity of the MLS band 5 radiances to perturbations in H_2O, are presented and discussed in Chapter 3.

In optimal estimation, the most probable solution is sought given the measurements and the *a priori* information. The error statistics of both the measurements $\mathbf{y}$ and the *a priori* information $\mathbf{x}_a$ are assumed to be Gaussian in nature. For any random vector, $\mathbf{u}$, of dimension n, say, the multivariate Gaussian distribution may be written as [*Mood et al., 1974*],

$$P(\mathbf{u}) = [(2\pi)^n \det(\mathbf{S}_u)]^{-\frac{1}{2}} exp[-\frac{1}{2}(\mathbf{u} - \bar{\mathbf{u}})^T \mathbf{S}_u^{-1}(\mathbf{u} - \bar{\mathbf{u}})] \qquad (2.13)$$

where $P(\mathbf{u})$ is the probability density function of the random vector $\mathbf{u}$, $\bar{\mathbf{u}}$ is the expected value of $\mathbf{u}$, and $det(\mathbf{S}_u)$ is the determinant of the covariance matrix, $\mathbf{S}_u$.

The probability of any solution, $\mathbf{x}$, given the set of measurements $\mathbf{y}$ and the *a priori* information $\mathbf{x}_a$, is given by the conditional probability density function $P(\mathbf{x}|\mathbf{y}, \mathbf{x}_a)$. The most likely value of $\mathbf{x}$ is the one which maximises this conditional probability density function. Making use of Bayes theorem [*Mood et al., 1974*], maximising $P(\mathbf{x}|\mathbf{y}, \mathbf{x}_a)$ with respect to $\mathbf{x}$ gives the maximum likelihood solution, $\hat{\mathbf{x}}$, as [*Rodgers, 1976*],

$$\hat{\mathbf{x}} = (\mathbf{S}_a^{-1} + \mathbf{K}^T \mathbf{S}_\epsilon^{-1} \mathbf{K})^{-1} (\mathbf{S}_a^{-1} \mathbf{x}_a + \mathbf{K}^T \mathbf{S}_\epsilon^{-1} \mathbf{y}) \qquad (2.14)$$

with covariance

$$\hat{\mathbf{S}} = (\mathbf{S}_a^{-1} + \mathbf{K}^T \mathbf{S}_\epsilon^{-1} \mathbf{K})^{-1} \qquad (2.15)$$

Thus, the solution, $\hat{\mathbf{x}}$, is seen to be a weighted combination of the measurements, $\mathbf{y}$ and the *a priori* information, $\mathbf{x}_a$. This solution is optimal in the sense that it is the most probable solution. The constraining effect of the *a priori* information can be seen from equations (2.14) and (2.15). If the error on each measurement is increased, such that $\epsilon_y \rightarrow \infty$ for every measurement,

then $\hat{\mathbf{x}} \rightarrow \mathbf{x}_a$ and $\hat{\mathbf{S}} \rightarrow \mathbf{S}_a$.

Equations (2.14) and (2.15) involve the inversion of three relatively large matrices. These equations can be transformed (see Appendix A) into a more computationally efficient form, involving the inversion of only one matrix, to give

$$\hat{\mathbf{x}} = \mathbf{x}_a + \mathbf{S}_a\mathbf{K}^T(\mathbf{K}\mathbf{S}_a\mathbf{K}^T + \mathbf{S}_\epsilon)^{-1}(\mathbf{y} - \mathbf{K}\mathbf{x}_a) \tag{2.16}$$

for the optimal estimate of $\mathbf{x}$ with error covariance

$$\hat{\mathbf{S}} = \mathbf{S}_a - \mathbf{S}_a\mathbf{K}^T(\mathbf{K}\mathbf{S}_a\mathbf{K}^T + \mathbf{S}_\epsilon)^{-1}\mathbf{K}\mathbf{S}_a \tag{2.17}$$

2.2.3 MLS Retrieval Scheme

Sequential Estimation

In the MLS retrieval scheme, equations (2.16) and (2.17) are solved to give $\hat{\mathbf{x}}$ and $\hat{\mathbf{S}}$, respectively. The retrieval algorithm uses the method of sequential estimation [*Rodgers, 1976*] to solve the equations. Using this method, it is not necessary to perform any matrix inversions. The assumption must be made that the measurement error covariance matrix, $\mathbf{S}_\epsilon$, is purely diagonal, i.e., that the noise on each radiance measurement is not correlated between measurements. In sequential estimation, the measurement vector, $\mathbf{y}$, is treated as a set of scalars y_i, for i = 1,...m. The initial estimates of the solution and its error covariance are set to $\hat{\mathbf{x}}_0 = \mathbf{x}_a$ and $\hat{\mathbf{S}}_0 = \mathbf{S}_a$. These estimates are then updated sequentially in the following way:

for $i = 1, ..., m$

$$\begin{aligned}\hat{\mathbf{x}}_i &= \hat{\mathbf{x}}_{i-1} + \hat{\mathbf{S}}_{i-1}\mathbf{k}_i(y_i - \mathbf{k}_i^T\hat{\mathbf{x}}_{i-1})/(\mathbf{k}_i^T\hat{\mathbf{S}}_{i-1}\mathbf{k}_i + \epsilon_i^2) \\ \hat{\mathbf{S}}_i &= \hat{\mathbf{S}}_{i-1} - \hat{\mathbf{S}}_{i-1}\mathbf{k}_i\mathbf{k}_i^T\hat{\mathbf{S}}_{i-1}/(\mathbf{k}_i^T\hat{\mathbf{S}}_{i-1}\mathbf{k}_i + \epsilon_i^2)\end{aligned} \tag{2.18}$$

The final estimates of $\mathbf{x}$ and $\mathbf{S}$ are given by $\hat{\mathbf{x}} = \hat{\mathbf{x}}_m$ and $\hat{\mathbf{S}} = \hat{\mathbf{S}}_m$, respectively. The column vector $\mathbf{k}_i$ contains the ith row of the influence function matrix $\mathbf{K}$.

The term ϵ_i^2 is the ith diagonal element of the measurement error covariance matrix, $\mathbf{S}_\epsilon$. In fact, the sequential estimation algorithm may be applied even if the matrix $\mathbf{S}_\epsilon$ is non-diagonal; this requires the diagonalisation of $\mathbf{S}_\epsilon$. In the above algorithm, at each stage, each element of $\mathbf{y}$ is treated separately and a new estimate $\hat{\mathbf{x}}$ is produced with an associated error covariance $\hat{\mathbf{S}}$. These estimates are used as the *a priori* values for the next stage. Using sequential estimation, the matrix inverse in equations (2.16) and (2.17) has become a scalar reciprocal, and the final values of $\hat{\mathbf{x}}$ and $\hat{\mathbf{S}}$ are identical to those obtained from the original equations [*Rodgers, 1976*].

Opacity Criterion

An important feature of the MLS retrieval scheme is the use of an *opacity criterion* which eliminates from the retrieval radiances which arise from optically thick paths. This is necessary as the retrieval method described above assumes a linear relationship between the radiances $\mathbf{y}$ and the unknown parameters $\mathbf{x}$. Considering the retrieval of atmospheric constituent amounts, if the viewing path is optically thick then the linear relationship no longer holds and the retrieval method is not valid.

An approximate method of estimating the optical thickness of the viewing path is used. The estimated optical thickness of a limb path for a particular MLS channel is given by [*Froidevaux et al., 1994*],

$$\tau_{p_i} = -ln[1 - y_i/(\omega_{p_i} T_{tan})] \tag{2.19}$$

where y_i is the measured radiance (in brightness temperature units) in the ith channel, ω_{p_i} is the proportion of the measured brightness temperature which comes from the principal sideband of the ith channel, T_{tan} is the temperature at the tangent point and τ_{p_i} is the estimated optical thickness in the ith channel. In the derivation of this estimate any contribution from the image sideband of the channel is ignored. Also, the atmosphere is assumed to be isothermal and at the temperature of the tangent point, T_{tan}. The estimated optical thickness, τ_{p_i}, is compared with a prescribed critical value and, if $\tau_{p_i} > \tau_c$, then

the corresponding radiance measurement y_i is ignored during the sequential estimation algorithm. For the MLS Version 3 retrieval, $\tau_c = 1$.

Further details relevant to the retrieval of H_2O from the radiance measurements in band 5 of MLS are given in Chapter 3.

2.3 Characterisation and Error Analysis

2.3.1 Characterisation of the Retrieval

The following discussion follows the formalism of *Rodgers, [1990]* for the characterisation and error analysis of profiles retrieved from remote sounding measurements. The inverse model was formally defined above in equation (2.10). This definition can also be written as

$$\hat{\mathbf{x}} = I(\mathbf{y}, \mathbf{b}, \mathbf{c}) = T(\mathbf{x}, \mathbf{b}, \mathbf{c}) \tag{2.20}$$

which formally defines the *transfer function*, T, which relates the retrieved quantities, $\hat{\mathbf{x}}$, to the true values, $\mathbf{x}$, and the sets of parameters $\mathbf{b}$ and $\mathbf{c}$. For clarity of explanation, and since this thesis is based on the retrieval of water vapour profiles, the state vector, $\mathbf{x}$, is assumed to contain a profile of atmospheric constituent amounts at a finite number, n, of levels.

Contribution function

The sensitivity of the retrieved profile, $\hat{\mathbf{x}}$, to the measurements, $\mathbf{y}$, can be expressed as the so-called *contribution function*, $\mathbf{D}$, where

$$\mathbf{D} = \frac{\partial \hat{\mathbf{x}}}{\partial \mathbf{y}} \tag{2.21}$$

From equation (2.16), $\mathbf{D}$ is given by

$$\mathbf{D} = \mathbf{S}_a \mathbf{K}^T (\mathbf{K} \mathbf{S}_a \mathbf{K}^T + \mathbf{S}_\epsilon)^{-1} \tag{2.22}$$

Each column of the contribution function matrix, $\mathbf{D}$, describes the sensitiv-

ity of each level of the retrieved profile to a perturbation in a single radiance measurement. Thus, the contribution function reflects the sensitivity of the retrieval to noise in the measurements. If the influence functions for particular measurements overlap sufficiently then oscillations are induced in the contribution function as the retrieval attempts to follow noise in the observations [*Rodgers, 1976*]. Examples of columns of **D** for the retrieval of H_2O from the MLS band 5 radiances are given in Chapter 3.

Averaging kernel

The sensitivity of the retrieval to the true profile is given by the so-called *averaging kernel* matrix, **A**, as

$$\mathbf{A} = \frac{\partial \hat{\mathbf{x}}}{\partial \mathbf{x}} \tag{2.23}$$

From equation (2.16), and using the fact that $\frac{\partial \mathbf{y}}{\partial \mathbf{x}} = \mathbf{K}$, the averaging kernel matrix, **A**, can be expressed as

$$\mathbf{A} = \mathbf{S}_a\mathbf{K}^T(\mathbf{K}\mathbf{S}_a\mathbf{K}^T + \mathbf{S}_\epsilon)^{-1}\mathbf{K} = \mathbf{D}\mathbf{K} \tag{2.24}$$

Each row of the matrix **A** contains the scaling factors that determine how perturbations in each level of the real atmosphere are reproduced in a particular level of the retrieved profile. For an ideal observing system, **A** would be the identity matrix **I**, but normally the rows of **A** will represent peaked functions, with the width of the peak being a measure of the vertical resolution of the retrieval. The rows of the averaging kernel matrix, **A**, for the retrieval of H_2O from the MLS band 5 radiances are plotted and discussed in Chapter 3.

2.3.2 Error Analysis

A method of quantifying the contribution to the retrieved profile of sources of error in remote measurements of the atmosphere is important both in the design of a remote sensing instrument and in the analysis of the retrievals. A formal method of evaluating such errors is outlined below.

The inverse model in equation (2.10) can be rewritten by using the expression for the measurements, $\mathbf{y}$, in equation (2.9) and bearing in mind that the measuring system uses exact values of the model parameters $\mathbf{b}$, whereas the inverse model uses estimates $\hat{\mathbf{b}}$. Thus, the inverse model can be expressed as,

$$\hat{\mathbf{x}} = I(F(\mathbf{x}, \mathbf{b}) + \epsilon_{\mathbf{y}}, \hat{\mathbf{b}}, \mathbf{c}) \tag{2.25}$$

For the purpose of error analysis, the inverse model is linearised about a state $(\bar{\mathbf{x}}, \hat{\mathbf{b}}, \mathbf{c})$, where $\bar{\mathbf{x}}$ is an arbitrary profile. Retaining the first order terms only and using the definitions of $\mathbf{K}$ and $\mathbf{D}$ from equations (2.12) and (2.21), respectively, gives [*Rodgers, 1990*],

$$\hat{\mathbf{x}} = T(\bar{\mathbf{x}}, \hat{\mathbf{b}}, \mathbf{c}) + \mathbf{DK}(\mathbf{x} - \bar{\mathbf{x}}) + \mathbf{DK}_b(\mathbf{b} - \hat{\mathbf{b}}) + \mathbf{D}\epsilon_y \tag{2.26}$$

where $\mathbf{K}_b$ is the sensitivity of the measurements to perturbations in the model parameters, $\mathbf{b}$, and is defined by

$$\mathbf{K}_b = \frac{\partial F}{\partial \mathbf{b}} \tag{2.27}$$

Equation (2.26) can be rearranged to give the total error in a retrieval as

$$\hat{\mathbf{x}} - \mathbf{x} = [T(\bar{\mathbf{x}}, \hat{\mathbf{b}}, \mathbf{c}) - \bar{\mathbf{x}}] + (\mathbf{A} - \mathbf{I})(\mathbf{x} - \bar{\mathbf{x}}) + \mathbf{DK}_b\mathbf{\Delta b} + \mathbf{D}\epsilon_y \tag{2.28}$$

where $\mathbf{A}$ is defined by equation (2.23), and $\mathbf{I}$ is the identity matrix. $\mathbf{\Delta b}$ replaces $(\mathbf{b} - \hat{\mathbf{b}})$ and represents the uncertainty in the knowledge of the model parameters, $\mathbf{b}$.

Replacing $\bar{\mathbf{x}}$, the arbitrary profile, with $\mathbf{x}_a$, the *a priori* profile, in equation (2.28) and noting that $[T(\mathbf{x}_a, \hat{\mathbf{b}}, \mathbf{c}) - \mathbf{x}_a] = 0$, gives

$$\hat{\mathbf{x}} - \mathbf{x} = (\mathbf{A} - \mathbf{I})(\mathbf{x} - \mathbf{x}_a) + \mathbf{DK}_b\mathbf{\Delta b} + \mathbf{D}\epsilon_y \tag{2.29}$$

Thus, the total retrieval error is composed of three main terms.

Smoothing error

The first term on the right-hand side of equation (2.29) is the so-called *smoothing error* and represents the error due to the smoothing effect of both the measurement technique and the retrieval process, through the averaging kernel matrix. The smoothing error is a measure of the contribution of the *a priori* uncertainty to the retrieval error. For an ideal observing system, $\mathbf{A} = \mathbf{I}$, and there is no smoothing error. The covariance of the smoothing error is given by,

$$\mathbf{S}_S = (\mathbf{A} - \mathbf{I})\mathbf{S}_a(\mathbf{A} - \mathbf{I})^T \tag{2.30}$$

Model parameter errors

The second term on the right-hand side of equation (2.29) is the error in the retrieved profile due to uncertainties in the forward model parameters. This error can be either random or systematic in nature depending on the source of the uncertainty. The uncertainty in the forward model parameters is denoted by $\mathbf{\Delta b}$ and the covariance of this uncertainty will be denoted by $\mathbf{S}_b$. Thus, the covariance of the contribution to the error in the retrieved profile due to the uncertainty in forward model parameters is given by,

$$\mathbf{S}_P = \mathbf{D}\mathbf{K}_b\mathbf{S}_b\mathbf{K}_b^T\mathbf{D}^T \tag{2.31}$$

Measurement error

The third term on the right-hand side of equation (2.29) represents the contribution of the measurement noise to the error in the retrieved profile. This error contribution is random in nature and its covariance is given by,

$$\mathbf{S}_M = \mathbf{D}\mathbf{S}_\epsilon\mathbf{D}^T \tag{2.32}$$

From equation (2.29) the total error in the retrieval is seen to be the sum of the smoothing error, the contribution from the measurement noise, and the contribution from the uncertainty in the forward model parameters. Assuming that these three error contributions are independent, then the covariance of

the error in the retrieved profile is given by,

$$\hat{\mathbf{S}} = \mathbf{S}_S + \mathbf{S}_P + \mathbf{S}_M \tag{2.33}$$

The diagonal elements of each of the error covariance matrices on the right-hand side of equation (2.33) represent the respective contributions to the variance of the retrieved profile. However, the off-diagonal elements of the error covariance matrices also give information on the nature of the errors.

Correlated errors

One way of conceptualising an error covariance matrix, $\mathbf{S}$ of dimension $n \times n$ say, is to diagonalise it, i.e., by finding its eigenvalues and eigenvectors such that,

$$\mathbf{SL} = \mathbf{L}\Lambda \tag{2.34}$$

where the columns of the matrix $\mathbf{L}$ are the eigenvectors of $\mathbf{S}$ and the eigenvalues form the diagonal elements of the diagonal matrix, Λ. The error covariance matrix, $\mathbf{S}$, is symmetric and therefore the eigenvectors may be normalised to give

$$\mathbf{L}^T\mathbf{L} = \mathbf{L}\mathbf{L}^T = \mathbf{I} \tag{2.35}$$

Thus, the error covariance matrix can be expressed as

$$\mathbf{S} = \mathbf{L}\Lambda\mathbf{L}^T \tag{2.36}$$

or, since Λ is a diagonal matrix, $\mathbf{S}$ can be decomposed to give

$$\mathbf{S} = \sum_{i=1}^{n} \lambda_i \mathbf{l}_i \mathbf{l}_i^T = \sum_{i=1}^{n} \mathbf{e}_i \mathbf{e}_i^T \tag{2.37}$$

where λ_i are the eigenvalues and $\mathbf{l}_i$ are the corresponding eigenvectors. The orthogonal quantities $\mathbf{e}_i = \lambda^{\frac{1}{2}}\mathbf{l}_i$ are the so-called *error patterns*; individual components of the error which are uncorrelated with each other.

Eigenvectors of the averaging kernel matrix, A

Equation (2.29) can be rewritten by expanding the term $(\mathbf{A} - \mathbf{I})(\mathbf{x} - \mathbf{x}_a)$ and grouping together the terms in $\mathbf{x}$ and the terms in $\mathbf{x}_a$ to give,

$$\hat{\mathbf{x}} = \mathbf{A}\mathbf{x} + (\mathbf{I} - \mathbf{A})\mathbf{x}_a + \mathbf{D}\mathbf{K}_b\Delta\mathbf{b} + \mathbf{D}\epsilon_y \tag{2.38}$$

The retrieved profile is now expressed as a linear combination of the true profile, $\mathbf{x}$, and the *a priori* profile, $\mathbf{x}_a$, with respective matrix weights, $\mathbf{A}$ and $\mathbf{I} - \mathbf{A}$, plus the contributions from uncertainties in the model parameters, $\mathbf{b}$ and noise in the measurements, ϵ_y. In order to understand the effect on the solution of the matrix weights, an eigenvector decomposition is useful.

Let $\mathbf{U}$ be the matrix of eigenvectors of $\mathbf{A}$ such that $\mathbf{AU} = \mathbf{U}\Lambda$, where Λ is the diagonal matrix of eigenvalues of $\mathbf{A}$. Using the fact that $\mathbf{U}^{-1}\mathbf{A} = \Lambda\mathbf{U}^{-1}$, then multiplying both sides of equation (2.38) on the left by $\mathbf{U}^{-1}$, and ignoring the error terms gives,

$$\mathbf{U}^{-1}\hat{\mathbf{x}} = \Lambda\mathbf{U}^{-1}\mathbf{x} + (\mathbf{I} - \Lambda)\mathbf{U}^{-1}\mathbf{x}_a \tag{2.39}$$

The eigenvectors of $\mathbf{A}$ (the columns of $\mathbf{U}$) can be considered as a representation of $\mathbf{x}$ such that $\mathbf{x} = \mathbf{U}\mathbf{w}$, where the vector, $\mathbf{w}$, contains the representation coefficients. Now, using the fact that $\mathbf{w} = \mathbf{U}^{-1}\mathbf{x}$, then equation (2.39) becomes,

$$\hat{\mathbf{w}} = \Lambda\mathbf{w} + (\mathbf{I} - \Lambda)\mathbf{w}_a \tag{2.40}$$

Since Λ is diagonal, equation (2.40) can be separated into components, giving

$$\hat{w}_i = \lambda_i w_i + (1 - \lambda_i)w_{a_i} \tag{2.41}$$

The elements of $\hat{\mathbf{w}}$ are expressed as scalar weighted means of the corresponding elements of $\mathbf{w}$ and $\mathbf{w}_a$. Thus, the solution profile, $\hat{\mathbf{x}}$, can be decomposed into patterns; those structures corresponding to $\lambda_i \sim 1$ will be well represented by the measurements, those structures corresponding to $\lambda_i \sim 0$ will come mainly from the *a priori* information, and those structures corresponding to

λ_i values somewhere between 0 and 1 will contain components from both the measurements and the *a priori* information.

All of the above techniques are applied to the retrieval of H_2O from the MLS band 5 radiances and the resulting characterisation and error analysis is presented in Chapter 3.

Chapter 3

Characterisation and Error Analysis of UARS MLS 183 GHz H_2O Retrievals

3.1 Introduction

A characterisation and error analysis of the H_2O retrievals from the 183 GHz radiometer of MLS are presented in this chapter. Firstly, some model spectra in the region of the 183 GHz H_2O line are shown along with some typical radiances measured by band 5 of the 183 GHz radiometer. Also, the influence function, **K**, which describes the sensitivity of the band 5 radiances to perturbations in the H_2O mixing ratio is discussed. Then, some important details of the H_2O retrieval method are given and the contribution function, **D**, which describes the sensitivity of the H_2O retrieval to changes in the band 5 radiances is discussed. Following this, typical averaging kernels for H_2O are shown and an indication of the contribution of the *a priori* information to the retrieved amounts is given. An estimate of the vertical resolution of the retrievals is also given. An error analysis for the H_2O retrievals is then presented which consists of a discussion of estimates of both the random and systematic errors involved in the retrieval of H_2O. Unless stated otherwise, all calculations and

analyses are performed for typical mid-latitude conditions and are relevant to Version 3 of the MLS H_2O retrievals.

Model spectra

The microwave spectrum of H_2O is due to electric dipole transitions between rotational states of the molecule. The H_2O molecule is an asymmetric rotor which means that no two of its three principal moments of inertia are equal [*Townes and Schawlow, Chapter 4, 1975*]. The ten lowest frequency rotational spectral lines of $H_2^{16}O$, the dominant isotopic form of water vapour, occur between 22.23 GHz and 448 GHz [*Waters, 1976*]. Band 5 of the MLS 183 GHz radiometer has its primary sideband centred on the 183.3 GHz H_2O line. Figure 3.1 shows calculated limb emission in the spectral region 182–

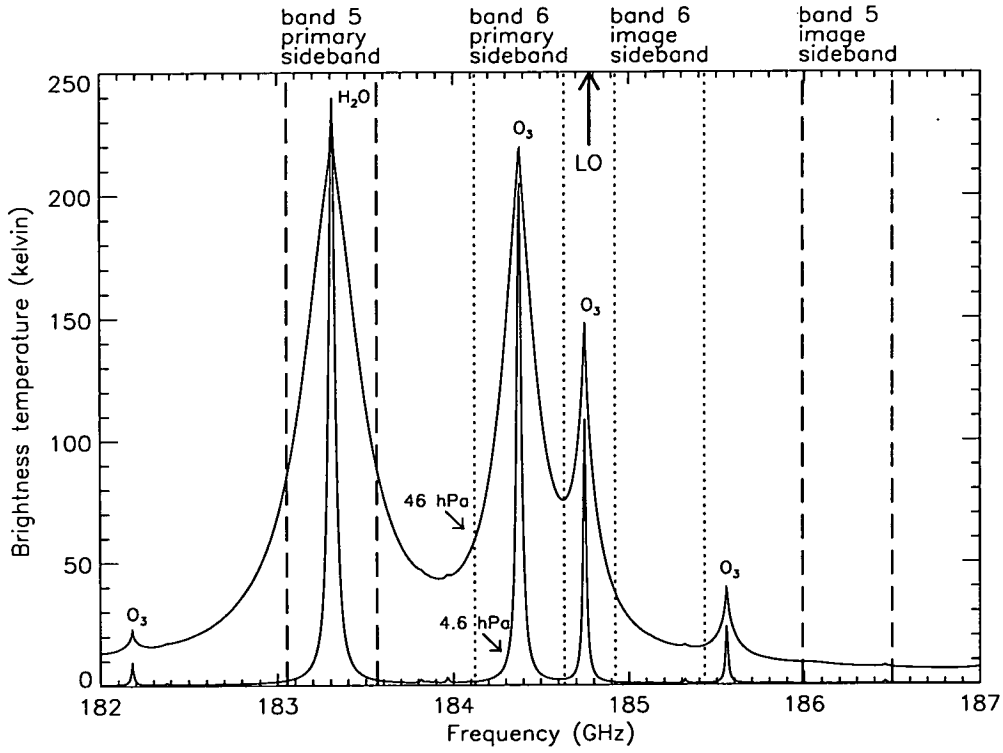

Figure 3.1: Calculated limb emission in the spectral region 182–187 GHz

187 GHz which includes both spectral sidebands of band 5 and band 6 (MLS band 6 radiances are used for retrieving O_3, see *Froidevaux et al., 1994*). The position of the local oscillator (LO) at 184.78 GHz is indicated on the

plot. Spectra are shown for tangent pressures in both the upper and lower stratosphere; namely at 4.6 hPa and 46 hPa, respectively. Spectral lines of all molecules which are thought to be important are included in the calculation employing spectral data from the JPL catalogue [*Pickett et al., 1992*]. The primary (signal) sideband is dominated by the 183.3 GHz H_2O line whereas the image sideband contains no strong lines, giving a 'clean' measurement of 183 GHz H_2O limb emission.

Measured radiances

Typical examples of measured radiances in band 5 are shown in figures 3.2 and 3.3. Vertical profiles of the radiances in channels 1 to 8 are plotted

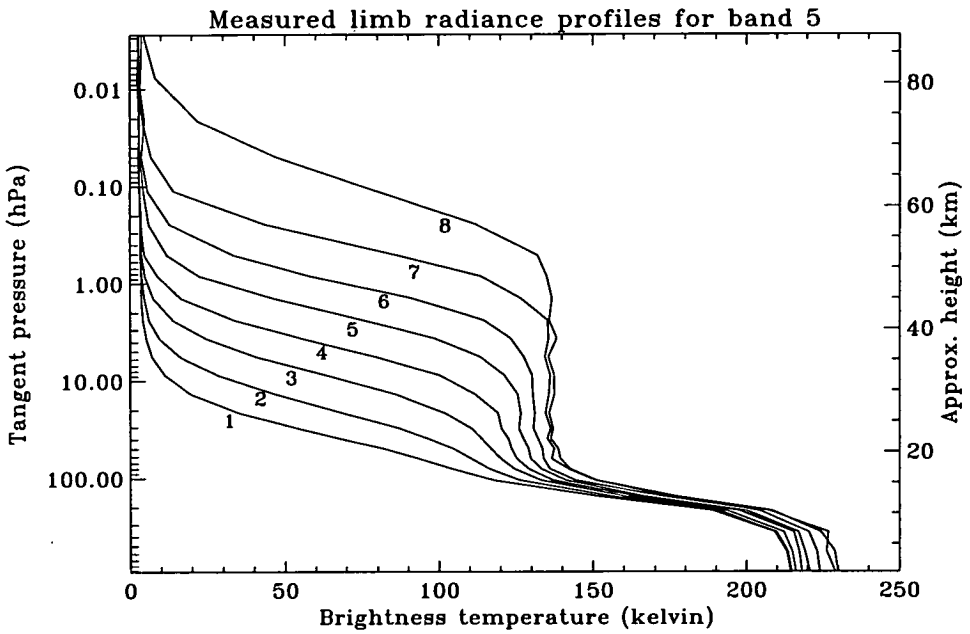

Figure 3.2: Measured limb radiance profiles for channels 1–8 of band 5

in figure 3.2. Channel 8 measures the limb emission at the line centre and saturates in the primary sideband at tangent heights of $\sim$ 50 km. Between $\sim$ 50 km and $\sim$ 20 km, where the primary sideband of channel 8 is saturated and there is no significant signal in the image sideband, variations in that radiance reflect variations in the temperature of the atmosphere. For channel 1, on the wing of the 183.3 GHz line, the signal in the primary sideband is not

significant until the FOV is scanned down to tangent heights of $\sim$ 30 km. The signal in the image sideband begins to make a significant contribution in all channels at $\sim$ 20 km. Vertical profiles of the radiances in channels 9 to 15 are similar to those in channels 7 to 1, respectively. The three panels in figure 3.3 display typical measured spectra in the mesosphere, upper stratosphere and lower stratosphere. The width of each channel is depicted by a horizontal bar and the measurement uncertainty is represented by a vertical bar. The effect of pressure broadening is clearly seen as the tangent pressure increases.

Influence functions

Influence functions (as defined in Chapter 2) for band 5 have been evaluated using the MLS forward model of Read, [*paper in preparation*]. In figure 3.4 selected influence functions with respect to H_2O are shown for channels 1, 4 and 8 of band 5. These influence functions describe the sensitivity of the band 5 model radiances to perturbations in the H_2O mixing ratio profile. Here the H_2O profile is represented as piecewise-linear in mixing ratio versus logarithm of atmospheric pressure, with breakpoints at pressure surfaces of $z = -3.0 + \frac{n}{3}$ where n = 0,...,19 and z is in units of $-\log_{10}$(hPa). The influence functions have been evaluated at 43 tangent pressures; $z = -3.0 + \frac{n}{6}$ where n = 0,...,42. The calculations include the effects of both the primary and image sidebands of each channel. For each plot, the vertical axis represents the pressure level of the perturbation in the H_2O mixing ratio profile and the horizontal axis represents the sensitivity, in units of Kelvin/ppmv, of the measured radiance to the perturbation in H_2O. The numbers printed to the right of the influence function peaks are the tangent pressures, in units of $-\log_{10}$(hPa), associated with each influence function. In the top panel, it can be seen that channel 1 radiances are most sensitive to H_2O perturbations in the lower stratosphere. This is because channel 1 lies on the wing of the 183.3 GHz H_2O line, and so H_2O emission contributes to the received signal in this channel at tangent pressures in the lower stratosphere, where the effects of pressure broadening are significant. Thus, the radiances in channel 1 supply information on the H_2O

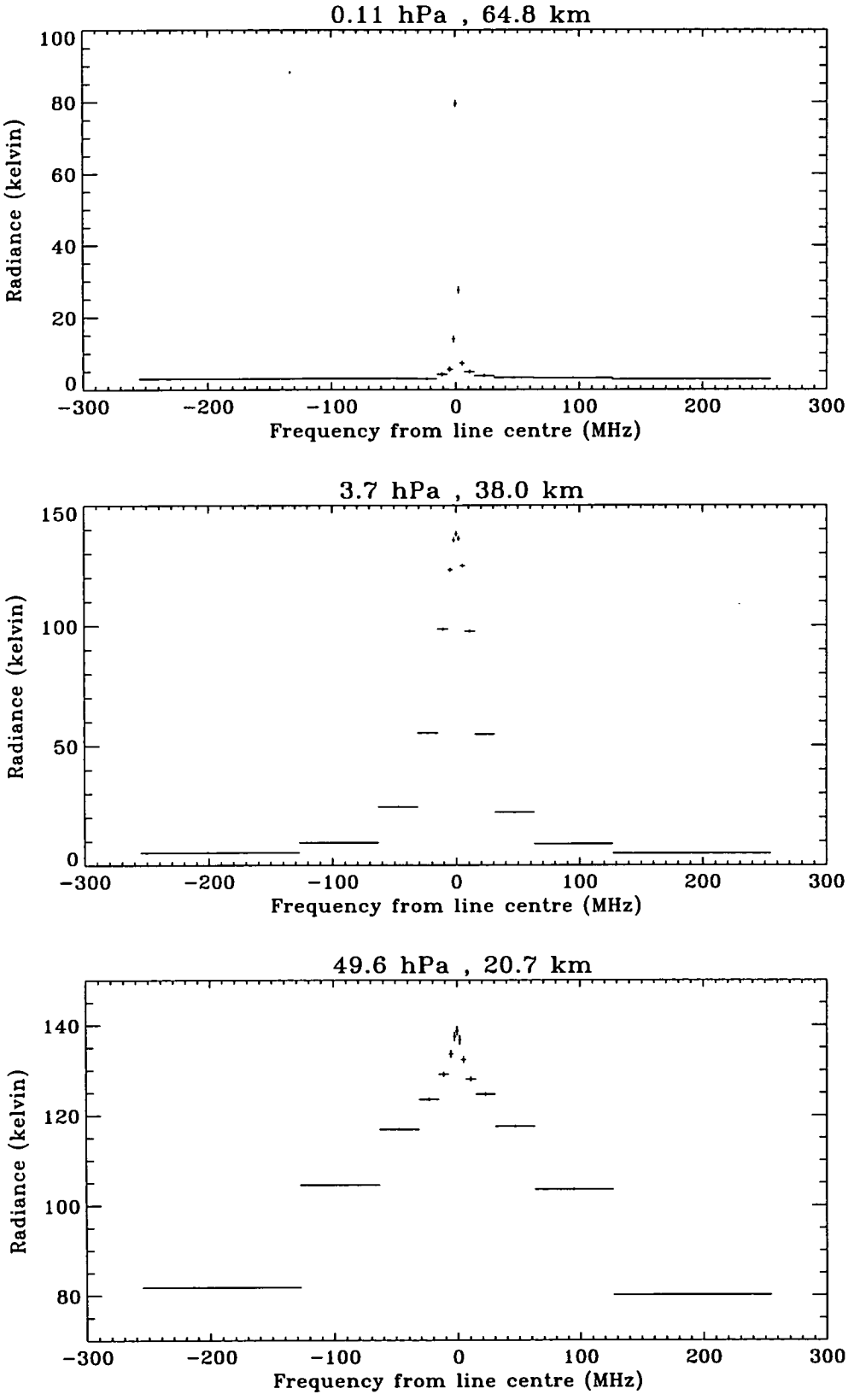

Figure 3.3: Measured limb radiance spectra for channels 1–8 of band 5

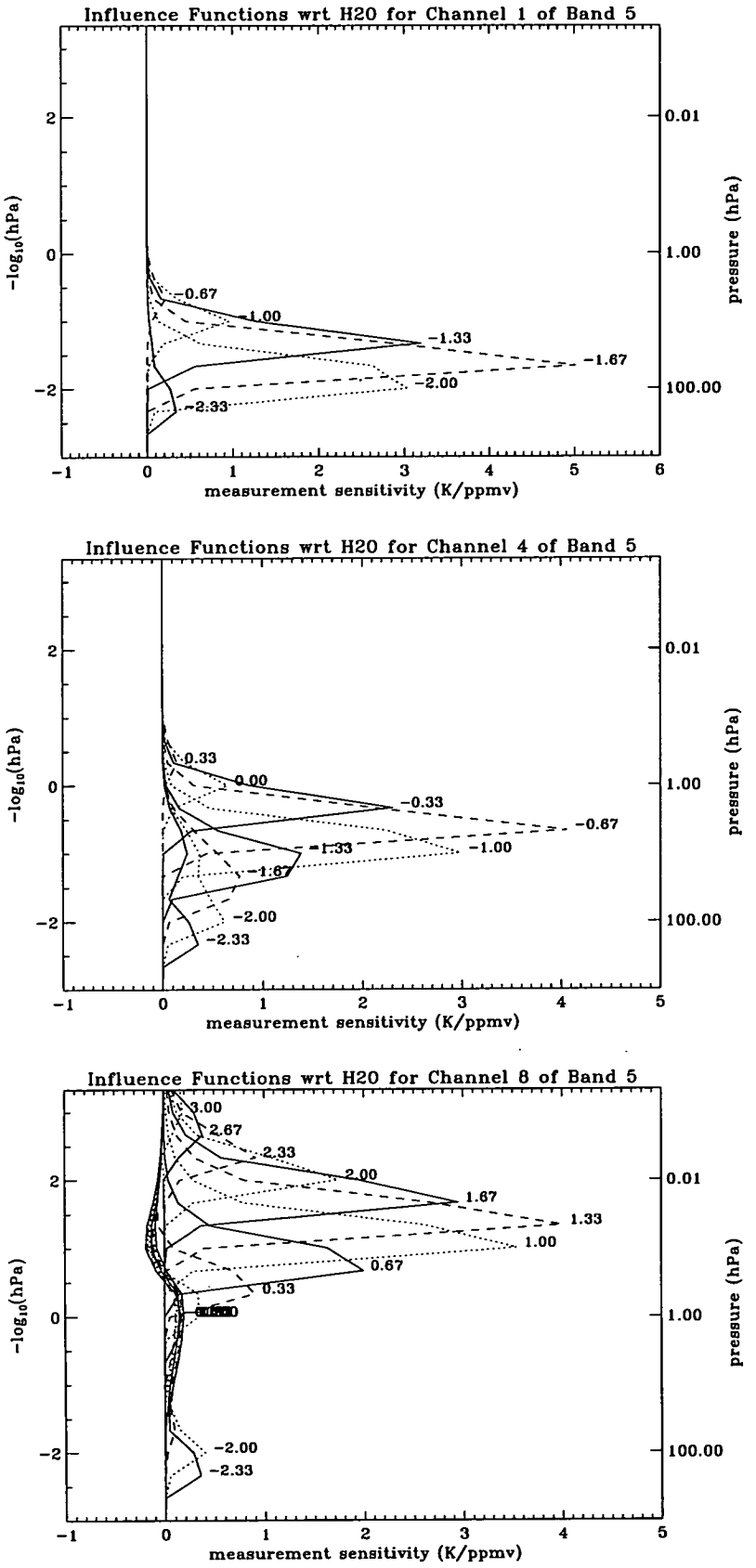

Figure 3.4: Influence functions for band 5 with respect to H_2O

mixing ratio in the lower stratosphere. Channel 4, which is centred at 23 MHz away from line centre, is most sensitive to H_2O in the upper stratosphere. For channel 4, the region of sensitivity to H_2O occurs higher in the atmosphere than that for channel 1 as the effects of pressure broadening do not need to be so great to produce a significant signal in channel 4. In the lower stratosphere, channel 4 shows less sensitivity to H_2O than channel 1 since, in this region, the channel 4 signal is close to saturation. Channel 8 is positioned at line centre and is therefore sensitive to H_2O perturbations at greater altitudes than the other channels. From the bottom panel of figure 3.4, it can be seen that channel 8 is most sensitive to H_2O for tangent pressures in the upper mesosphere. The sensitivity decreases into the thermosphere as the received signal reduces due to the diminishing number density of H_2O molecules. The signal in channel 8 is saturated in the primary sideband at pressures of around 1 hPa and below, and so the radiances are insensitive to perturbations in H_2O at tangent pressures in this region. Some sensitivity to H_2O is apparent in the lowermost stratosphere; this is due to the contribution of the signal in the image sideband of channel 8. Use of all 15 channels of band 5 gives sensitivity to H_2O mixing ratio from the lower stratosphere to the upper mesosphere. Influence functions with respect to other parameters, such as atmospheric temperature and pressure, can be evaluated but are not shown in this thesis.

3.2 Retrieval Contribution Functions

Radiances from all 15 channels of band 5 are used in the retrieval of H_2O mixing ratio profiles. The retrieval grid consists of 20 levels at $z = -3.0 + \frac{n}{3}$ where n = 0,...,19 and z is in units of $-\log_{10}$(hPa). Thus the retrieval grid covers the vertical range of 1000 hPa to 4.6 x 10^{-4} hPa. In the case of MLS, the *a priori* inputs to the retrieval are based on a month-dependent climatology developed by the UARS science team [*inter alia MAP Handbook 31, 1989*]. The UARS H_2O climatology [*Remsberg et al., 1990*] consists mainly of monthly zonal means from the Limb Infrared Monitor of the Stratosphere (LIMS) [*Russell et*

al., 1984] for seven months (November – May), 100 hPa to 1.5 hPa and 56°S to 84°N. From 1.5 hPa to 0.5 hPa, radiance averaged profiles from LIMS data are used. Besides the LIMS data, ground-based microwave data [see, for example, *Bevilacqua et al., 1985, 1987; Tsou et al., 1988*] are used in the mesosphere for pressures of 0.5 hPa to 0.01 hPa. The H_2O UARS climatology was extended to the whole of the year by assuming hemispheric symmetry in the seasons. Extensions where UARS climatology is unavailable make use of default values which were constructed from the Caltech/JPL photochemical model for a mid-latitude equinox day. For Version 3 of the MLS H_2O retrieval, a diagonal *a priori* covariance matrix is used. In the stratosphere the assumed *a priori* uncertainty is set to 2 ppmv. By comparison, the standard deviation about the zonal mean of typical LIMS H_2O profiles for May and October tends to be less than 1 ppmv throughout most of the stratosphere [*Remsberg et al., 1990*]. This suggests that an *a priori* error of 2 ppmv for MLS H_2O retrievals in the stratosphere is unlikely to overconstrain the solution to the input climatology. Tests with significantly larger *a priori* errors gave results which were negligibly different from the standard retrievals within the useful vertical range of the data [*Froidevaux, personal communication, 1993*]. The useful vertical range of the MLS Version 3 H_2O retrieval is discussed later in this chapter.

Contribution functions (defined in Chapter 2) for the retrieval of H_2O mixing ratio profiles from MLS band 5 have been evaluated algebraically by using equation (2.22) of Chapter 2. The *a priori* covariance matrix employed here is purely diagonal with elements equivalent to those used in the Version 3 retrieval. This assumes that there is no correlation in the variability of the *a priori* mixing ratios between the levels of the above defined retrieval grid. The measurement error covariance matrix is also purely diagonal; this assumes that there is no correlation in radiance noise between channels and also between limb views within a particular channel. The calculation of the contribution functions also takes into account the effect of the opacity criterion which is described in Chapter 2. The radiances in band 5 are sensitive not only to H_2O mixing ratio, but to other parameters such as atmospheric temperature and

tangent pressure. These parameters are considered as constrained, i.e., their values are not updated during the retrieval of H_2O but uncertainties in their values are taken into account. Thus, in evaluating the contribution functions for H_2O, the influence functions and associated uncertainties for these parameters are included. For temperature and tangent pressure, the associated uncertainties are taken to be the retrieved error from the Version 3 retrieval as both temperature and tangent pressure are retrieved using radiances from band 1 prior to the retrieval of H_2O from band 5 radiances. Since the influence functions are evaluated on a fixed grid of tangent pressures (see above), they are linearly interpolated onto a typical MLS limb scan before being employed in the calculation of the contribution functions.

The three panels in figure 3.5 show H_2O contribution functions for selected radiance measurements in channels 1, 4 and 8 of band 5 for a typical mid-latitude retrieval. The vertical axis represents the pressure level of the retrieved mixing ratio, the horizontal axis represents the sensitivity of the retrieved mixing ratio to perturbations in the measured radiance and is in units of ppmv/kelvin. Each plotted line represents a column of the H_2O contribution function matrix, i.e., the contribution of a perturbation in a single radiance measurement to the retrieved profile. The number printed at the maximum or minimum value (depending on which has the largest absolute value) of each contribution function represents the tangent pressure, in units of $-\log_{10}$(hPa), of the associated radiance measurement. The oscillatory nature of the contribution functions, due to overlapping influence functions as discussed in Chapter 2, is evident in these plots. In the top panel it can be seen that perturbations in channel 1 radiances in the lower stratosphere contribute to the retrieved profile in the lower stratosphere. In the middle panel, perturbations in channel 4 radiances in the upper stratosphere contribute to the retrieved profile mainly in the upper stratosphere although a perturbation in the radiance measurement at $z = -0.67$ (4.6 hPa) appears to affect the retrieved profile in the lower stratosphere also. In the bottom panel, perturbations in channel 8 radiances in the upper mesosphere and lower thermosphere

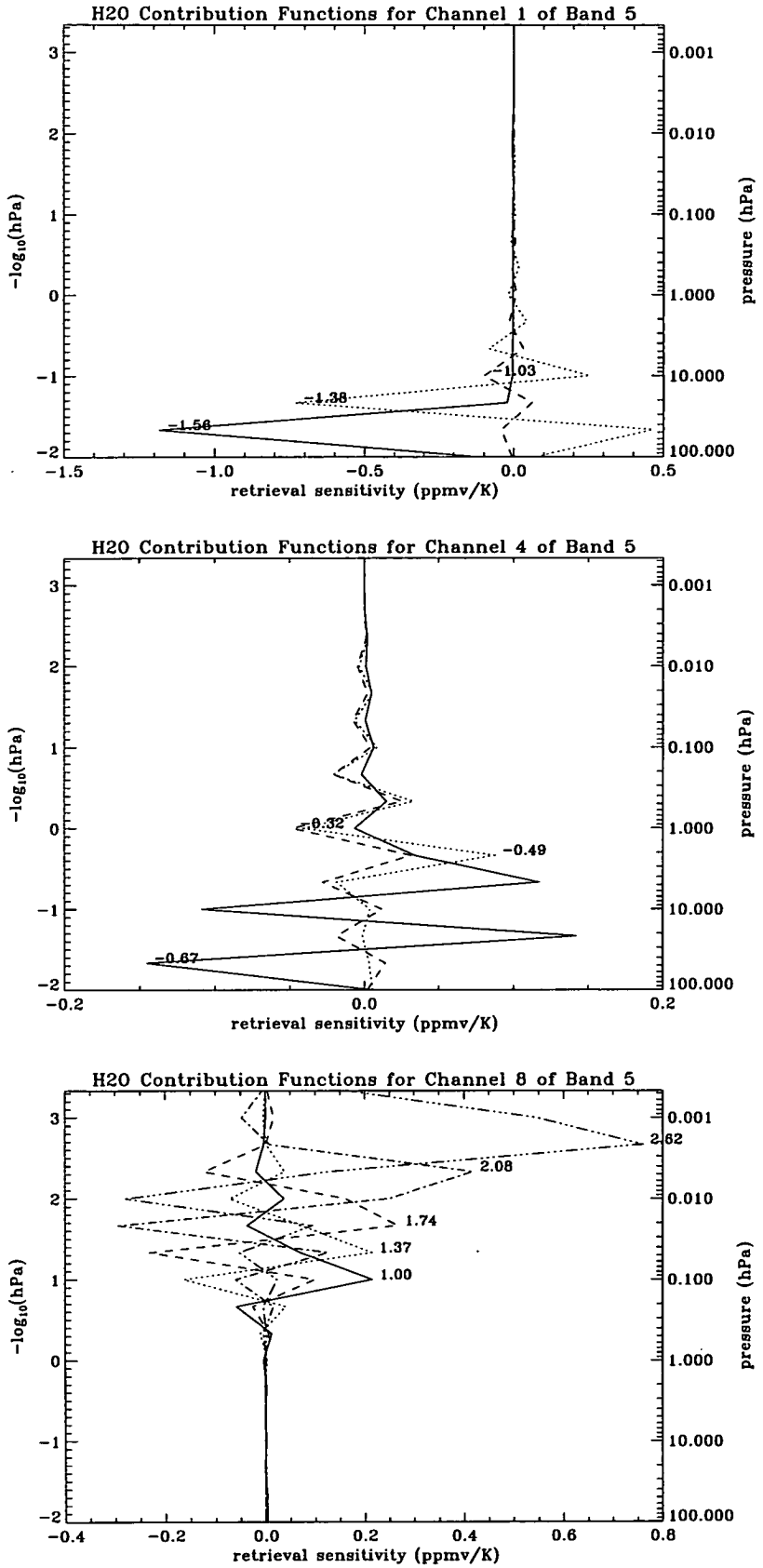

Figure 3.5: H_2O contribution functions for band 5

are seen contribute to the retrieved profile in that region of the atmosphere.

3.3 Averaging kernels and *a priori* contribution

In this section the nature of the averaging kernels (defined in Chapter 2) for MLS H_2O retrievals is discussed and a measure of the vertical resolution of the retrievals is given. Also, an indication of the contribution of the *a priori* information to the retrieved mixing ratio is presented.

Averaging kernels

Averaging kernels for H_2O have been calculated algebraically using equation (2.24) of Chapter 2. Figure 3.6 shows rows of the MLS H_2O averaging kernel matrix for a typical mid-latitude retrieval. Each row of the averaging

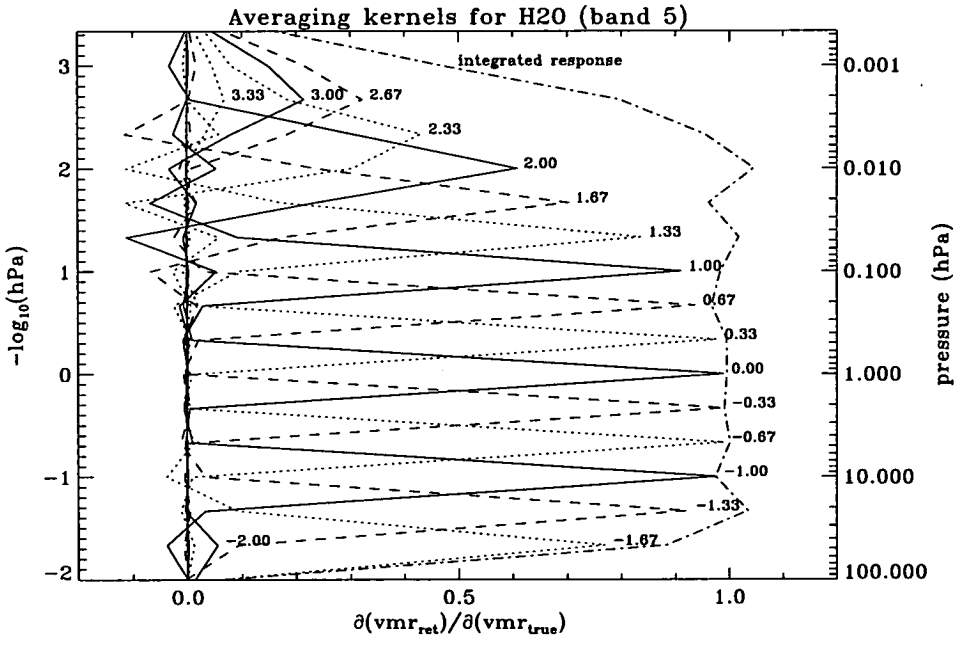

Figure 3.6: Averaging kernels for H_2O retrieval

kernel contains the scaling factors that determine how perturbations in each level of the real atmosphere are reproduced in a particular level of the retrieved profile. The vertical axis represents the pressure levels of the real atmosphere, the horizontal axis represents the magnitude of the scaling factors. The num-

bers printed to the right of each averaging kernel peak represent the pressure level, in units of $-\log_{10}$(hPa), of the retrieval associated with that particular row of the averaging kernel. The 'ideal' shape, indicating that an atmospheric perturbation is perfectly retrieved, is represented by a response of magnitude 1 at the perturbed level and 0 elsewhere. It can be seen that the shape of the averaging kernel is close to ideal for retrieval levels from $z = -1.33$ to 0.67 (22 hPa to 0.2 hPa). At $z = -1.67$ (46 hPa) the peak magnitude is 0.8 and at $z = -2.0$ (100 hPa) the peak magnitude is less than 0.1. This reflects the effect of the opacity criterion which discards measurements that are deemed to be optically thick. Generally, for band 5, measurements with associated tangent pressures greater than about 40 hPa are not included in the retrieval of H_2O. Thus, the retrievals at 100 hPa and below contain very little or no information content from the measurements and therefore produce values close to the *a priori* amounts. Above $z = 0.67$ (0.2 hPa) the magnitude of the averaging kernel peak reduces and the width of the function increases as the altitude of the retrieval level increases. The reason for this is two-fold: (1) in this region of the atmosphere the measured signal decreases with height due to the diminishing number density of molecules and so the signal-to-noise ratio decreases; (2) in the upper mesosphere and lower thermosphere the MLS limb views are further apart than at lower levels in the atmosphere (see Chapter 1) and this tends to widen the averaging kernels. Also shown on the plot is the integrated response i.e., the sum over a column of the averaging kernel matrix. This represents a measure of the response of the whole retrieved profile to a perturbation at a particular level in the real atmosphere. If the integrated response is less than unity, then the missing component is supplied by the *a priori* information. From figure 3.6 it can be seen that from $z = -1.33$ to 2.0 (22 hPa to 0.01 hPa) the integrated response is close to unity.

Vertical resolution

The width of the averaging kernels gives a measure of the vertical resolution of the retrieval; broadening of the kernels indicates a loss of vertical resolution

due to the retrieval process. In figure 3.7 a measure of the vertical resolution of the MLS H_2O retrievals is plotted. The measure of vertical resolution

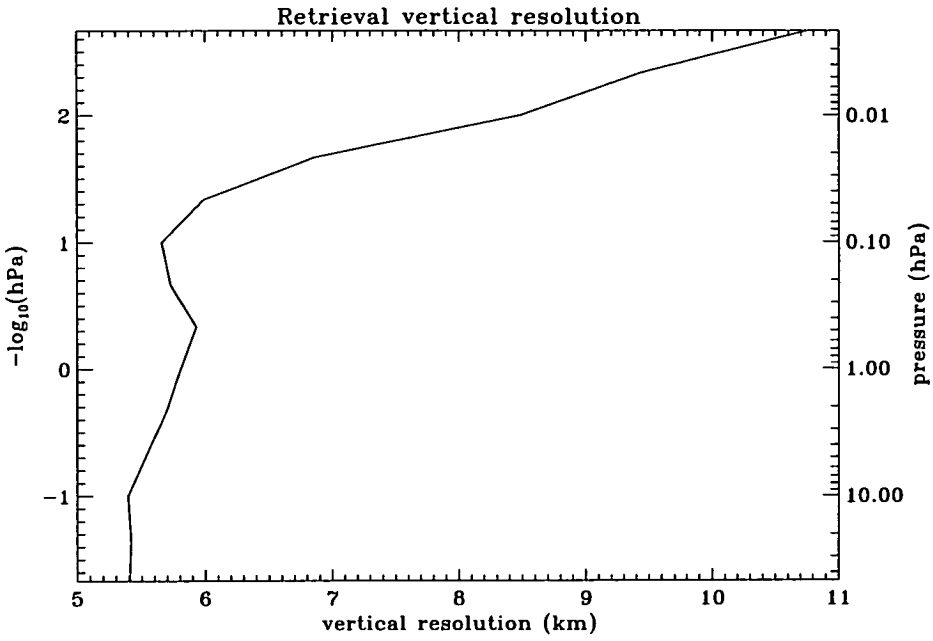

Figure 3.7: Vertical resolution of H_2O retrieval

plotted here is the full width at half-maximum which will be denoted $\Delta_{\frac{1}{2}}$. This measure is only valid where the averaging kernels are well-peaked and do not have large side-lobes, and the maximum occurs at the desired pressure level. For this reason, $\Delta_{\frac{1}{2}}$ is plotted from $z = -1.67$ to 2.67 (46 hPa to 0.002 hPa) only. Between $z = -1.67$ (46 hPa) and 1.33 (0.046 hPa) the vertical resolution is seen to lie between 5 and 6 km. Above this there is an increasing loss of vertical resolution with altitude due to the combined effects of the wider scan pattern and the decreasing signal-to-noise ratio.

Effect of *a priori* information

In order to establish the effect of the *a priori* information on the retrieved profile it is useful to look at the nature of the matrix (**I**–**A**), where **I** is the identity matrix and **A** is the averaging kernel matrix. This matrix represents the sensitivity of the retrieval to the *a priori* information and, from equation (2.38), each row of (**I**–**A**) gives the scaling factors which determine the weight

given to each level of the *a priori* profile for a particular level of the retrieved profile. Figure 3.8 shows the rows of (I–A) for the retrieval of H_2O. The

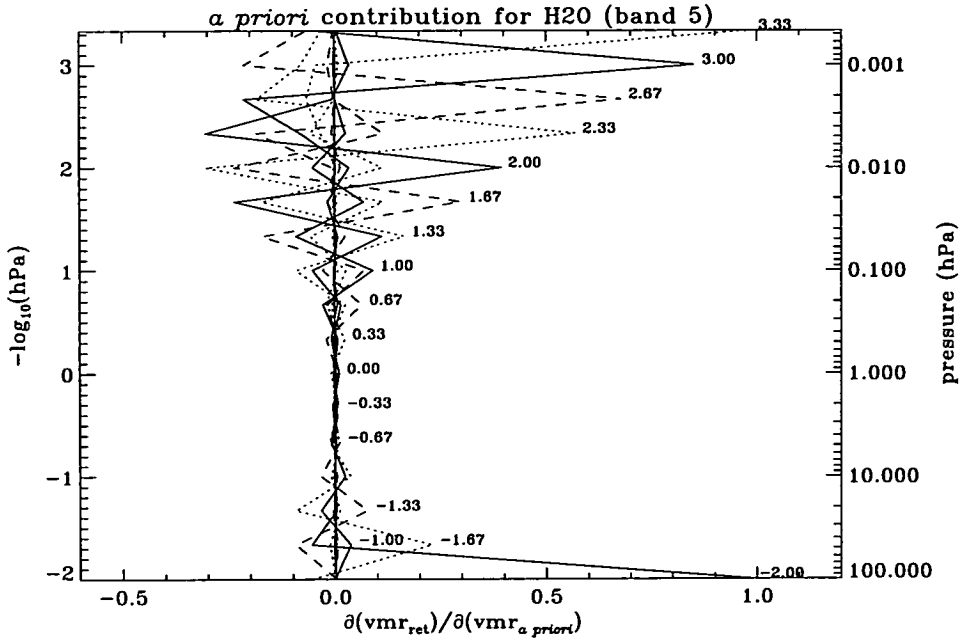

Figure 3.8: Sensitivity of the H_2O retrieval to *a priori*

vertical axis represents the pressure level of the *a priori* profile which is on the same grid as the retrieved profile, the horizontal axis represents the sensitivity of the retrieval to the *a priori* information. The numbers printed to the right of the maxima of the functions represent the pressure, in units of $-\log_{10}$(hPa), of the retrieval level associated with that row of (I–A). It can be seen that the *a priori* information has very little contribution between 46 hPa and 0.1 hPa, and its contribution increases with altitude throughout the upper mesosphere and lower thermosphere. At 100 hPa the retrieval of H_2O is dominated by the *a priori* information.

As discussed in Chapter 2, a useful method of understanding how matrix weights affect the retrieval solution is to use an eigenvector decomposition. As a reminder, from equation (2.41), eigenvectors of the averaging kernel matrix, **A**, with eigenvalues close to a value of 1 represent structures that will be well reproduced by the measurement system, whereas, eigenvectors with cor-

responding eigenvalues close to 0 will represent structures which come mainly from the *a priori* information. The eigenvectors of the averaging kernel matrix for the retrieval of H_2O are plotted in figure 3.9; the corresponding eigenvalues, λ, are printed at the top of each panel in the figure. It can be seen that the eigenvectors with corresponding eigenvalues close to 0 (the first seven eigenvectors) contain vertical structure mainly below 100 hPa with some small scale structure around 0.01 hPa and above. This implies that the *a priori* information contributes to components in the retrieved profile below 100 hPa and to the small scale structure of components around 0.01 hPa and above. The last eight eigenvectors plotted have corresponding eigenvectors greater than 0.95 and therefore show the vertical structures that arise from the measurements. Thus, it can be seen that the measurements reproduce well the fairly broad vertical structures. The eigenvectors with corresponding eigenvalues significantly greater than 0 but also significantly less than 1 correspond to vertical structures that contain contributions from both the measurements and the *a priori* information.

It should be noted that the averaging kernels shown in this section were calculated using a representation of the true atmospheric profiles identical to the relatively coarse MLS retrieval grid. However, the true profile is actually continuous, and using a higher resolution representation for the true profile may alter the shape of the averaging kernels. In Chapter 5, the effect of using a representation of higher resolution for the true profile, when evaluating the averaging kernels, is discussed.

From the information given by the averaging kernels, the useful vertical range for Version 3 H_2O retrievals would be 46–0.01 hPa. However, there are known artefacts in the Version 3 H_2O data which lead to a more restricted useful vertical range. Firstly, in the mesosphere, there are frequently-occurring high mixing ratios at $\sim$ 0.1 hPa which seem unrealistic [*Lahoz et al., 1994*]. Secondly, there is an apparent loss of information from the measurements in the lower stratosphere at high latitudes during winter which results in a higher than normal contribution from the *a priori* information to the retrievals,

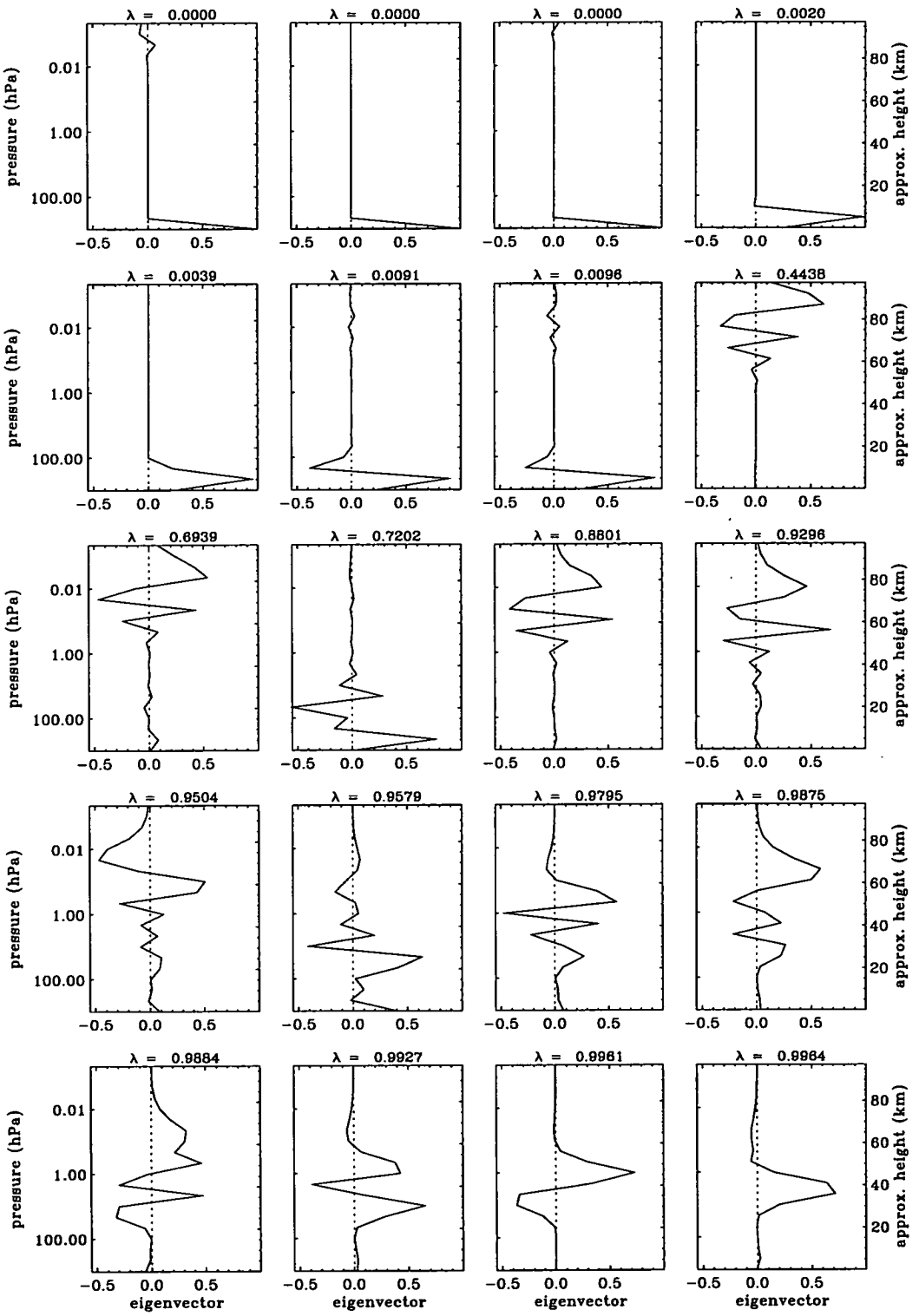

Figure 3.9: Eigenvectors of H_2O averaging kernel matrix

particularly at 46 hPa (see Chapter 4). Thus, the useful vertical range for scientific studies with Version 3 H_2O data is 22–0.2 hPa at high latitudes and 46–0.2 hPa elsewhere.

3.4 Error Analysis

In this section, an error analysis based on the formalism of *Rodgers, [1990]* (see Chapter 2) is presented for the retrieval of H_2O from band 5 of MLS. Estimates of both random and systematic errors are given along with an estimate of the smoothing error which arises from the retrieval process. The resulting estimated errors from this analysis are compared with typical retrieval errors produced by the MLS Version 3 algorithms.

3.4.1 Random errors

Three sources of random error are investigated in this analysis, namely (1) noise on the measured radiances, (2) uncertainty in the retrieved atmospheric temperature and (3) uncertainty in the retrieved tangent pressure.

From equation (2.32) in Chapter 2, the contribution of the measurement noise to the retrieval error covariance is $\mathbf{S}_M = \mathbf{D}\mathbf{S}_\epsilon\mathbf{D}^T$ where $\mathbf{S}_\epsilon$ is the measurement error covariance matrix, $\mathbf{D}$ is the contribution function matrix for the retrieval of H_2O and $\mathbf{D}^T$ is the transpose of $\mathbf{D}$. The values of measurement noise used to construct $\mathbf{S}_\epsilon$ were typical noise values produced by the MLS Level 1 processing algorithms [*Jarnot et al., 1994*]. $\mathbf{S}_\epsilon$ is purely diagonal which therefore assumes that there are no correlations in measurement noise both between channels and between different limb views within each channel. Temperature and tangent pressure are retrieved using radiances from band 1 prior to the retrieval of H_2O during which temperature and tangent pressure are constrained parameters. This means that the retrieved values of temperature and tangent pressure are not altered during the retrieval of H_2O but their associated uncertainties are taken into account. In order to assess the effect of random uncertainties in temperature and tangent pressure on the H_2O re-

trieval one can evaluate the contribution of these uncertainties to the retrieval error covariance of H_2O from equation (2.31)

$$\mathbf{S}_P = \mathbf{D}\mathbf{K}_b\mathbf{S}_b\mathbf{K}_b^T\mathbf{D}^T \tag{3.1}$$

where $\mathbf{S}_b$ represents the error covariance matrix of either temperature or tangent pressure, $\mathbf{K}_b$ is the influence function matrix with respect to either parameter and $\mathbf{D}$ is the contribution function matrix for the retrieval of H_2O. The $\mathbf{S}_b$ matrices for both temperature and tangent pressure are constructed by placing the square of the retrieved error in each parameter along the diagonal of the matrix. The off-diagonal elements are set to zero; this assumes that there are no correlations in the retrieved errors for either temperature or tangent pressure. In figure 3.10 the contributions of these random uncertainties to the retrieved error for H_2O are plotted. The vertical axis represents the

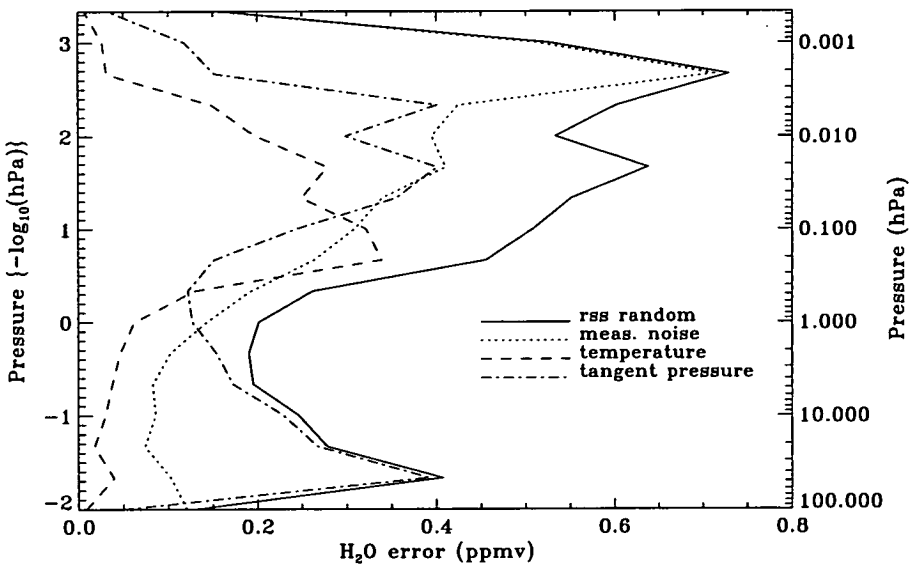

Figure 3.10: Random errors for H_2O retrieval

pressure level of the retrieval and the horizontal axis represents the magnitude of the contribution to the retrieved error in H_2O. For the contribution of measurement noise the square root of the diagonal elements of the matrix $\mathbf{S}_M$ is

plotted, for temperature and tangent pressure the square root of the diagonal elements of the matrix $\mathbf{S}_P$ for both parameters is plotted. Also plotted is the root-sum-square (rss) of the above three contributions. It can be seen that the contribution from the measurement noise generally increases with altitude. This is due to two reasons. Firstly, the measured signal decreases with increasing altitude (see figure 3.2) due to the decreasing number density of molecules and this decreases the signal-to-noise ratio. Secondly, with increasing altitude, the measured signal is confined more to the channels towards the centre of the band (see figure 3.3). The bandwidth of the channels decreases towards the band centre (see Table 1.2) and this decreasing bandwidth increases the noise level on the measurements. The contribution from the uncertainty in retrieved temperature appears to increase sharply in the lower mesosphere. At pressure levels above 0.46 hPa the temperature retrieval relaxes to the *a priori* values and the *a priori* uncertainty in temperature is 20 kelvin [*Fishbein et al., 1994*], between 22 hPa and 1 hPa the retrieved uncertainty in temperature is generally less than 5 kelvin. Below 1 hPa the random error in retrieved H_2O seems to be dominated by the uncertainty in the retrieved tangent pressure.

In Chapter 2, a method of conceptualising error covariance matrices was introduced. This involved evaluating the orthogonal quantities $\mathbf{e}_i = \lambda_i^{\frac{1}{2}}\mathbf{l}_i$ where λ_i and $\mathbf{l}_i$ are the eigenvalues and eigenvectors, respectively, of the error covariance matrix. The orthogonal quantities, $\mathbf{e}_i$, known as error patterns, represent independent components of the error. In figure 3.11 the first nine error patterns for the $\mathbf{S}_M$ matrix are plotted. The eigenvalue associated with each error pattern is printed at the top of each panel. The first three error patterns (corresponding to the error patterns with largest associated eigenvalues) show that the dominant components in the error which are contributed by the measurement noise occur above 1 hPa and have a vertical wavelength of around 10–15 km. The error patterns with small associated eigenvalues show the components that are represented well by the measurements and hence do not contribute much to the retrieved error. These components tend to be a mixture of very broad scale structure and some finer scale structure in the

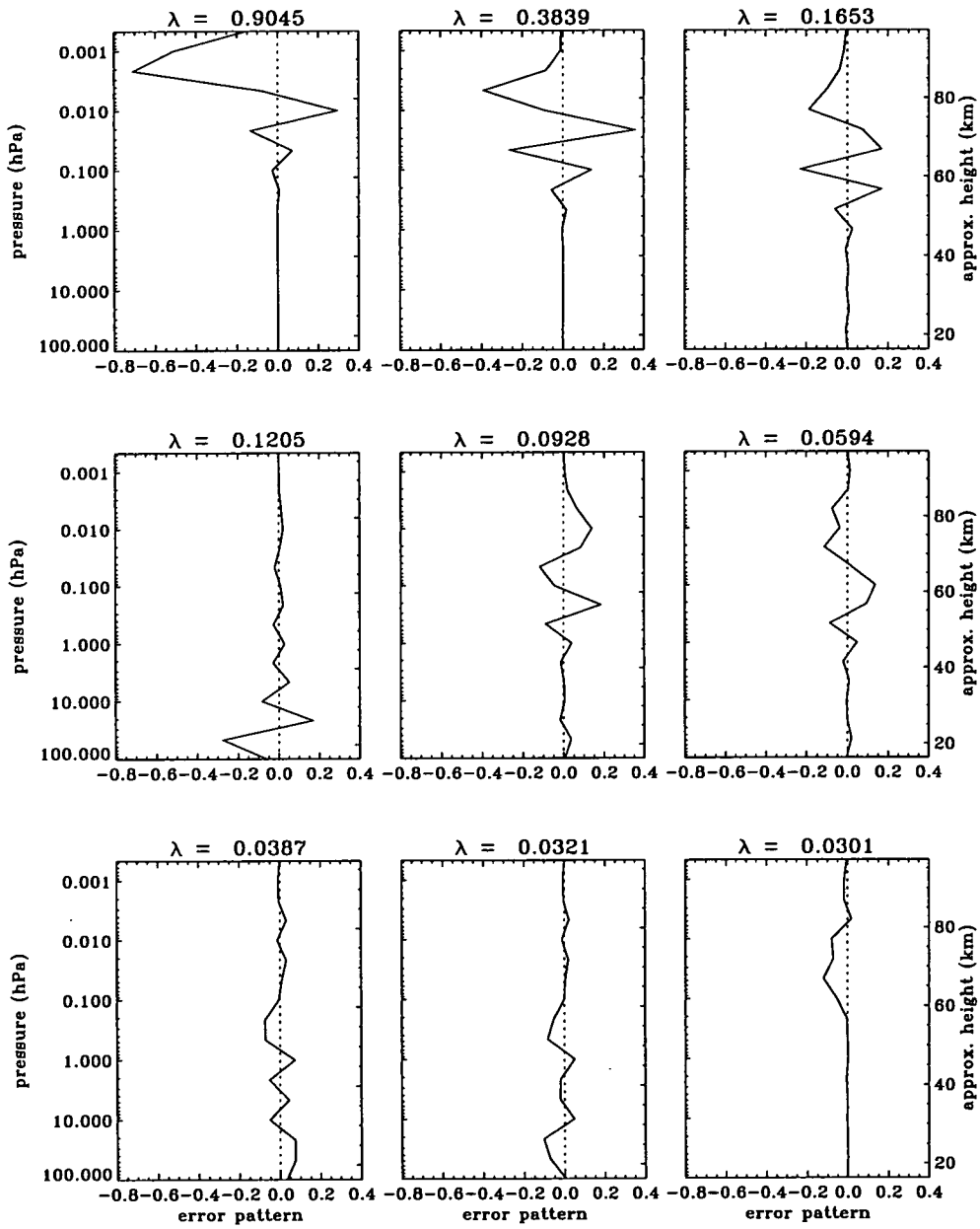

Figure 3.11: Error patterns for measurement noise

stratosphere.

Comparison with observed variability

The random errors described above contribute to the variability that would be expected if the same region of the atmosphere was measured repeatedly and so should provide a measure of the precision of the H_2O retrievals. It is therefore useful to compare these random errors with the measured variability of the MLS H_2O retrievals. In figure 3.12 a comparison of the rss random error from the above analysis with the measured variability of the MLS H_2O retrievals is given. In the figure, the solid line, labelled (1), represents the rss

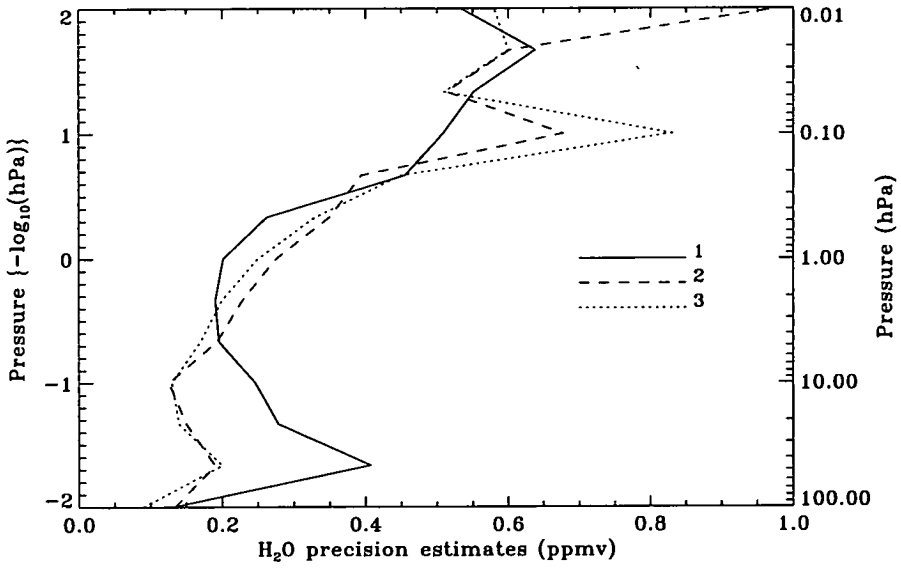

Figure 3.12: Precision estimates for H_2O. For meaning of lines see text.

random error from the above analysis. The dashed line, labelled (2), represents the rms difference between pairs of profiles near the orbit turning points (near 80°N or 80°S) in the summer hemisphere. It is at these latitudes that the densest sampling occurs and the summer hemisphere is chosen to minimise any effects from atmospheric variability. These profile pairs are less than 2 hours apart in time and are separated by less than 150 km. The time period used was 19th July 1992 to 8th August 1992 which gave 241 pairs of profiles

near to 80°N. The dotted line, labelled (3), shows the variability of retrieved profiles in the tropics where the atmospheric variability is usually small. It is a result of calculating the standard deviation of retrieved profiles in the latitude range 5°N–5°S for each one of 442 days and averaging the standard deviations over these days.

Both measures of the variability of the retrievals (lines 2 and 3) are in reasonable agreement with each other. The effect of the frequently-occurring high values at 0.1 hPa can be seen in an increase in the variability of the retrievals at that pressure level. The variability of the retrievals is small at 100 hPa since at this level the retrieval is dominated by the *a priori* information. It can be seen that, above 5 hPa, the rss random error (line 1) from the error analysis above compares reasonably well with the measured variability, except at 0.1 hPa where the above mentioned frequently-occurring high values affect the measured variability. Between 5 hPa and 46 hPa, the rss random error is 0.1–0.2 ppmv larger than the measured variability of the retrievals. In this region of the atmosphere the rss random error is dominated by the uncertainty in the retrieved tangent pressure. However, the uncertainties in retrieved tangent pressure that are incorporated into the formal error analysis above may include some significant systematic effects, especially in the lower stratosphere [*Fishbein et al., 1994*]. Therefore, the error analysis above may lead to an over estimate of the random error, especially in the lower stratosphere.

Smoothing error

The random errors considered in the analysis above contribute to the variability in the retrievals that would be expected if the same region of the atmosphere was measured repeatedly. However, there is a further contribution to the error on a retrieved profile which is not a random error in the same manner as the random errors described above. This error is known as the smoothing error (see Chapter 2) and can be regarded as the contribution of the *a priori* error to the retrieved error. This error depends on differences between the true profile and the *a priori* profile and can be evaluated using equation (2.30) of

Chapter 2. The smoothing error for the retrieval of H_2O has been evaluated by this method and is plotted in figure 3.13. The *a priori* covariance matrix used in this calculation is the same as that used in the MLS Version 3 retrievals, which is a purely diagonal matrix with the diagonal elements between 100 hPa and 4.6 x 10^{-4} hPa set to 4 ppmv^2. Setting all non-diagonal elements to zero, assumes that no inter-level correlations exist. It can be seen that, in the lower

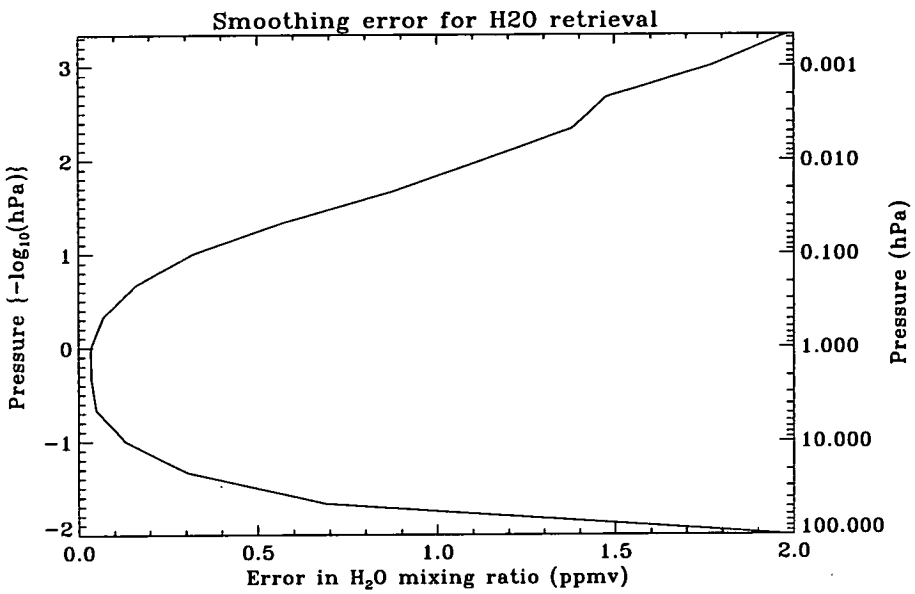

Figure 3.13: Smoothing error for H_2O retrieval

stratosphere, the smoothing error increases with pressure until it becomes equal to 2 ppmv (the *a priori* error) at 100 hPa. This is due to the increasing optical thickness of the MLS limb views as tangent pressure increases. The retrieval method does not use radiance measurements which arise from limb paths that are deemed to be optically thick. Thus, with increasing pressure in the lower stratosphere, the retrievals use less and less radiance measurements until, at 100 hPa, there is no information from the measurements and all the contribution is from the *a priori* information. Upwards from 1 hPa, the smoothing error increases due to the decreasing signal-to-noise ratio in the band 5 measurements and the wider scan pattern in this region until, at 4.6

x 10^{-4} hPa, the retrieval contains virtually no information from the measurements and is dominated by the *a priori* information.

It should be noted that the averaging kernels used in the calculation of this smoothing error are those presented earlier in this chapter. These averaging kernels were calculated using a representation of the true atmospheric profiles identical to the relatively coarse MLS retrieval grid. However, the true profile is actually continuous, and so any estimate of the amount of smoothing that results from both the measurement technique and the retrieval process may be an underestimate. This is particularly important for MLS H_2O in the upper stratosphere and lower mesosphere, where the measurement sensitivity is good, but the smoothing error presented here will only reflect the amount of smoothing from the already relatively coarse representation of the true profile. In Chapter 5, the effect of using a representation of higher resolution for the true profile when evaluating the averaging kernels and the resulting smoothing error is discussed. Also, in Chapter 5, the effect of including non-zero off-diagonal elements in the *a priori* error covariance matrix is discussed.

It is useful to look at the error patterns (see Chapter 2) produced by the smoothing error. These patterns are proportional to the eigenvectors of the covariance matrix for the smoothing error, $\mathbf{S}_S$, and represent the orthogonal structures that the observing system cannot see. Figure 3.14 shows the first nine error patterns for the contribution of the smoothing error to the overall retrieval error. The eigenvalues associated with each error pattern are printed at the top of each panel. These error patterns tend to have larger values in the upper mesosphere and lower thermosphere, and in the lower stratosphere, where the *a priori* information contributes most to the retrieved profile. The scale of these structures tends to be finer than that for the error patterns for the measurement noise contribution (see figure 3.11 above). Thus, the measurements tend to contribute the broad-scale components to the error whereas the *a priori* information supplies the fine-scale structure. Here, any structures of scale finer than the retrieval grid cannot be represented.

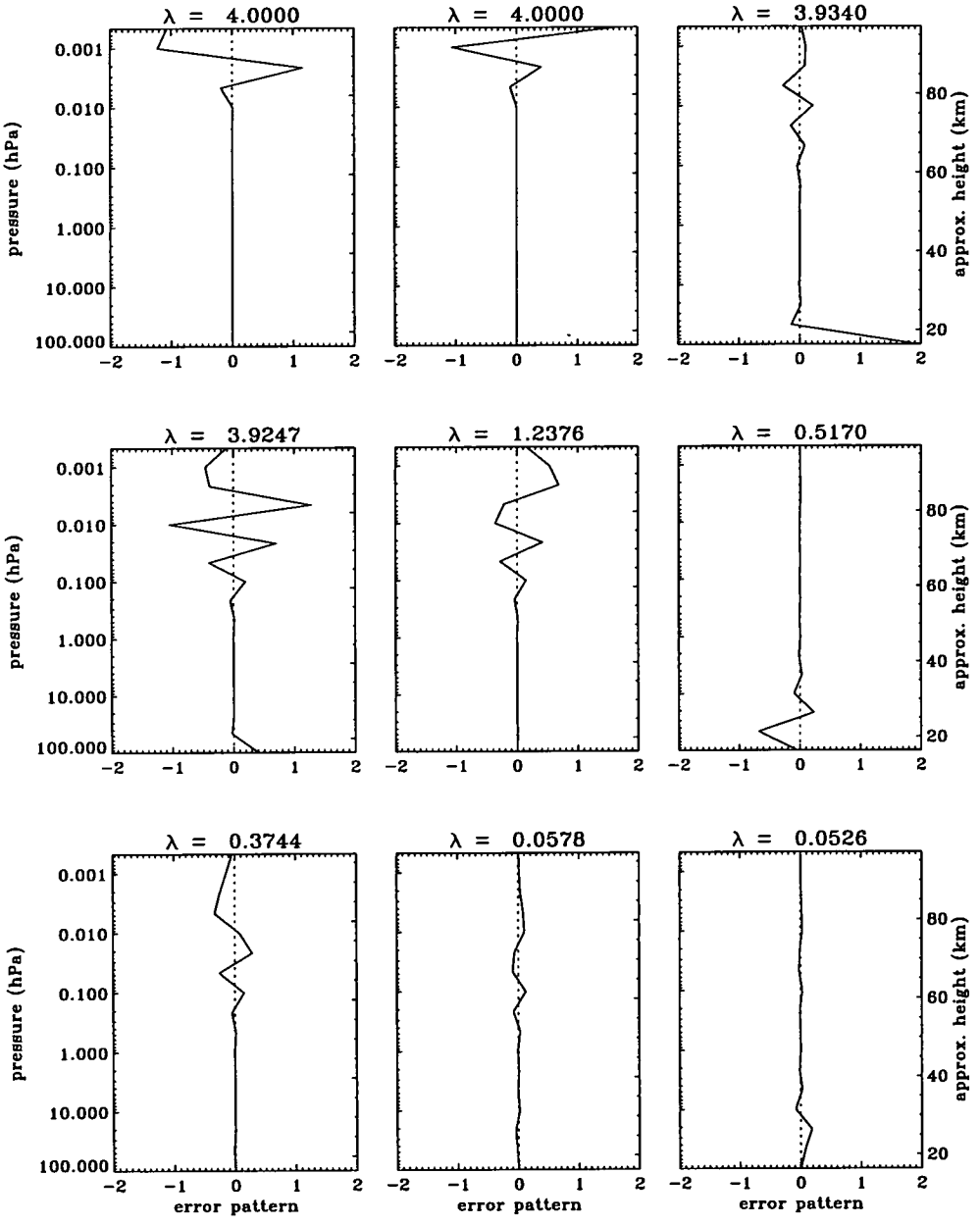

Figure 3.14: Error patterns for smoothing error

3.4.2 Systematic errors

In addition to random errors, it is necessary to consider systematic errors. These may arise from uncertainties in forward model parameters or from uncertainties in the calibration of the instrument. In the following analysis of systematic errors, two methods were employed to estimate the effects of systematic uncertainties on the retrieved H_2O. One method, which was used mainly with instrument calibration parameters, was to estimate the resulting error in measured radiance due to uncertainty in the parameter in question and, using knowledge of any correlations in such errors, construct an error covariance matrix, **E**. This error in measured radiance can then be mapped into errors in retrieved H_2O mixing ratio by equation (3.2) (essentially replacing the term $\mathbf{K}_b\mathbf{S}_b\mathbf{K}_b^T$ in equation (2.31) by **E**),

$$\mathbf{S}_P = \mathbf{DED}^T \tag{3.2}$$

where **D** is the contribution function matrix for the retrieval of H_2O and $\mathbf{S}_P$ gives the contribution of uncertainties in the parameter, P, to the error in retrieved H_2O mixing ratio. The other method, which was used primarily for assessing the effect of uncertainties in forward model parameters, was to perturb the parameter in question and re-run the retrieval algorithms. The results were then compared with a standard run to ascertain the sensitivity of the retrieval to the perturbation of the parameter being studied. This method involved a certain amount of reliance on colleagues at JPL to perform such tests.

Figure 3.15 shows estimates of the dominant systematic errors along with the root-sum-square (rss) of the systematic errors arising from all the sources of uncertainty considered in this analysis. Below, the various sources of uncertainty which were considered are discussed. Firstly, the sources of the dominant systematic uncertainties (see figure 3.15) are discussed.

tangent pressure: Since the retrieved mixing ratios are based on radiances at the retrieved tangent pressure then systematic errors in tangent

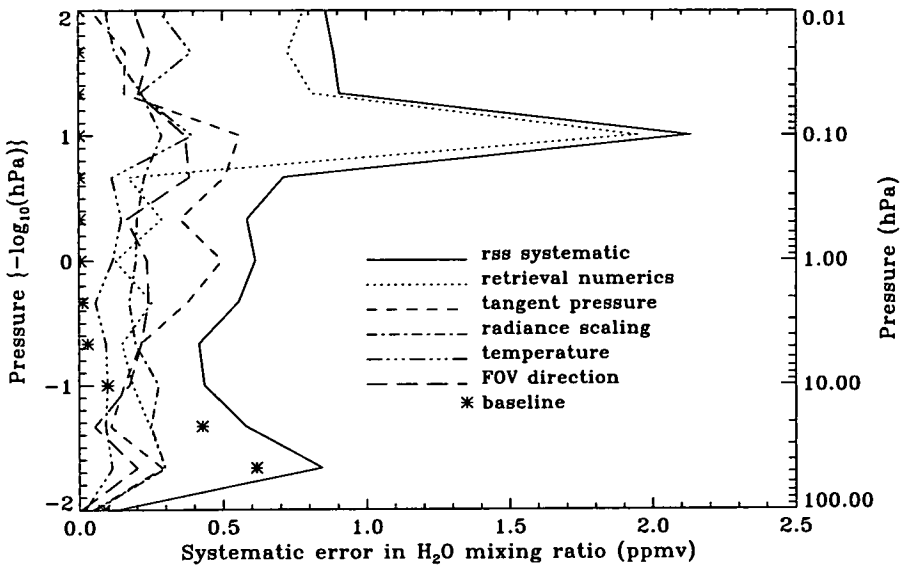

Figure 3.15: Systematic errors for H_2O retrieval

pressure can produce systematic errors in mixing ratio. Sensitivity tests were performed assuming a systematic error in tangent pressure of about 6 % [see *Fishbein et al., 1994*]. The main source of this systematic error is from possible errors in the O_2 spectroscopic data base. It can be seen from figure 3.15 that these errors tend to dominate the systematic error between 2 hPa and 0.2 hPa.

temperature: Systematic errors in temperature can lead to systematic errors in mixing ratio since the measured radiances depend somewhat on the temperature (see Chapter 2). Sensitivity tests were performed taking biases in temperature to be 2 K for latitudes equatorward of 60 degrees and 5 K for latitudes poleward of 60 degrees. These biases are consistent with observed average differences between MLS and NMC (National Meteorological Centre) temperatures [see *Fishbein et al., 1994*]. Tangent pressure was retrieved while the temperature biases were imposed. The resulting changes in H_2O mixing ratio were then analysed. At mid-latitudes for a 2 K systematic error in temperature, the systematic uncertainty in H_2O mixing ratio is generally about 0.1 ppmv below 0.2 hPa, and 0.2–0.4 ppmv above 0.2 hPa.

retrieval numerics: this refers to the differences between the mixing ratio profiles used to create simulated noise-free radiances, and the subsequent retrieved profiles based on these radiances using the inversion algorithm. From figure 3.15, it can be seen that these errors are generally 0.2–0.3 ppmv, but at 0.1 hPa this error is 2 ppmv and may account for the unrealistically high mixing ratios which can sometimes occur at this pressure level.

radiance scaling: three sources of scaling errors in calibrated radiances are radiometric calibration, sideband ratio errors and spectroscopic errors in linestrength. The first two error sources are discussed by *Jarnot et al.* [*1994*]. Based on this reference, a systematic uncertainty of 0.6 % was used for the radiometric calibration of the 183 GHz radiometer. This uncertainty is due mainly to uncertainties in the pre-launch characterisation of losses through the MLS antenna and switching mirror. A covariance matrix of radiance errors from this source was constructed which assumes the errors are fully correlated across the band and with height. Errors in the sideband ratios can lead to possible errors in single sideband radiance of $\sim$ 2 % for the 183 GHz H_2O band [see *Jarnot et al., 1994*]. These errors should be correlated in some way across the band but due to lack of knowledge of such correlations a covariance matrix of radiance errors was constructed which assumes no correlation is present. This gives a conservatively high estimate of the resulting uncertainty. For a systematic error in line strength a value of 1 % based on *Pickett et al.* [*1992*] has been used which is probably a conservatively high estimate of the line strength error. Again, a covariance matrix of radiance errors due to this source was constructed which assumes that the errors are fully correlated across the band and with height. The resulting uncertainties in H_2O due to these three sources were combined by taking the root-sum-square uncertainty. This leads to an estimated error in radiance scaling of generally 0.2–0.3 ppmv.

Field of view (FOV) direction: errors in the FOV direction are related to possible errors in misalignment of the 183 GHz radiometer FOV with respect to the 63 GHz FOV. Post launch calibration data from scans of the moon indicate a need for an alignment adjustment of the 183 GHz radiometer FOV

from the pre-launch data (see *Jarnot et al., 1994*). The MLS Version 3 data used a misalignment value of 0.006 degrees which is somewhat less than the result of the studies based on moon-views of 0.011 degrees. In this analysis, an uncertainty of 0.007 degrees in FOV direction has been assumed (this is the uncertainty assumed in the MLS Version 3 data) and this uncertainty has been mapped into H_2O mixing ratio. Systematic errors in retrieved H_2O due to this source of uncertainty are generally 0.2–0.4 ppmv.

baseline: a set of radiance offsets are retrieved, with one component per limb view, as an attempt to quantify the contribution to the measured radiances of any atmospheric constituents which may be missing from the forward model. The *a priori* value for each baseline offset component is based on the retrieved value for the previous (above) limb view. The *a priori* error is set to a conservatively large value of 3 kelvin. Typical errors in the retrieved baseline were mapped into errors in H_2O mixing ratio. The contribution to the retrieved error in H_2O from the error in the baseline is only significant at 10 hPa and below, but dominates the systematic error in H_2O at 22 hPa and 46 hPa.

The following sources of systematic error were also considered but the resulting uncertainties in mixing ratio are generally not as significant as those which arise from the above-mentioned sources. The estimated systematic errors in mixing ratio arising from the sources below are not plotted in figure 3.15 but have been included in the estimate of the root-sum-square systematic error.

spectroscopy: errors in spectroscopic parameters can give rise to errors in retrieved mixing ratio. Line positions are known extremely accurately at microwave wavelengths and therefore do not represent a significant error source. Uncertainties in line strength have been included in the radiance scaling uncertainty mentioned above. Possible errors in linewidth were treated by assuming an uncertainty of 1.8 % in the broadening function and an uncertainty of 4 % in the temperature exponent. These uncertainties were estimated by combining information from *Bauer et al., [1989]* and *Goyette and De Lucia, [1990].*

We also include a related uncertainty from imperfect knowledge of the Doppler shift of the emitted radiation, produced by line of sight velocity effects. Atmospheric wind along the line of sight will be the dominant source of error since both the spacecraft and earth velocity components are reasonably well known. An uncertainty of 70 m/s in line of sight velocity was assumed. The root-sum-square uncertainty in H_2O mixing ratio due to these three error sources is generally less than 0.1 ppmv in the stratosphere and 0.2–0.25 ppmv in the mesosphere, where uncertainty in the line of sight velocity becomes significant through the Doppler effect.

dry air continuum: the dry air continuum is a semi-empirical contribution which is derived from radiance data from the 205 GHz radiometer [see *Read et al., paper in preparation*]. Possible errors produced by imperfect knowledge of the dry air continuum are estimated by assuming that no dry air continuum is present in the forward model, and comparing the subsequent retrieved H_2O mixing ratios with a standard retrieval. This is a 'worst case' scenario. This error source is only significant in the lower stratosphere where an error of 0.07 ppmv occurs at 46 hPa and an error of 0.03 ppmv occurs at 22 hPa.

FOV shape and position: FOV shape and position errors of the 183 GHz radiometer have been transformed into errors in radiance [see *Jarnot et al., 1994*]. This gives an error of 0.5 K, at most, in brightness temperature and this value was used to construct a covariance matrix of radiance error due to this source assuming these errors to be fully correlated across the band. The resulting error in H_2O mixing ratio is significant only in the lower stratosphere and is generally less than 0.1 ppmv.

filter shape: each frequency channel across the H_2O band of the 183 GHz radiometer has an associated filter shape and position. Filter position errors are negligible but errors in filter shape could give rise to worst case errors in calibrated radiance of $\sim$ 0.5% [see *Jarnot, et al., 1994*]. A covariance matrix of radiance error due to this source was constructed with no correlations between channels. The resulting uncertainty in H_2O mixing ratio is small

when compared to the other systematic uncertainties mentioned above and is generally less than 0.03 ppmv.

In summary, the root-sum-square (rss) estimated systematic error in retrieved H_2O is 0.4–0.85 ppmv (7–18 %) between 46 hPa and 0.2 hPa. At 0.1 hPa, the rss systematic error is 2.2 ppmv (30 %) and between 0.046 hPa and 0.01 hPa the rss systematic error is $\sim$ 0.9 ppmv (30 % at 0.046 hPa increasing to 60 % at 0.01 hPa).

3.4.3 Summary of Error Analysis

In this section a summary of the above error analysis is presented. Figure 3.16 shows the rss random error (from figure 3.10), the rss systematic error (from figure 3.15), the smoothing error (from figure 3.13) and the root-sum-square of these three errors. Also plotted for comparison are typical estimates, produced by the MLS Version 3 production retrieval algorithms, of errors in retrieved H_2O mixing ratios. Figure 3.17 shows the same information but expressed as a percentage of a typical mid-latitude H_2O profile as retrieved by MLS.

It can be seen that between 4.6 hPa and 0.046 hPa, the total rss error is dominated by the systematic errors and below 46 hPa the smoothing error is dominant. At 4.6 hPa and above, the MLS Version 3 error generally lies somewhere between the rss random error and the total rss error. This is to be expected as the MLS Version 3 error contains components from random errors and from the smoothing error, but on the whole does not take account of systematic uncertainties. The MLS Version 3 error does contain a systematic component which is designed to account for known differences between the tabulated linear forward model and the complete radiative transfer model (see Chapter 2). This amounts to adding 3 % of the measured radiance in band 5 to the radiance noise prior to performing the retrieval of H_2O. It is this factor which may account for the MLS Version 3 error being larger than the total rss error from the above analysis at 10 hPa and 22 hPa. At 100 hPa both the error analysis and the MLS Version 3 errors give an error of 2 ppmv which is the *a priori* error.

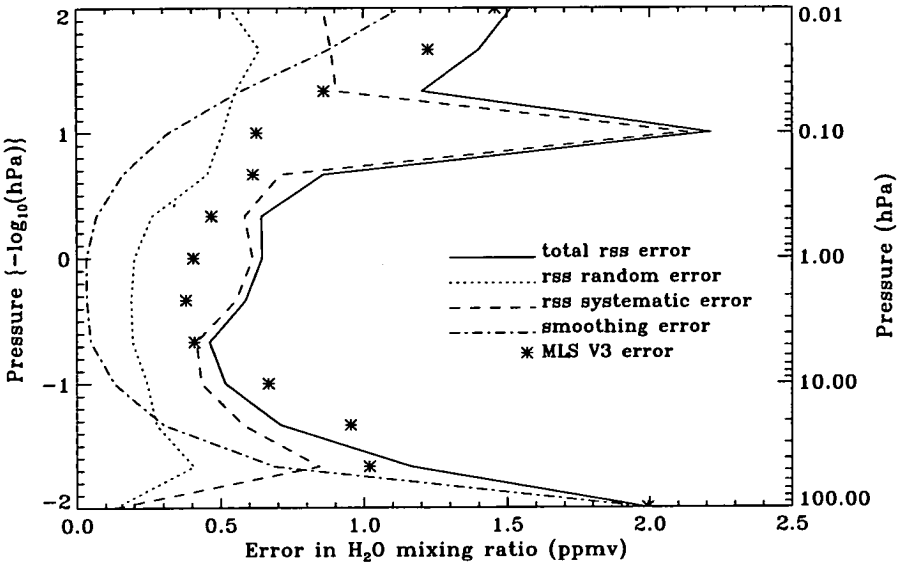

Figure 3.16: Errors for H_2O retrieval

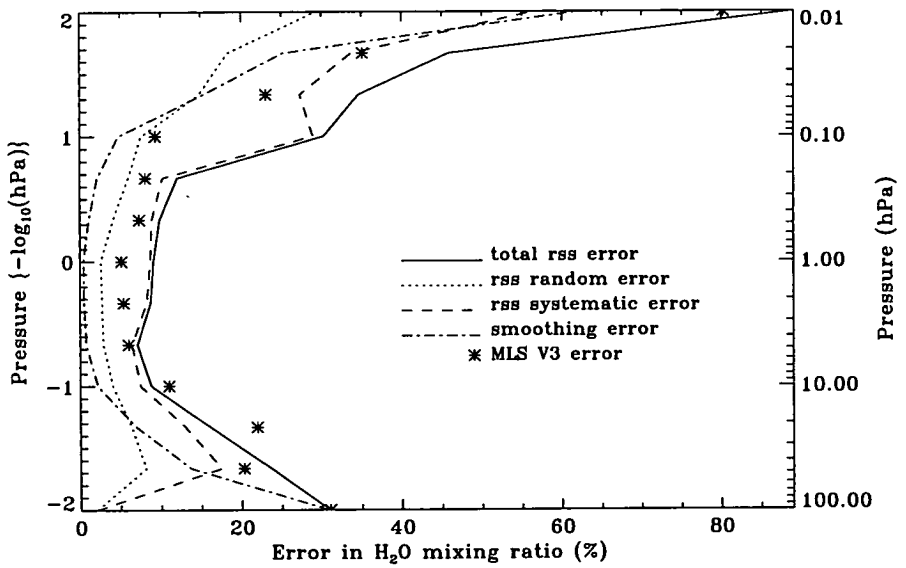

Figure 3.17: Percentage errors for H_2O retrieval

Finally, Table 3.1 gives estimates of the precision and overall accuracy of the MLS Version 3 H_2O retrievals based on the error analysis described above. The estimated precision is taken as the rss random error and the overall

Pressure	Single Profile Precision		Accuracy	
(hPa)	(ppmv)	(percent)	(ppmv)	(percent)
0.01	0.55	29	1.5	89
0.022	0.65	18	1.4	46
0.046	0.55	15	1.2	35
0.1	0.5	8	2.2	30
0.22	0.45	6	0.85	12
0.46	0.25	4	0.65	10
1	0.2	3	0.65	9
2.2	0.2	3	0.6	9
4.6	0.2	3	0.45	7
10	0.25	4	0.5	9
22	0.3	6	0.7	16
46	0.4	8	1.15	24

Table 3.1: Estimated precision and accuracy for MLS Version 3 H_2O retrievals

accuracy is the root-sum-square of the rss random error, the rss systematic error and the smoothing error. The precision estimates apply to a single profile; any averaging of profiles will improve the precision. The estimates have been rounded to the nearest 0.05 ppmv and to the nearest whole number for percentage values. Table 3.1 shows precision and accuracy estimates for the vertical range 46 hPa to 0.01 hPa. Note that between 46 hPa and 4.6 hPa, the precision estimate given here may be overly pessimistic as the measured variability of the MLS H_2O retrievals appears to be significantly smaller than the rss random error (see figure 3.12) in this region. Also, differences between MLS Version 3 H_2O and other measurements of H_2O [see *Lahoz et al., 1994*] generally lie within the overall accuracy quoted in Table 3.1, although between 1 hPa and 0.22 hPa, there is some evidence to suggest that some systematic effects may not be accounted for adequately. The comparisons with other measurements also suggest that the MLS Version 3 H_2O values are consistently too large by $\sim 5\,\%$ at 46 hPa and at 22 hPa and by 15–20 % in the range 1 hPa

to 0.22 hPa.

3.5 Chapter Summary

In this chapter a characterisation and error analysis of UARS MLS 183 GHz H_2O retrievals was presented. Firstly, examples of modelled radiances in the frequency range 182–187 GHz were shown along with some typical radiances measured by band 5 of the MLS 183 GHz radiometer. Examples of influence functions were then presented, which showed that the band 5 radiances were sensitive to perturbations in H_2O mixing ratio from the lower stratosphere into the lower thermosphere. The contribution functions and averaging kernels then gave information on the sensitivity of the H_2O retrieval. A study of the averaging kernels suggested that the useful vertical range of the Version 3 H_2O retrievals is 46–0.01 hPa. However, due to known artefacts in the data, a restricted vertical range for useful scientific studies with Version 3 H_2O retrievals is given as 22–0.2 hPa at high latitudes and 46–0.2 hPa elsewhere. For this useful vertical range, the estimated vertical resolution of the retrievals is 5–6 km. An error analysis was performed which produced estimates of the contributions of both random errors, including the smoothing error, and systematic uncertainties to the overall error in retrieved H_2O. From this analysis, a summary of the estimated precision and overall accuracy of the MLS Version 3 H_2O retrievals was presented in Table 3.1.

The retrieval of H_2O, using MLS Version 3 algorithms, employs a linear retrieval method. Research is currently underway at Edinburgh University to perform a nonlinear retrieval of H_2O from the measured radiances of band 5 of the 183 GHz radiometer. Studies have also been performed at JPL to retrieve H_2O in the upper troposphere and lower stratosphere using the measured radiances from the 205 GHz radiometer [*Read et al., 1994*].

In Chapter 4, an investigation of the apparent loss of measurement information in the H_2O retrievals in the lower stratosphere at high latitudes during winter, is presented along with a proposed method to improve such retrievals.

In Chapter 5, the effect on the retrieval of including non-zero off-diagonal elements in the *a priori* covariance matrix, is discussed, and the possibility of retrieving H_2O to a finer vertical resolution is investigated.

Chapter 4

Possible improvements to H_2O retrievals in the lower stratosphere

4.1 Introduction

In this chapter a problem with the retrieval of H_2O in the lower stratosphere at high latitudes during winter is investigated. Firstly, the nature of the problem is illustrated and an explanation of the source of the problem is given. Then, a proposed method of improving the H_2O retrievals in this region is discussed and the results of test retrievals are presented.

Before illustrating the problem, a reminder of the error ratio, which is described in Chapter 2, is given. The error ratio, for a particular retrieval level, is defined as the ratio of the corresponding diagonal element of the error covariance matrix after retrieval to that before retrieval and provides a measure of the relative contributions to the retrieval from the measurements and from the *a priori* information. If the error ratio is equal to 1 then no information has been provided by the measurements, if the ratio is close to 0 then most of the information has come from the measurements and little is contributed by the *a priori* information. The error ratio is used to qualify

the retrieved values in the MLS data files. When the error ratio is greater than 0.5, which means that more than 25% of the variance of the retrieval is due to the *a priori* information, the estimated uncertainties are flagged with a negative sign. This alerts the user that poorer measurement sensitivity is expected and the use of these data values is cautioned against.

In figure 4.1 the zonal mean error ratio for the MLS Version 3 retrieval of H_2O is plotted for three different days; 10th January 1992 (top panel), 8th August 1992 (middle panel), and 30th August 1992 (bottom panel). Each panel shows a contour plot of the error ratio with contour intervals of 0.1. The horizontal axis represents latitude in degrees and the vertical axis represents the pressure of the retrieval level in hPa. For both 10th January and 8th August 1992, MLS was north-looking and on 30th August 1992 MLS was south-looking. It can be seen that, for the three days shown, the error ratio for H_2O is generally less than 0.5 at retrieval levels above 22 hPa, and there is no strong variation with latitude. This is typical of the H_2O retrieval on most days. However, it is noticed that below 22 hPa, on both 10th January and 30th August 1992, there is an increase in error ratio towards the higher latitudes. This reflects an increase in the contribution from the *a priori* information and a decrease in the amount of information provided by the measurements. On 10th January 1992 the increase in error ratio occurs at high northern latitudes, and on 30th August 1992 the increase occurs at high southern latitudes. It is noted that on 8th August 1992 there is no increase in the error ratio at high latitudes. Thus, it appears that the increase in error ratio in the lower stratosphere occurs at high latitudes only in the winter hemisphere. Further inspection of the H_2O retrievals on other days reveals a similar increase in the error ratio towards the high latitudes in the winter hemisphere.

Figure 4.2 shows equal-area projections of MLS retrieved temperature (top panel) and error ratio for H_2O (bottom panel) at 46 hPa on 10th January 1992 (UARS day 121). The edge of the plots are at 33°S and the black circle in the centre shows the area where no MLS measurements are made. Only data from the ascending sections of orbits are plotted. On this pressure surface the MLS

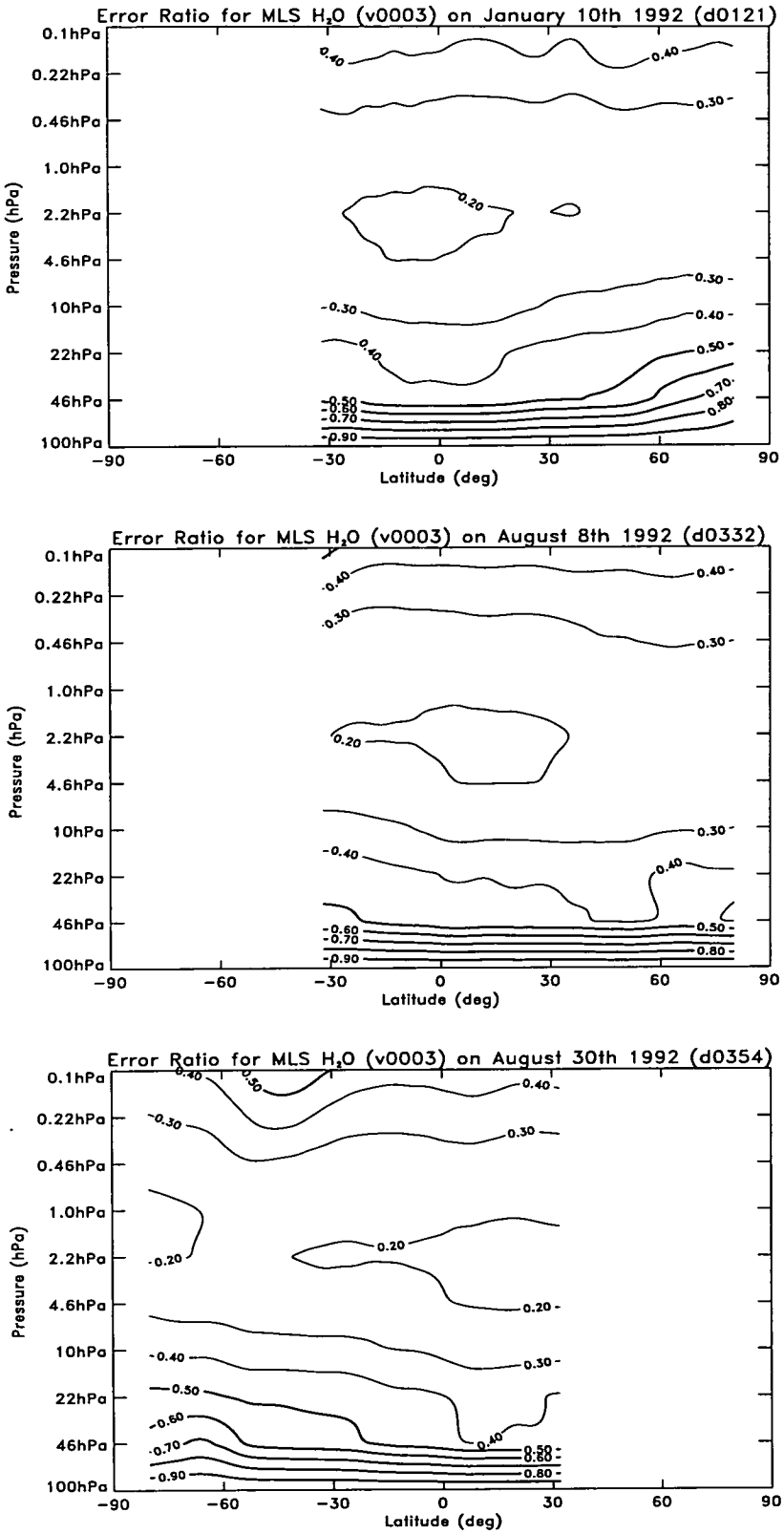

Figure 4.1: Zonal mean error ratio for H_2O on 10th January 1992, 8th August 1992 and 30th August 1992

band 1 radiances do not contribute to the retrieval of temperature and so the retrieved temperatures are set equal to the *a priori* values which are derived from the daily analysis of the U.S. National Meteorological Centre (NMC) [*see Fishbein et al., 1994*]. However, this should give a good representation of the temperature distribution at 46 hPa. In the top panel the cold Arctic vortex can be seen centred just to the right of the pole. In the bottom panel, it can be seen that it is in this same region that the highest error ratios occur. Near to the centre of the vortex, error ratios greater than 0.9 are found and a substantial area is covered by error ratios greater than 0.5.

Figure 4.3 shows similar plots as figure 4.2 but at 22 hPa. At this pressure surface the MLS retrieved temperatures do contain information from the measured radiances and the contribution from the *a priori* temperature is small. In the top panel, as before, the cold Arctic vortex is evident and is located to the right of the pole. From the bottom panel, it can be seen that the error ratio is less than that at 46 hPa, but a substantial area exists, in the region of the cold vortex, where the error ratio lies between 0.5 and 0.6.

The plots in figures 4.2 and 4.3 only show data from the ascending sections of orbits, but similar features are found when plotting data from the descending sections. Inspection of retrievals on other days also shows that the occurrence of high error ratios at 46 hPa and 22 hPa coincides with the presence of cold air in the region of the polar vortex.

From the above discussion it appears that, at high latitudes in the winter hemisphere, the retrieval of H_2O at 46 hPa and at 22 hPa contains a larger contribution from the *a priori* information than the retrievals at lower latitudes or at high latitudes in the summer hemisphere. To illustrate this further, the averaging kernels and the smoothing error for the retrieval of H_2O at high latitude during winter are presented. The calculations were performed for a profile at 70°S on 12th July 1992. On this day, during the southern hemisphere winter, MLS was south-looking and the selected profile is located within the cold Antarctic vortex.

Figure 4.4 shows the resulting averaging kernels which are to be compared

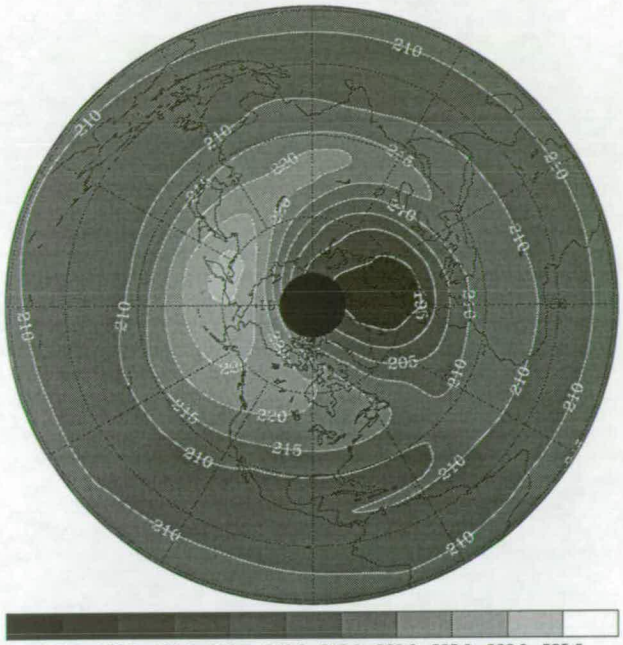

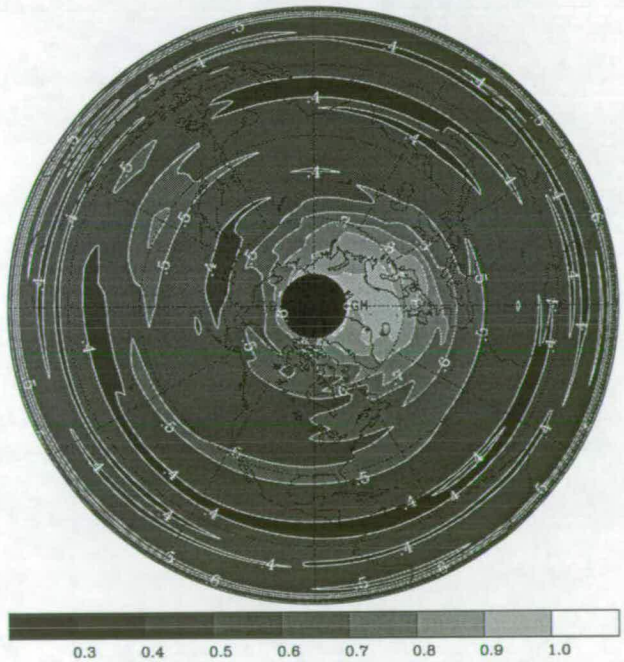

Figure 4.2: Temperature and Error ratio for H_2O at 46 hPa on 10th January 1992

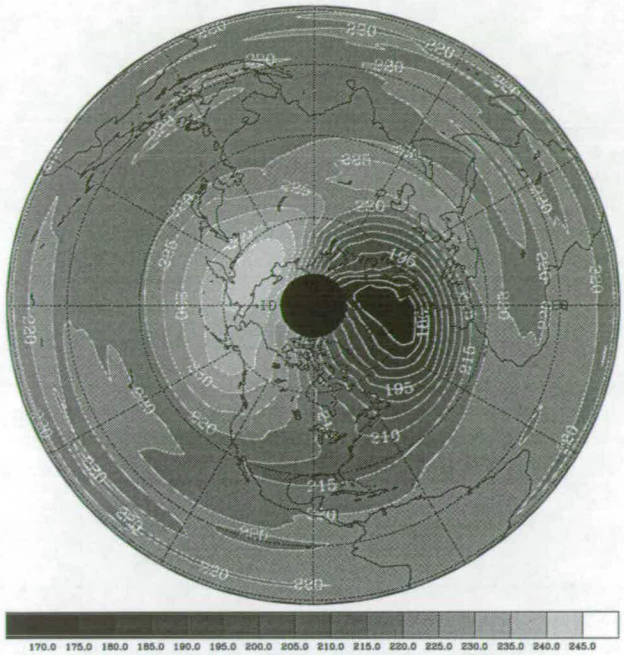

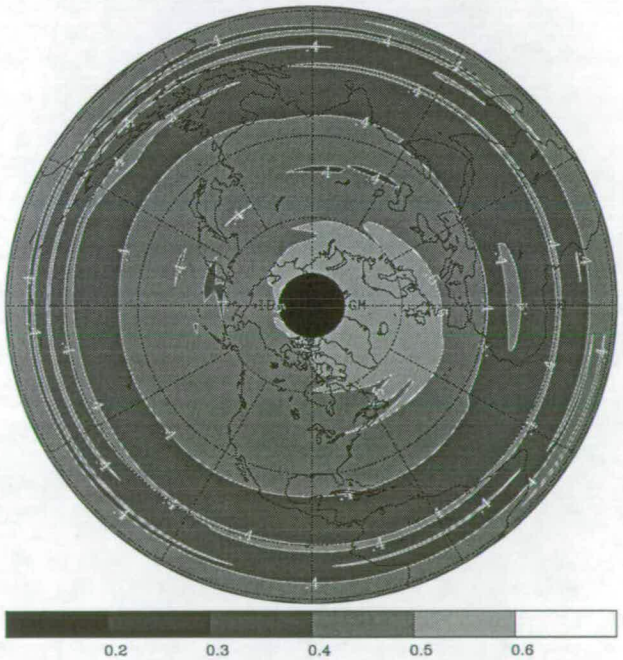

Figure 4.3: Temperature and Error ratio for H_2O at 22 hPa on 10th January 1992

with those of a typical mid-latitude retrieval shown in figure 3.6. The major

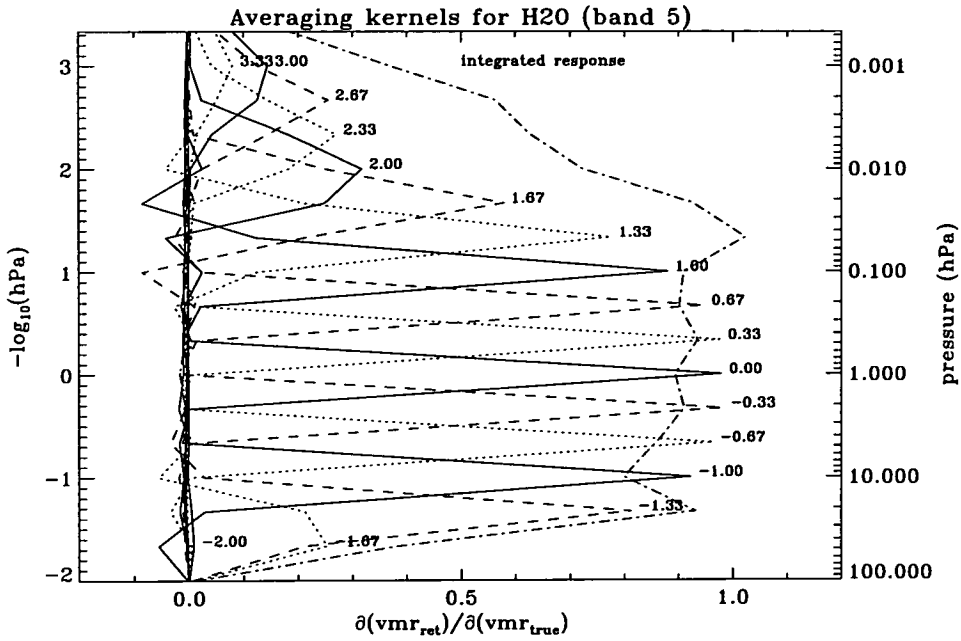

Figure 4.4: Averaging kernels for H_2O retrieval at high latitude during winter

difference between the two sets of averaging kernels occurs for the retrieval at 46 hPa; the peak value is only 0.25 for the high latitude retrieval compared with a peak value of nearly 0.8 for the typical mid-latitude retrieval. This reflects a substantial reduction in measurement information for the retrieval at 46 hPa and implies a corresponding increase in the contribution from the *a priori* information. A small reduction in the peak value of the averaging kernel at 22 hPa is also found; 0.8 for the high latitude retrieval compared to 0.9 for the typical mid-latitude case. It also appears that the integrated response for the high latitude retrieval is, in general, less than that for the typical mid-latitude retrieval, which reflects a reduced sensitivity of the whole retrieved profile to perturbations in the H_2O mixing ratio.

The estimated smoothing error for both the polar winter and the typical mid-latitude retrievals is plotted in figure 4.5. It can be seen that, in general, the smoothing error for the retrieval during the polar winter is greater than that for the typical mid-latitude retrieval. This increase in smoothing error

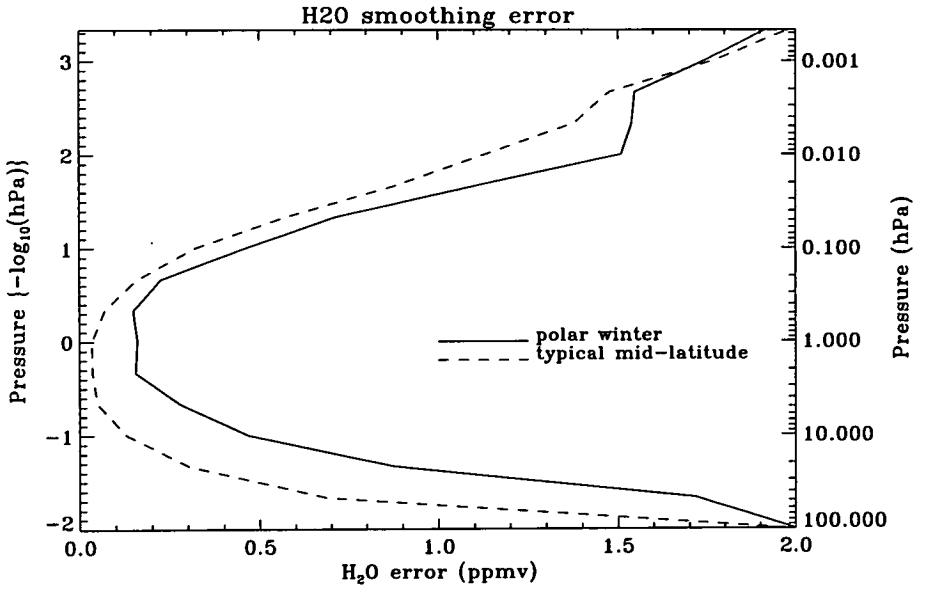

Figure 4.5: Smoothing error for H_2O retrieval during polar winter and for typical mid-latitude

is particularly significant in the lower stratosphere; at 46 hPa the smoothing error has increased from 0.7 ppmv to 1.7 ppmv, and at 22 hPa the increase is from 0.3 ppmv to 0.9 ppmv. Since the smoothing error is a measure of the contribution of the *a priori* error to the retrieval error, then this provides further evidence that the retrieval of H_2O at high latitudes during winter is subject to a significant loss of measurement information in the lower stratosphere.

The observation of H_2O mixing ratios in the lower stratosphere over the polar regions during winter and spring time is important in the study of stratospheric chemistry in the polar vortex [*Turco et al., 1989*]. Previous aircraft-borne measurements by *Kelly et al., [1989]* and *Gandrud et al., [1990]* lead to evidence of dehydration of the Antarctic and Arctic polar stratosphere, respectively. However, measurements from aircraft have limited spatial coverage but satellite-borne instruments, such as MLS, can provide measurements on a near global scale. Thus, it is desirable to try to improve the quality of the retrieval of H_2O from MLS in the lower stratosphere during the polar winter.

4.2 Proposed method to improve retrievals in the lower stratosphere

4.2.1 Cause of loss of measurement information

In this section an explanation of the cause of the above-mentioned loss of measurement information for the retrieval of H_2O in the polar lower stratospheric winter is given. The low temperatures which exist in these regions result in the pressure surfaces sinking to lower heights than those at mid-latitudes. The tangent points of the MLS limb views occur at approximately the same heights for each scan, allowing for perturbations in satellite attitude, but the corresponding pressure of the tangent points varies depending on the temperature of the atmosphere. Thus, in the cold polar vortex the MLS radiance measurements have an associated tangent pressure which is lower than that of corresponding measurements at mid-latitudes.

The opacity criterion (see Chapter 2) determines whether or not a radiance measurement is included in the retrieval; if the estimated optical thickness of the limb view is less than a prescribed maximum permitted value then the radiance measurement is used. The effect of the opacity criterion is displayed in figure 4.6 for limb scans at both mid-latitudes and during polar winter. The plots in figure 4.6 show the radiance measurements which are included in the retrieval (denoted by an asterisk) and those which are rejected (denoted by a dot) on the basis of the opacity criterion. The left panel corresponds to a typical limb scan at mid-latitude and the right panel corresponds to a limb scan at high latitude during winter. The vertical axis gives the tangent pressure associated with each limb view and the horizontal axis represents the channel number. Remember, channel 8 is positioned at the centre of the 183.3 GHz H_2O line, and channels 1 and 15 are the channels positioned furthest from the line centre (see Table 1.2).

In both panels of figure 4.6 it can be seen that, for limb views above 0.1 hPa, measurements in all channels are included in the retrieval. As the in-

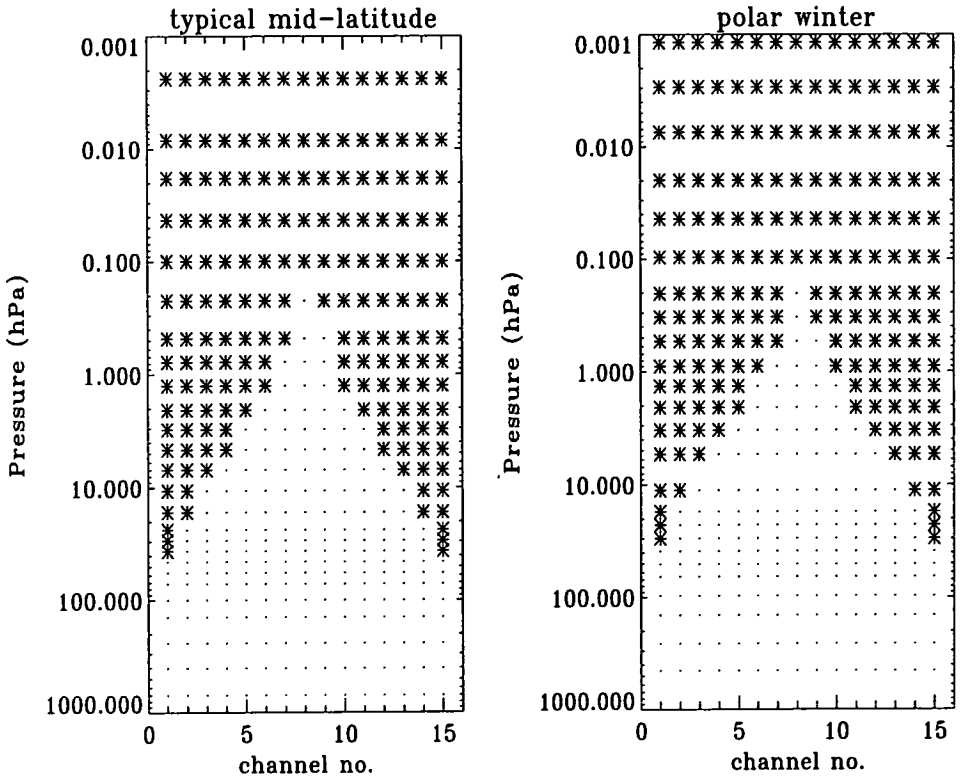

Figure 4.6: Effect of opacity criterion. Left panel for typical limb scan at mid-latitude, right panel for limb scan at high latitude in winter. The plots show the radiance measurements which are included in the retrieval (*) and those which are not (.)

strument scans downward below 0.1 hPa, measurements begin to be rejected; firstly from the centre channel and then from channels further from line centre. By the time the tangent pressure of the limb view is at 10 hPa, only the measurements in channels 1, 2, 14 and 15 are included in the retrieval. An important difference between the plots in the two panels is that the measurements in channels 1 and 15 are used down to tangent pressures of ~ 40 hPa for the typical mid-latitude case whereas, for the scan at high latitude in winter, the measurements in channels 1 and 15 are not used below ~ 30 hPa. Although these measurements in channels 1 and 15 are rejected below approximately the same height (~ 22 km) in both cases, the low stratospheric temperatures over the polar region in winter cause this threshold to occur at a lower tangent pressure than for the measurements at mid-latitudes.

Thus, for the retrieval of H_2O at high latitudes in winter, there are gen-

erally no measurements available below ~ 30 hPa and so the retrieval at the 46 hPa level is dominated by the *a priori* information. As mentioned above, the retrieval at the 22 hPa level would also appear to suffer from a small loss of measurement information.

4.2.2 Development of channel-dependent opacity criterion

From the discussion in the previous section, it would appear desirable to try and reduce the threshold height below which the radiance measurements are ignored during the retrieval process. This should increase the contribution from the measurements to the retrieval at 46 hPa. In order to do this, the opacity criterion must be amended.

From equation (2.19) of Chapter 2, the estimated optical thickness of a limb path for a particular channel is given by

$$\tau_{p_i} = -ln[1 - y_i/(\omega_{p_i} T_{tan})] \tag{4.1}$$

where y_i is the measured radiance (in brightness temperature units) in the ith channel, ω_{p_i} is the proportion of the measured brightness temperature which comes from the principal sideband of the ith channel, T_{tan} is the temperature at the tangent point and τ_{p_i} is the estimated optical thickness in the ith channel. For the MLS Version 3 retrieval, this estimated optical thickness, τ_{p_i}, is compared with the prescribed critical value, τ_c; if $\tau_{p_i} > \tau_c$ then the corresponding radiance measurement y_i is ignored during the retrieval. For the MLS Version 3 retrieval, $\tau_c = 1$. One method of reducing the height below which the measurements are ignored would be to increase the value of τ_c. However, τ_c is not channel-dependent and any increase in its value may have an undesirable effect on the retrieved profile at levels above the lower stratosphere by allowing radiance measurements from optically thick limb paths in the channels near to the line centre to be included in the retrieval.

It would seem desirable to develop a channel-dependent τ_c in order to investigate the possibility of allowing the threshold height, at which the mea-

sured radiances in the wing channels (channels 1, 2, 14 and 15) are rejected, to be reduced without affecting the rejection criterion for the other channels. Also, equation (4.1) does not take into account the presence of a signal in the image sideband. This signal generally becomes significant, in all channels, when the tangent height of the limb view is below $\sim 20\,\mathrm{km}$ (see figure 3.2). The fact that the estimate for τ_{p_i} does not take into account any signal in the image sideband is not important for most channels as the signal in the principal sideband generally becomes optically thick at tangent heights well above 20 km. However, the signal in channels 1 and 15 is not deemed to be optically thick until the tangent height is below $\sim 22\,\mathrm{km}$, generally. This is close to the height at which the signal in the image sideband becomes significant, and it may be that this extra contribution to the measured radiance results in an overestimate of the optical thickness of the limb path; in equation (4.1) if y_i increases then τ_{p_i} also increases. If the estimate of τ_{p_i} was to take into account any contribution from the image sideband then it may be possible to reduce the threshold height at which the measured radiances in channels 1 and 15 are rejected on the basis of the opacity criterion. This could be crucial in increasing the contribution from the measurements to the retrieval of H_2O in the lower stratosphere, particularly at 46 hPa.

From the above discussion it would appear that channel-dependent opacity criteria are desirable and that allowance should be made for the presence of a signal in the image sideband. An alternative, and equivalent way of applying the opacity criterion is to define a τ_i such that

$$\tau_i = -ln[1 - y_i/T_{tan}] \tag{4.2}$$

where y_i and T_{tan} have the same definitions as above. Now this τ_i is related to τ_{p_i} by

$$\tau_i = -ln[1 - \omega_{p_i}(1 - exp(-\tau_{p_i}))] \tag{4.3}$$

which is obtained by combining equations (4.1) and (4.2) and eliminating y_i. From equation (4.3), a channel-dependent critical value, τ_{c_i} can be defined

and is related to the original channel-independent critical value for the optical thickness in the principal sideband by

$$\tau_{c_i} = -ln[1 - \omega_{p_i}(1 - exp(-\tau_c))] \tag{4.4}$$

Although τ_i in equation (4.2) has no direct physical meaning, for a particular limb view, τ_i can be evaluated for each channel and compared with a prescribed critical value τ_{c_i}. Table 4.1 shows values for τ_{c_i} which are equivalent to using the original channel-independent opacity criterion with a critical value of $\tau_c = 1$, i.e., equivalent to the opacity criterion applied to MLS Version 3 retrievals. These τ_{c_i} values have been calculated using equation (4.4) with $\tau_c = 1$.

Channel	ω_{p_i}	τ_{c_i}	Channel	ω_{p_i}	τ_{c_i}
1	0.523202	0.401563	9	0.533165	0.411017
2	0.528306	0.406395	10	0.533296	0.411142
3	0.531003	0.408958	11	0.533554	0.411388
4	0.532070	0.409974	12	0.534068	0.411879
5	0.532596	0.410475	13	0.535143	0.412905
6	0.532860	0.410727	14	0.536973	0.414655
7	0.532985	0.410846	15	0.539863	0.417424
8	0.533079	0.410935			

Table 4.1: Relative response, ω_{p_i}, of the principal sideband and values of τ_{c_i} for channel-dependent opacity criterion equivalent to using channel-independent opacity criterion as for MLS Version 3 retrievals

Thus, with the channel-dependent opacity criteria, the critical value for a particular channel can be changed without affecting the other channels. From equation (4.4) and given the values of ω_{p_i}, it can be seen that for $\tau_c = \infty$, $\tau_{c_i} \sim 0.75$. Thus, setting $\tau_{c_i} = 0.75$ would allow the use of radiance measurements from a completely opaque limb path; setting $\tau_{c_i} > 0.75$ allows radiances from the image sideband to be used.

The channel-dependent opacity criterion described above was incorporated into the MLS retrieval algorithms in order to run test retrievals to investigate the possibility of increasing the contribution from the measurements to the retrieval of H_2O in the lower stratosphere at high latitudes during winter. In

the next section, the results of such test retrievals are discussed.

4.3 Test retrievals

In this section the results of performing test retrievals using the channel-dependent opacity criterion, described above, are discussed. The test retrievals were performed using both simulated radiances and radiances measured by MLS. Test retrievals were performed using a variety of critical values for τ_{c_i}, but the following discussion will concentrate on three different scenarios to illustrate the findings of this study.

These three scenarios are; (a) all critical values, τ_{c_i}, are such that the opacity criterion is exactly equivalent to that for the MLS Version 3 retrievals, i.e., the values for τ_{c_i} are set to those in Table 4.1, (b) $\tau_{c_1} = \tau_{c_{15}} = 1$, $\tau_{c_2} = \tau_{c_{14}} = 0.65$, the values of τ_{c_i} for channels 3 to 13 are as shown in Table 4.1, (c) $\tau_{c_1} = \tau_{c_2} = \tau_{c_{14}} = \tau_{c_{15}} = 0.6$, all other values of τ_{c_i} are as shown in Table 4.1.

Scenario (a) is equivalent to the MLS Version 3 retrieval. Scenario (b) allows radiances in channels 1 and 15 to be used which may arise from very opaque limb paths. Since the retrieval algorithm is linear (see Chapter 2), retrievals performed under this scenario may be subject to nonlinearities. Scenario (b) also allows for the presence of a signal in the image sideband, and allows the use of radiances in channels 2 and 14 which would arise from limb paths of greater optical thickness than that permitted by the MLS Version 3 retrieval. Scenario (c) is somewhat of a compromise between scenario (a) and scenario (b).

4.3.1 With simulated radiances

Radiances in band 5 of MLS were simulated using the MLS forward model and random noise equivalent to the typical noise on MLS measured radiances was added to these simulated radiances. The assumed temperature and H_2O distributions on which the radiance calculations are based, are smoothed versions of the MLS Version 3 retrievals for 17th September 1992 (UARS day 372)

when MLS was south-looking. To illustrate the results of the test retrievals the discussion will concentrate on a section of one particular orbit which crosses over the southern polar region. Figure 4.7 shows cross-sections of the assumed distributions of temperature and H_2O for the chosen orbit track. In each of the panels in figure 4.7 the latitude of every third profile is printed along the top of the plot and the corresponding longitude is printed along the bottom. The orbit track is also plotted at the bottom right of each panel. The top panel shows the assumed temperature distribution which contains temperatures of less than 200K at 46 hPa and 22 hPa over the polar region. The bottom panel displays the assumed H_2O distribution for the chosen orbit section and this distribution will be considered as the 'truth' against which the retrieved values will be compared.

In figure 4.8 the results of the H_2O retrievals along the chosen orbit track are plotted. The top panel shows the H_2O mixing ratios and in the bottom panel the corresponding error ratios are displayed. Along the horizontal axis the latitude of every fifth profile is marked. The results for the three retrieval scenarios described above are plotted; the dotted line corresponds to scenario (a), the dashed line corresponds to scenario (b) and the dash-dot line corresponds to scenario (c). In the top panel the solid line shows the H_2O mixing ratio which represents the assumed true value at 46 hPa. It can be seen that at low and mid-latitudes, the retrieved values for scenario (a), which is equivalent to the MLS Version 3 retrieval, do not differ greatly from the values retrieved under scenarios (b) and (c), and that on the whole, all of these retrieved values tend to be larger than the true value by 0.1–0.3 ppmv. However, at the high southern latitudes the scenario (a) retrieval tends to overestimate the true value by as much as 1 ppmv whereas the scenario (b) and (c) retrievals give estimates of H_2O that are close to the true value in this region. The error ratio for the scenario (a) retrieval at low and mid-latitudes tends to lie between 0.35 and 0.5, but increases to between 0.6 and 0.8 at high latitudes. In contrast, the error ratio for the scenario (b) and (c) retrievals lies between 0.3 and 0.4 throughout the orbit section. Thus, the retrievals for scenarios (b) and (c)

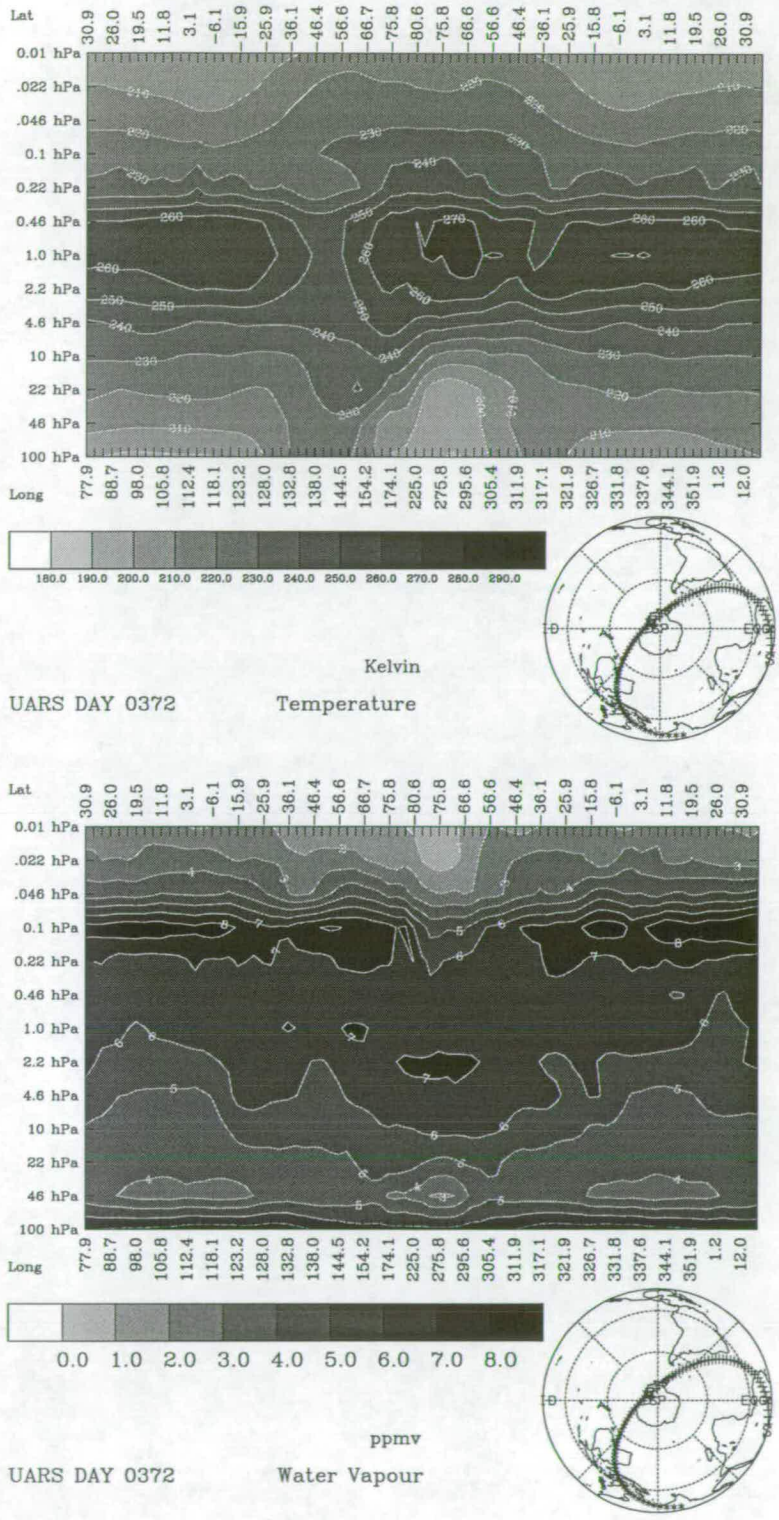

Figure 4.7: Temperature and H_2O cross-sections, along part of an orbit, of assumed distributions based on smoothed versions of the MLS Version 3 retrievals on 17th September 1992 (UARS day 372). See text for details.

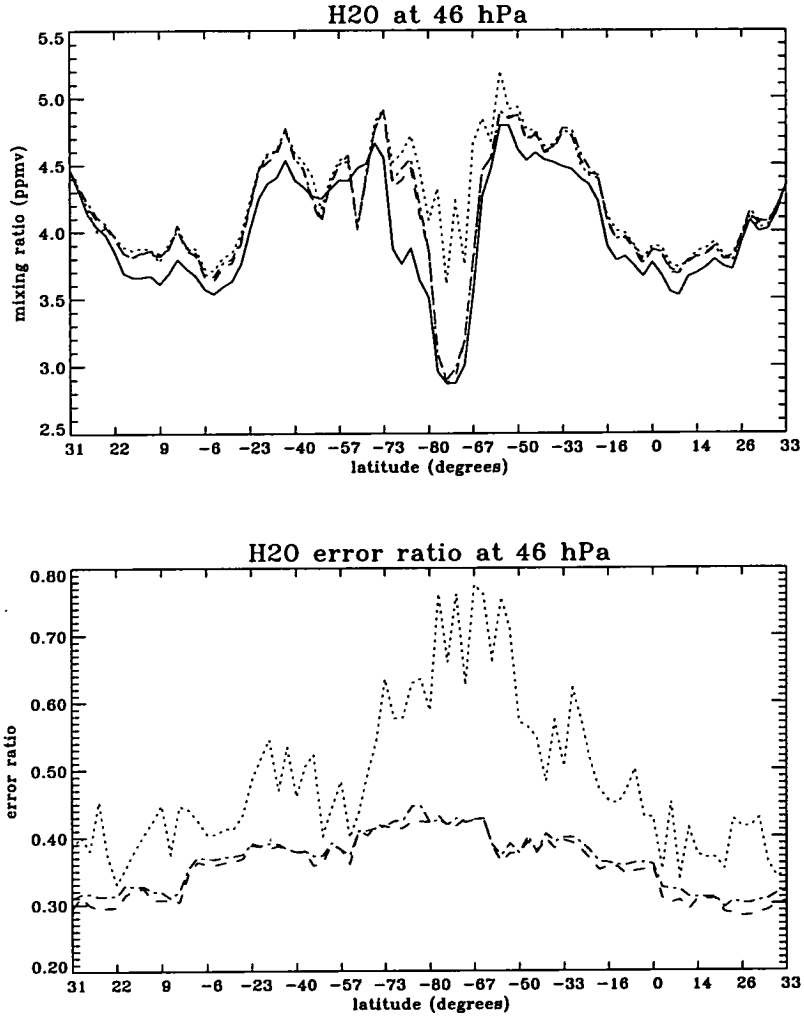

Figure 4.8: H_2O retrievals at 46 hPa based on simulated data. The plots are for a chosen orbit track which crosses over the southern polar region. Dotted line - scenario (a), dashed line - scenario (b), dash-dot line - scenario (c), solid line - true mixing ratio. See text for details.

are less influenced by the *a priori* information than the scenario (a) retrieval and hence contain more information from the measurements themselves. For the retrieval of H_2O at 46 hPa the difference between the scenario (b) and (c) retrievals is small.

Figure 4.9 shows similar plots to figure 4.8 but for the retrieval of H_2O at 22 hPa. In general, the scenario (a) retrieval tracks the true value just as well as the scenario (b) and (c) retrievals. However, the error ratio for scenarios (b) and (c) is less than that for scenario (a) reflecting an increase in the amount of information contributed by the measurements. Also, the error

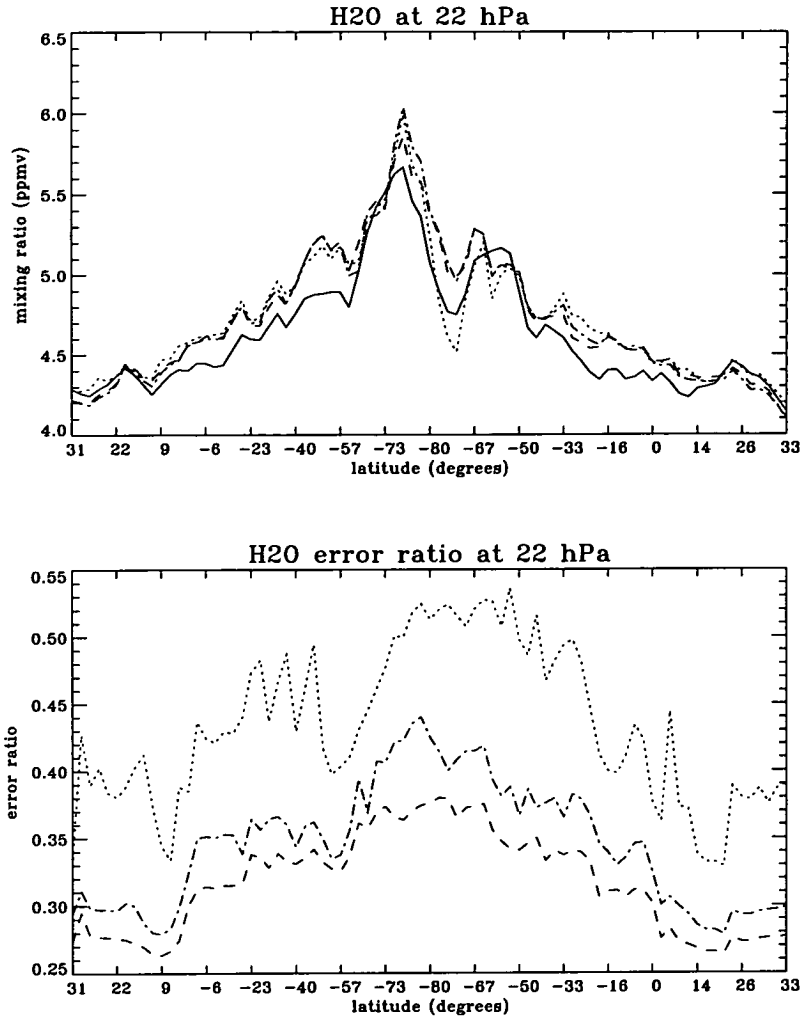

Figure 4.9: H_2O retrievals at 22 hPa based on simulated data. The plots are for a chosen orbit track which crosses over the southern polar region. Dotted line - scenario (a), dashed line - scenario (b), dash-dot line - scenario (c), solid line - true mixing ratio. See text for details.

ratio for scenario (b) is less than that for scenario (c). Further tests showed that this is due to the values of τ_{c_2} and $\tau_{c_{14}}$ being greater for scenario (b) than for scenario (c). At levels above 22 hPa there was no significant difference between the retrieved values and corresponding error ratios for the different scenarios.

Thus, from the results of performing retrievals based on simulated radiances, it appears that increasing the critical value of τ_{c_i}, for channels 1, 2, 14 and 15, from the values that are equivalent to performing the MLS Version 3 retrieval, improves the 'truth-tracking' ability of the retrieval at 46 hPa and

greatly reduces the error ratio, particularly at high latitudes. At 22 hPa the error ratio is also reduced and the 'truth-tracking' ability of the retrieval is no worse than for MLS Version 3. There is no great difference between the retrievals for scenarios (b) and (c) and so, on the basis of this study, scenario (c) would be recommended for implementation as the values of τ_{c_i} for channels 1, 2, 14 and 15 are less than those for scenario (b) and therefore scenario (c) would give a reduced risk to nonlinear effects.

4.3.2 With MLS measured radiances

In this section the results of test retrievals based on radiance measurements in MLS band 5 are discussed. The same three scenarios, described above, are used to illustrate the findings of this study.

The discussion will concentrate on retrievals based on measured radiances from 30th August 1992, when MLS was south-looking. As for the test retrievals based on simulated radiances, the analysis will concentrate on a section of a particular orbit that crosses over the southern polar region. Figure 4.10 shows cross sections of MLS Version 3 retrieved temperature and H_2O for the chosen orbit section. At the top of each panel the latitude of every third profile is printed and along the bottom of each panel the corresponding longitude is printed. It can be seen from the top panel that temperatures lower than 190K are to be found at 46 hPa and 22 hPa at high southern latitudes. The white dashed lines represent the 0.5 contour for the error ratio. Concentrating on the H_2O retrievals in the lower stratosphere, the error ratio at 46 hPa is generally less than 0.5 at low and mid-latitudes but increases to greater than 0.5 in the cold air associated with the southern polar vortex; this cold air extends to southern mid-latitudes. The error ratio for H_2O at 22 hPa is also generally less than 0.5 apart from in the cold polar region. Near to 80°S the MLS Version 3 retrieved mixing ratios for H_2O at 46 hPa are less than 2 ppmv which may suggest evidence of dehydration in this region. However, the error ratio in this region is greater than 0.5 and so the retrieval is deemed to be too strongly influenced by the *a priori* information for the purposes of scientific analysis.

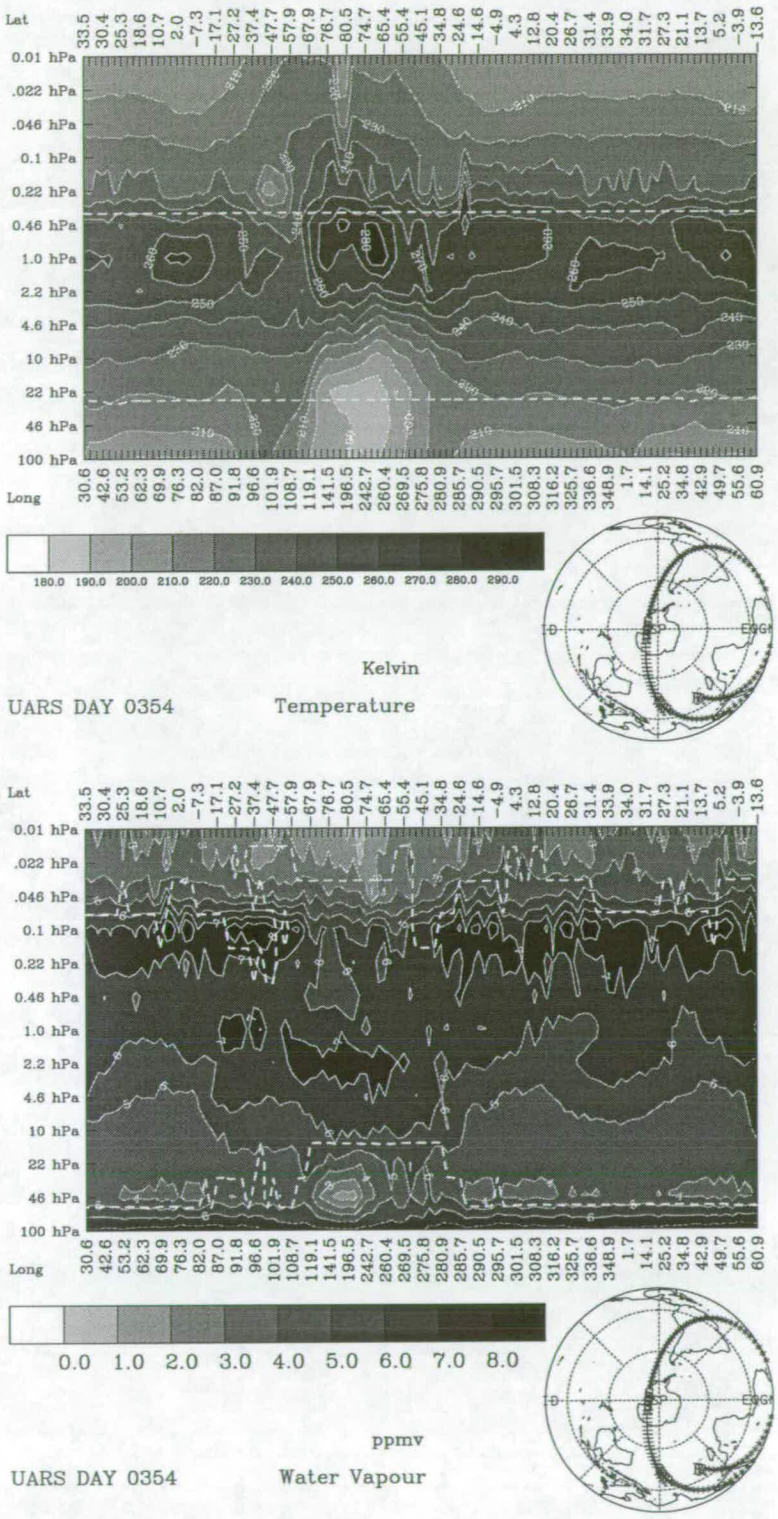

Figure 4.10: Temperature and H_2O cross-sections, along part of an orbit, for the MLS Version 3 retrieval on 30th August 1992 (UARS day 354). The white dashed lines represent the 0.5 contour for the error ratio. See text for details.

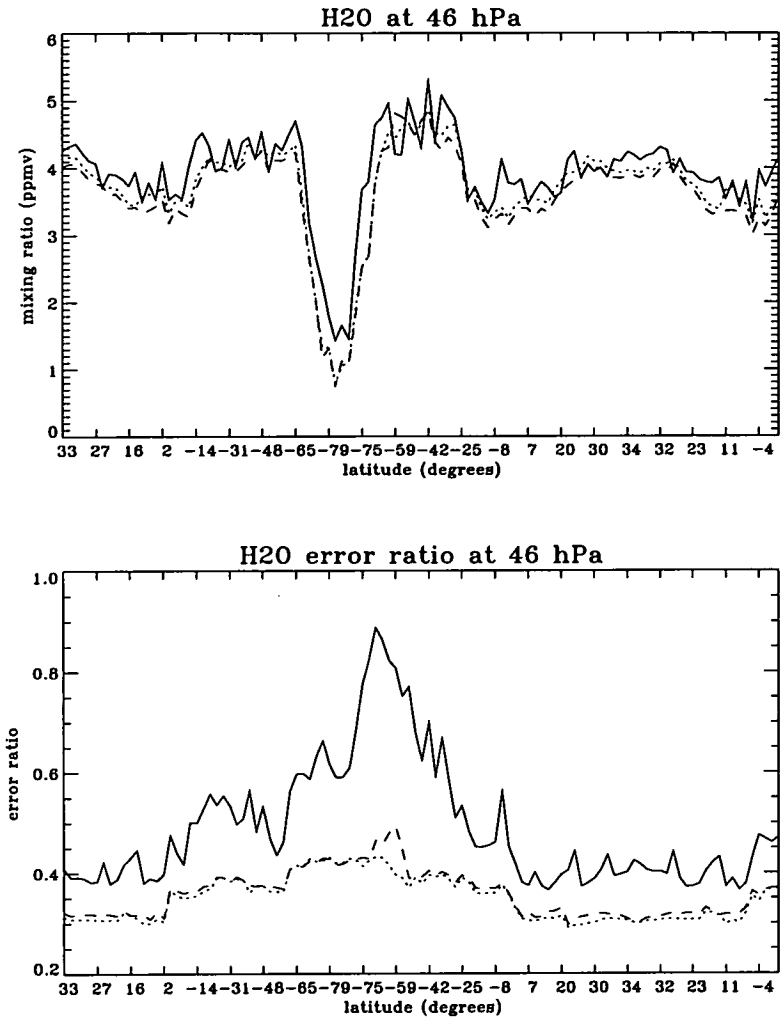

Figure 4.11: H_2O retrievals at 46 hPa based on measured radiances on 30th August 1992 (UARS day 354). The plots are for a chosen orbit track which crosses over the southern polar region. Solid line - scenario (a), dotted line - scenario (b), dashed line - scenario (c). See text for details.

Figure 4.11 shows the results, at 46 hPa, of the test retrievals for the three scenarios described above, along the chosen orbit section for 30th August 1992. The solid line corresponds to scenario (a), which is equivalent to the MLS Version 3 retrieval, the dotted line corresponds to scenario (b) and the dashed line corresponds to scenario (c). The top panel shows the retrieved mixing ratios and the bottom panel displays the corresponding error ratios. At low and mid-latitudes the retrieved mixing ratios for scenarios (b) and (c) appear to be slightly smaller than those for scenario (a), although it is not particularly clear. However, at high southern latitudes the retrievals for scenarios (b) and

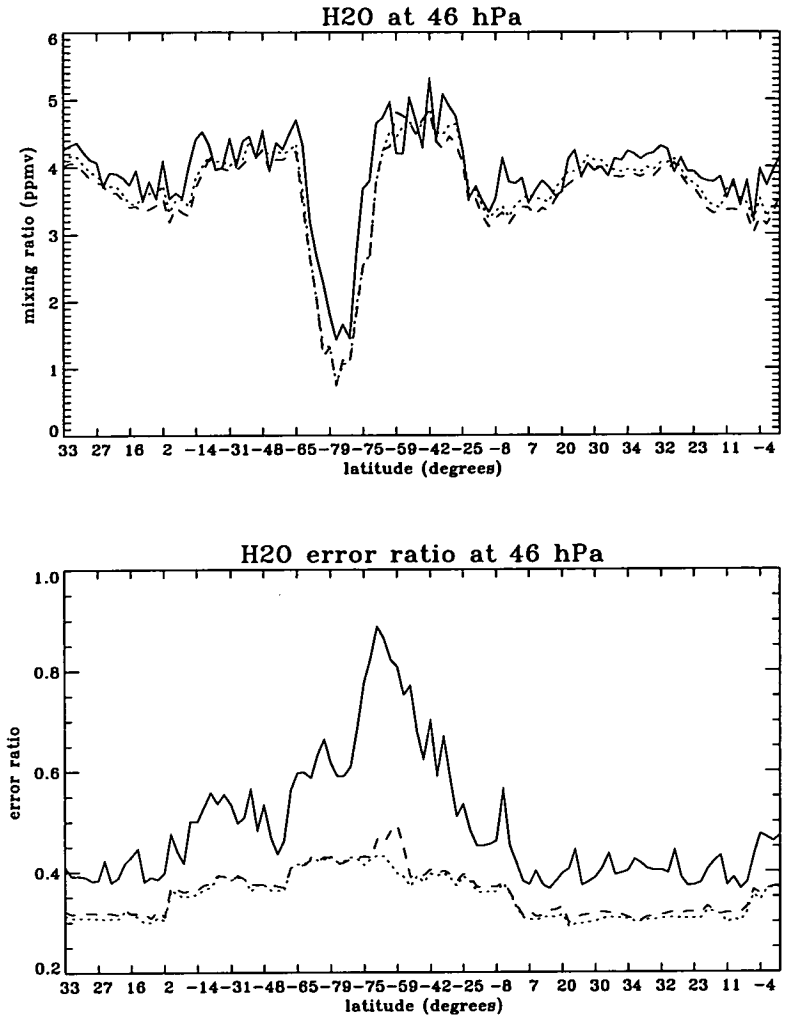

Figure 4.11: H_2O retrievals at 46 hPa based on measured radiances on 30th August 1992 (UARS day 354). The plots are for a chosen orbit track which crosses over the southern polar region. Solid line - scenario (a), dotted line - scenario (b), dashed line - scenario (c). See text for details.

Figure 4.11 shows the results, at 46 hPa, of the test retrievals for the three scenarios described above, along the chosen orbit section for 30th August 1992. The solid line corresponds to scenario (a), which is equivalent to the MLS Version 3 retrieval, the dotted line corresponds to scenario (b) and the dashed line corresponds to scenario (c). The top panel shows the retrieved mixing ratios and the bottom panel displays the corresponding error ratios. At low and mid-latitudes the retrieved mixing ratios for scenarios (b) and (c) appear to be slightly smaller than those for scenario (a), although it is not particularly clear. However, at high southern latitudes the retrievals for scenarios (b) and

(c) seem to give systematically lower mixing ratios than those for scenario (a). Unfortunately, in this case, as opposed to the study using simulated radiances, there is no 'true' value with which to compare the retrieved value. However, it can be seen that, for the retrieval scenarios (b) and (c), the error ratio at high southern latitudes is greatly reduced from that for scenario (a). In places, the error ratio has been reduced from greater than 0.8 to ~ 0.4. Thus, the retrievals for scenarios (b) and (c) contain a larger contribution from the measurements and a correspondingly smaller contribution from the *a priori* information than for scenario (a), and this should give more confidence in the retrieved mixing ratios produced using either scenario (b) or (c). There is not much difference between the retrievals for scenarios (b) and (c), as was the case when simulated radiances were used.

The results of the test retrievals at 22 hPa, along the chosen orbit section on 30th August 1992, are shown in figure 4.12. The lines plotted in both panels of figure 4.12 represent the same quantities as in figure 4.11 but correspond to the retrieval of H_2O at 22 hPa. From the bottom panel of figure 4.12 it can be seen that the error ratio for scenarios (b) and (c) is reduced from that obtained in scenario (a). This is a similar result to that found for the retrieval of H_2O at 22 hPa using simulated radiances. However, in the top panel it is noticed that the different retrieval scenarios give different mixing ratios at 22 hPa. Scenario (b) produces the highest mixing ratios, scenario (a) gives the lowest mixing ratios, and scenario (c) lies somewhere in between. The difference between the retrieved mixing ratios from scenarios (a) and (b) can be as much as 1 ppmv. These differences between the different retrievals at 22 hPa did not occur when simulated radiances were used.

Although the analysis so far has been concentrated on a particular orbit section, the retrievals were performed on the complete set of radiance measurements for 30th August 1992. In figure 4.13 the mean retrieved profiles are plotted within four selected latitude bands; 10°N–10°S, 10°–30°N/S, 30°–50°N/S, and 50°–80°S. The vertical extent of the plots is 100 hPa to 4.6 hPa. The horizontal bars represent the standard deviation, σ, of the scenario (a)

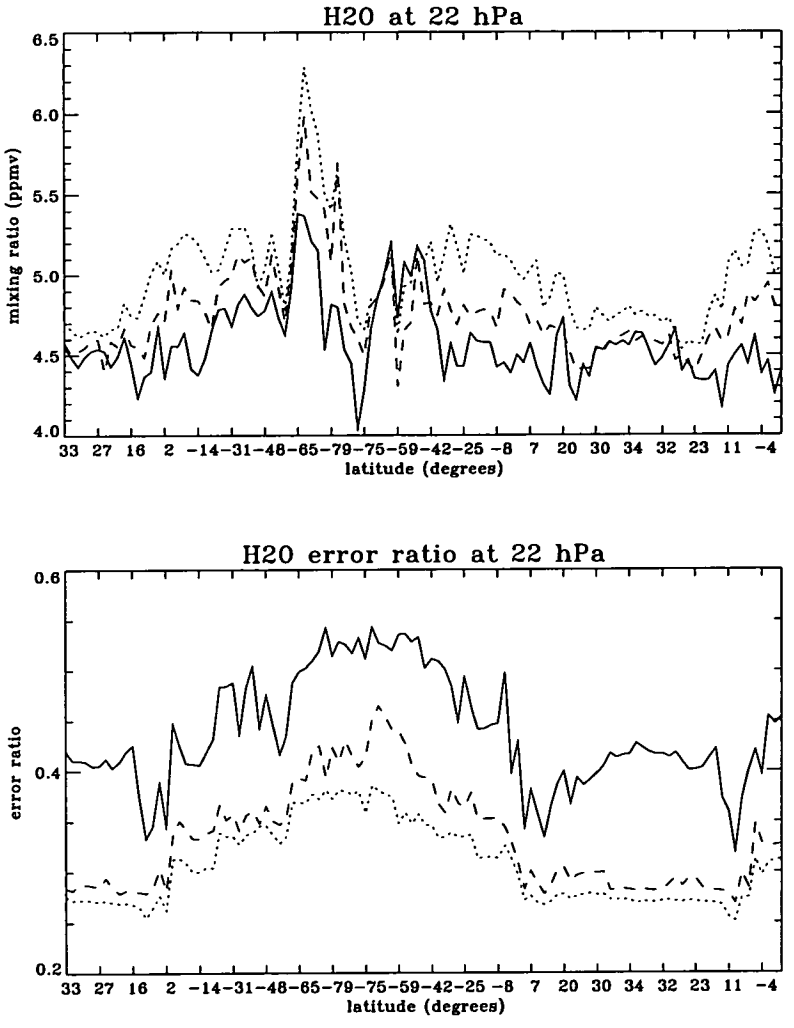

Figure 4.12: H_2O retrievals at 22 hPa based on measured radiances on 30th August 1992 (UARS day 354). The plots are for a chosen orbit track which crosses over the southern polar region. Solid line - scenario (a), dotted line - scenario (b), dashed line - scenario (c). See text for details.

retrievals; the bars are centred on the mean retrieved value for scenario (a) and have a length of 2σ. It can be seen that, under scenarios (b) and (c), the retrieved mixing ratios at 22 hPa are increased producing a less smooth profile than that produce by the scenario (a) retrieval. This is particularly apparent in the latitude range 10°N–10°S. This may be due to nonlinearities caused by including, in the retrieval, radiance measurements which arise from optically thick limb paths. It is also noted that, at 100 hPa, the retrieved values for scenarios (b) and (c) tend to be less than those for scenario (a). By increasing the τ_{c_i} values for channels 1, 2, 14 and 15, the retrieval at 100 hPa becomes sensi-

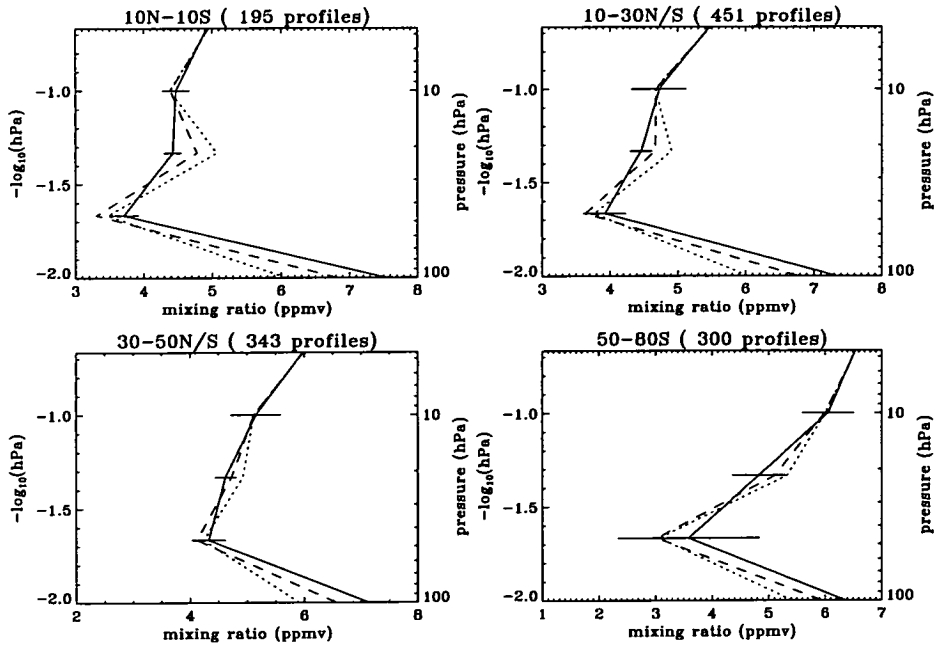

Figure 4.13: Mean retrieved profiles of H_2O within selected latitude bands for 30th August 1992. Solid line - scenario (a), dotted line - scenario (b), dashed line - scenario (c). See text for details.

tive to information in the radiances; the error ratio at 100 hPa (not shown) for scenario (a) is generally ~ 1, whereas the error ratio for scenario (b) is ~ 0.9 and that for scenario (c) is ~ 0.95. Thus, increasing the contribution from the measurements tends to decrease the retrieved mixing ratio at 100 hPa. It is possible that this change in mixing ratio at 100 hPa induces a subsequent change in the retrieved mixing ratio at 22 hPa.

Test retrievals were also performed on the complete set of radiance measurements from 10th January 1992, when MLS was north-looking. At 46 hPa, similar results to the retrievals on 30th August 1992 were found; the retrievals for scenarios (b) and (c) greatly reduced the error ratio compared to that of the scenario (a) retrieval. Also, at 22 hPa, the error ratio was reduced under scenarios (b) and (c). However, the increase in retrieved mixing ratio at 22 hPa, which was found for 30th August 1992 under scenarios (b) and (c), was present but not as significant for 10th January 1992. Figure 4.14 shows the mean retrieved profiles within selected latitude bands for 10th January 1992.

The format of figure 4.14 is similar to that of figure 4.13, but only shows the

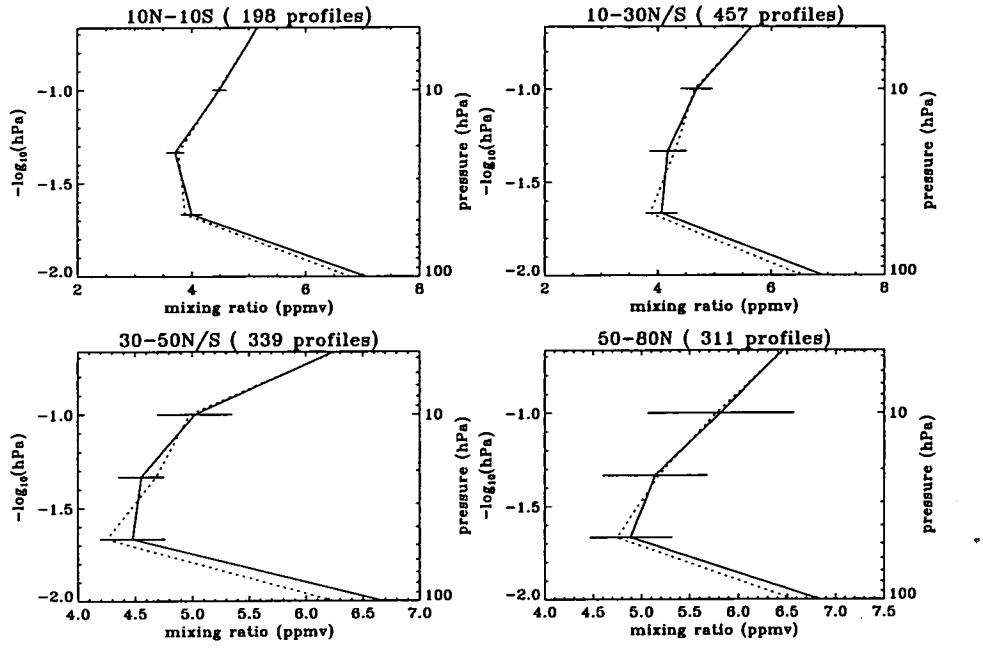

Figure 4.14: Mean retrieved profiles of H_2O within selected latitude bands for 10th January 1992. Solid line - scenario (a), dotted line - scenario (b). See text for details.

results of the scenario (a) retrievals (solid line) and the scenario (b) retrievals (dotted line). It can be seen that the increase in mixing ratio at 22 hPa and the decrease in mixing ratio at 100 hPa, which were found for the scenario (b) and (c) retrievals for 30th August 1992, are not nearly as significant for the scenario (b) retrieval on 10th January 1992, and a smoother retrieved profile is produced.

4.4 Summary and Discussion

In this chapter a problem with the retrieval of H_2O in the lower stratosphere at high latitudes during winter was illustrated. It was found that the retrievals at 46 hPa and 22 hPa contained an increased contribution from the *a priori* information at high latitudes during the polar winter. The areas covered by these poor retrievals were highly correlated with the regions of cold air

associated with the polar vortex.

This increase in the contribution from the *a priori* information is due to a corresponding loss of information from the radiance measurements. This is caused by the use of an opacity criterion which does not permit radiance measurements to be included in the retrieval if they arise from limb paths of optical thickness greater than a prescribed critical value. A method to improve the retrieval of H_2O at 46 hPa and 22 hPa was developed and tested. This involved the design of a channel-dependent opacity criterion which allowed radiance measurements, in channels 1, 2, 14 and 15, arising from limb paths of greater optical thickness than before, to be included in the retrieval. This channel-dependent opacity criterion was incorporated into a version of the MLS retrieval algorithm and test retrievals were performed using both simulated radiances and MLS measured radiances.

For the retrievals based on simulated radiances, it was found that, at 46 hPa, a substantial increase in the contribution from the measurements was possible coinciding with an improvement in the ability of the retrieval to track the true mixing ratios, particularly over the polar region. At 22 hPa, a substantial increase in the contribution from the measurements was also possible with the truth-tracking ability of the retrieval remaining as good as, and certainly no worse than, the MLS Version 3 retrieval.

For the retrievals based on MLS measured radiances, a similar increase in the contribution from the measurements was found to be possible, at both 46 hPa and 22 hPa. However, for the retrievals based on measurements from 30th August 1992, an increase in the critical value of optical thickness permitted in channels 1, 2, 14 and 15 appeared to result in a significant increase in the retrieved mixing ratio (up to 1 ppmv) at 22 hPa. This may be due to nonlinearities caused by the use of radiance measurements which arise from optically thick limb paths or may be induced by a decrease in the retrieved mixing ratio at 100 hPa which is caused by a slight increase in the contribution from the measurements to the retrieval at this pressure level. This artefact was not so apparent for retrievals based on measurements from 10th January 1992,

and no evidence of it was seen in the retrievals based on simulated radiances.

Because of the above mentioned artefact in the retrieval, it is not recommended that the channel-dependent opacity criterion, with increased critical values for channels 1, 2, 14, and 15, be implemented into the operational MLS retrieval until further investigation is performed and a fuller understanding of this problem is gained. Future versions of the MLS retrieval algorithms will incorporate a nonlinear retrieval method which will allow the use of radiance measurements from optically thick limb paths. A nonlinear iterative retrieval scheme to retrieve H_2O from MLS radiance measurements is under development at Edinburgh University.

Chapter 5

Possibility of retrieving H_2O at higher vertical resolution

5.1 Introduction

In this chapter the possibility of retrieving H_2O mixing ratios at higher vertical resolution than nominal is investigated. For MLS Version 3 the H_2O mixing ratio is retrieved at pressure levels of $z = -3.0 + \frac{n}{3}$ where $n = 0, ..., 19$ and z is in units of $-\log_{10}$(hPa). This gives an inter-level separation of 5–6 km. The vertical width of the field-of-view (FOV), as determined by the separation of the half-power points, for the MLS 183 GHz radiometer is 3.7 km [*Jarnot et al., 1994*]. Also, *Waters, [1993]* showed that for an optically thin ray path, half of the total limb radiation arises from an atmospheric layer of 3.2 km vertical extent above the tangent point. Thus, it seems reasonable to suggest that H_2O could be retrieved to a vertical resolution of better than the nominal 5–6 km. Retrievals on a higher vertical resolution are desirable, as intimated by *Mote et al., [1995]* in their study of variations in tropical lower stratospheric H_2O in relation to the annual cycle in tropical tropopause temperatures. In this paper, MLS Version 3 H_2O data in the lower stratosphere are compared with model values, but the comparison is confounded by the fact that the vertical resolution of the MLS retrievals is somewhat poorer than that of the models

used.

In Section 5.2 the possibility of retrieving H_2O at higher vertical resolution from measurements made on the nominal MLS scan pattern are investigated. This would involve reprocessing only of the existing data and would not require new measurements to be made. The methods of characterisation and error analysis described in Chapter 2 and applied in Chapter 3, are used to investigate the possibility of retrieving H_2O on grids of twice and four times the nominal vertical resolution. The nature of the averaging kernels, the vertical resolution and the estimated retrieval errors are studied in order to decide whether such retrievals are possible. Also in this section the effects of including off-diagonal elements in the *a priori* covariance matrix are investigated.

In section 5.3 the effects on the retrieval of H_2O using a scan pattern of higher resolution than the nominal MLS scan pattern are investigated. An assessment of whether the nominal scan pattern is under-sampling the atmosphere is given; would radiance measurements at higher vertical resolution add any significant information to the retrievals ? Again, retrievals on grids of resolution twice and four times that of the nominal retrieval grid are investigated and the resulting averaging kernels, vertical resolution and estimated retrieval errors are studied.

The retrieval errors considered in this work are all random in nature, including the smoothing error. No attempt has been made to estimate the effects of systematic errors. In section 5.4 the results of the above studies are summarised and discussed.

5.2 With nominal MLS scan pattern

In this section the possibility of retrieving H_2O at higher vertical resolution than nominal using the nominal MLS scan pattern is investigated. As a reminder, MLS Version 3 H_2O mixing ratios are retrieved on pressure surfaces $z = -3.0 + \frac{n}{3}$ where $n = 0, ..., 19$ and z is in units of $-\log_{10}$(hPa). This gives an inter-level separation of 5–6 km. The two retrieval grids of higher resolu-

tion which are employed in the following study are defined as follows. The grid having twice the vertical resolution as nominal is $z = -3.0 + \frac{n}{6}$ where $n = 0, ..., 41$ and the grid of four times the nominal resolution is $z = -3.0 + \frac{n}{12}$ where $n = 0, ..., 83$. These two grids give inter-level separations equivalent to 2.5–3 km and ~ 1.5 km, respectively.

In the work presented below, the effect of including non-zero off-diagonal elements in the *a priori* covariance matrix is also investigated. As mentioned in Chapter 2, the diagonal elements of this matrix represent the *a priori* variance at each level and the off-diagonal elements represent inter-level covariances. For MLS Version 3 retrievals the *a priori* covariance matrix for H_2O is purely diagonal, i.e., all off-diagonal elements are set to zero. However, if some idea of the length scale of correlations is available, then an artificial covariance matrix, $\mathbf{S}_a$ can be constructed from equation (5.1)

$$\mathbf{S}_a^{ij} = (\mathbf{S}_a^{ii}\mathbf{S}_a^{jj})^{\frac{1}{2}} exp(-(z_i - z_j)^2/l^2), \tag{5.1}$$

where i and j represent levels of the retrieval grid and hence, rows and columns of the covariance matrix, z_i is the pressure in, $-\log_{10}$(hPa), of the ith retrieval level, and l is the length scale of correlations. Constructing the *a priori* covariance matrix in this manner assumes that correlations have a Gaussian decay with distance, in $-\log_{10}$(hPa), away from each level. Including off-diagonal elements in the *a priori* covariance matrix adds an additional constraint on the smoothness of the retrieved profile.

Before considering the possibility of retrieving H_2O on the two higher resolution grids, the effect of including non-zero off-diagonal elements in the *a priori* covariance matrix for a retrieval at the nominal resolution is investigated.

5.2.1 Nominal retrieval grid

Using equation (5.1), an *a priori* covariance matrix was constructed assuming a correlation length scale of $l = \frac{1}{3}$ [$-\log_{10}$(hPa)], which is equivalent to 5–6 km

in height. This is equal to the separation of levels of the nominal MLS retrieval grid. Applying equations (2.22) and (2.24), corresponding averaging kernels were evaluated for the retrieval of H_2O on the nominal retrieval grid. These averaging kernels are plotted in figure 5.1 and are not too dissimilar to the averaging kernels for MLS Version 3 retrievals (see figure 3.6). The peak values

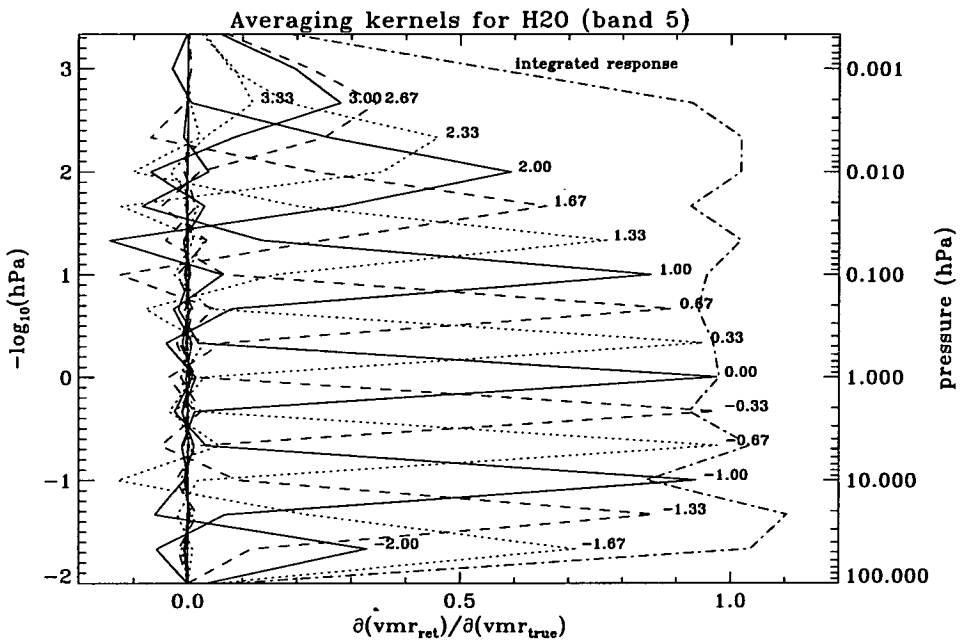

Figure 5.1: Averaging kernels for H_2O retrieval on nominal grid. A correlation length scale of 5–6 km was assumed.

of the averaging kernels have decreased slightly although the averaging kernel for $z = -2.0$ (100 hPa) is now more prominent but peaks at the wrong pressure level; 46 hPa instead of 100 hPa. Thus, introducing correlations of length scale 5–6 km into the *a priori* covariance matrix has increased the sensitivity of the retrieval at 100 hPa to perturbations in H_2O at 46 hPa but has not improved the sensitivity to perturbations at 100 hPa itself. It is noted that the integrated response at 46 hPa and 22 hPa has increased to values greater than 1 and the integrated response at 10 hPa has decreased slightly. It appears that the introduction of the inter-level correlations has created an over-response of the whole retrieved profile to perturbations at 46 hPa and 22 hPa and has reduced

the response to perturbations at 10 hPa. In fact, an oscillation seems to have been induced in the integrated response.

The vertical resolution, given by the full-width at half-maximum, $\Delta_{\frac{1}{2}}$, of the averaging kernels, is plotted in figure 5.2. Line (a) represents $\Delta_{\frac{1}{2}}$ for the

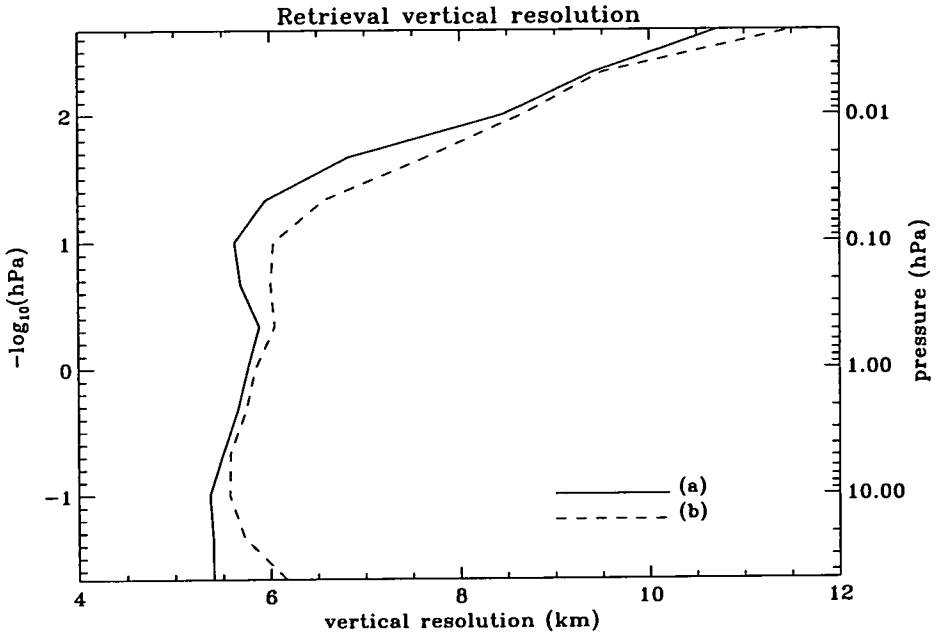

Figure 5.2: Vertical resolution of H_2O retrieval on nominal grid; (a) no inter-level correlations, (b) correlation length of 5–6 km.

MLS Version 3 retrieval. Line (b) is $\Delta_{\frac{1}{2}}$ for the retrieval assuming a correlation length scale of 5–6 km. The vertical range of the plot is restricted to between 46 hPa and 0.002 hPa where the averaging kernels are reasonably well peaked and the peak value occurs at the corresponding retrieval level. In general, the vertical resolution is poorer in the case when inter-level correlations have been assumed. This is to be expected, as the introduction of inter-level correlations causes a certain amount of vertical smoothing over the profile.

An analysis of the random errors, including the smoothing error, has been performed for the retrieval of H_2O on the nominal retrieval grid assuming a correlation length scale of 5–6 km. Figures 5.3, 5.4 and 5.5 show the smoothing error, error due to measurement noise and the total retrieval error, respectively.

The lines labelled (a) represent the estimated errors for the MLS Version 3 retrieval and those labelled (b) correspond to a retrieval assuming the presence of inter-level correlations. The main effect on the smoothing error, of intro-

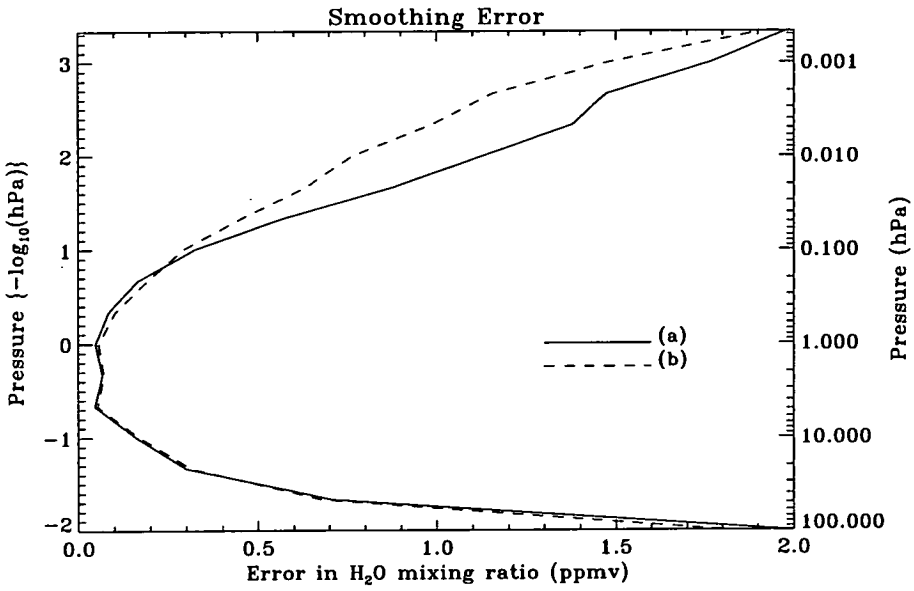

Figure 5.3: Smoothing error for H_2O retrieval on nominal grid; (a) no inter-level correlations, (b) correlation length of 5–6 km.

ducing a correlation length scale of 5–6 km, is to reduce the error significantly in the region 0.1–0.001 hPa. For example, at 0.01 hPa the smoothing error has been reduced from 1.1 ppmv to 0.7 ppmv. In this region of the atmosphere the limb views of the nominal MLS scan are $\sim$ 6 km apart (see Table 1.3) which is comparable to the spacing of the retrieval levels. The smoothing error, which reflects the contribution of the *a priori* error to the retrieval error, reduces as the introduction of inter-level correlations adds some extra information on the shape of the profile. The error due to measurement noise is mostly affected in the region 0.2–0.01 hPa, where the error has been reduced by 0.05–0.1 ppmv. Between 46 hPa and 10 hPa there is also a slight reduction in error due to measurement noise and above 0.002 hPa there is an increase in the error. The total retrieval error (see figure 5.5) is given by the root-sum-square of the error

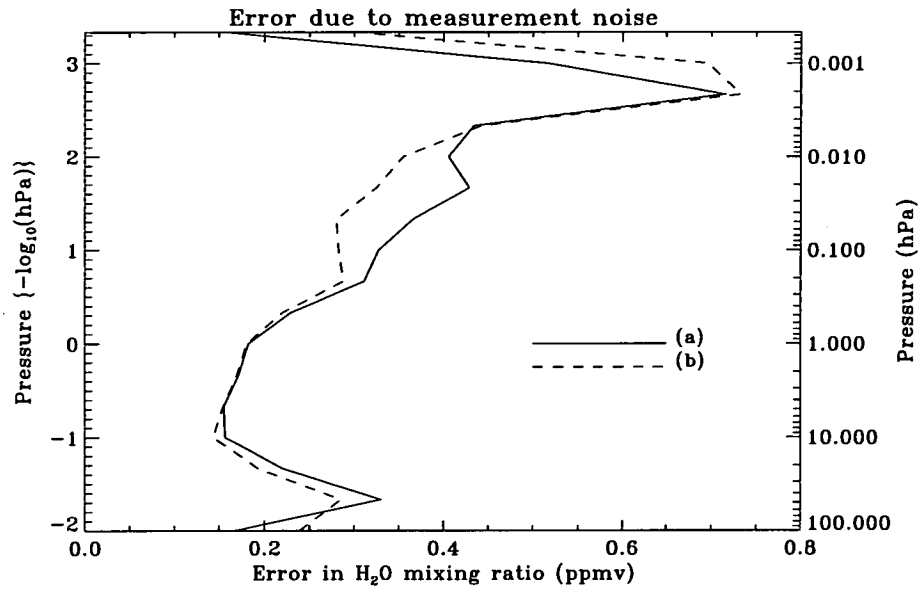

Figure 5.4: Error due to measurement noise for H_2O retrieval on nominal grid; (a) no inter-level correlations, (b) correlation length of 5–6 km.

due to measurement noise, errors due to temperature and tangent pressure errors, and the smoothing error. It can be seen that the main effect of assuming a correlation length scale of 5–6 km is to significantly reduce the total error above 0.1 hPa. This is due mainly to the resulting reduction in the smoothing error in this region. Below 4.6 hPa there is a small reduction in the total error.

In summary, the effect of introducing a correlation length scale of 5–6 km to the *a priori* covariance matrix is to reduce the vertical resolution of the H_2O retrieval by as much as 0.5 km and to reduce the retrieval error above 0.1 hPa by as much as 0.3 ppmv. Thus, there is no improvement to the retrieval of H_2O below 0.1 hPa but above this level, where the nominal MLS scan pattern is more sparse, the error in retrieved H_2O is significantly reduced with a small loss of vertical resolution.

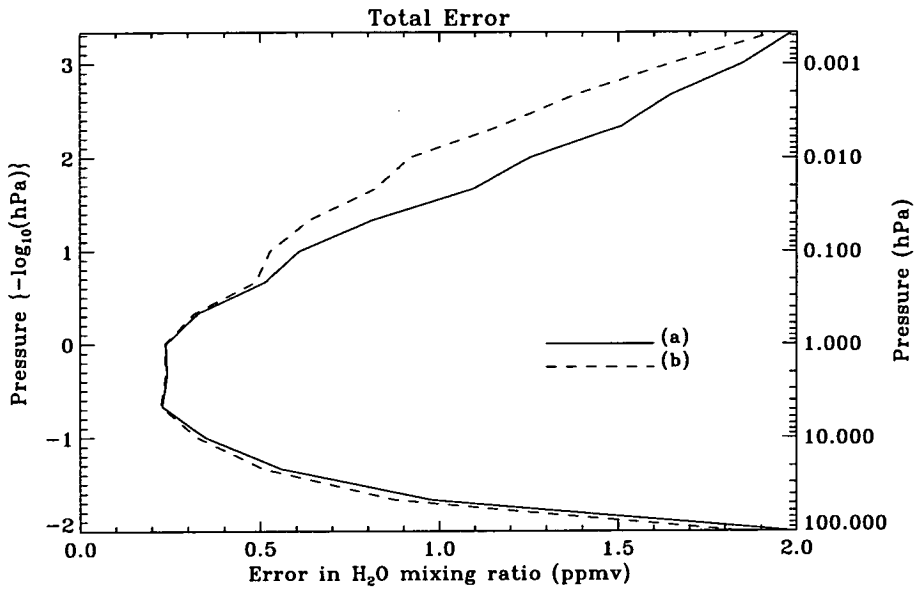

Figure 5.5: Total error for H_2O retrieval on nominal grid; (a) no inter-level correlations, (b) correlation length of 5–6 km.

5.2.2 Retrieval grid of resolution 2 x nominal

In this section the possibility of retrieving H_2O on a grid of twice the vertical resolution as the nominal grid using measurements on the nominal MLS scan pattern is investigated. Influence functions (K-matrices) were evaluated using a basis representation for H_2O profiles which was twice the resolution as that for the nominal retrieval. Also, the effects of including non-zero off-diagonal elements in the *a priori* covariance matrix are studied. Two different correlation length scales have been employed separately. Equation (5.1) was used to construct two *a priori* covariance matrices; one assuming a length scale of $l = \frac{1}{6}$ [$-\log_{10}$(hPa)] which is equivalent to 2.5–3 km, half of the separation of levels of the nominal MLS retrieval grid, the other assuming $l = \frac{1}{3}$ [$-\log_{10}$(hPa)] which is equivalent to 5–6 km, equal to the separation of the levels of the nominal MLS retrieval grid.

Figure 5.6 shows the resulting averaging kernels when all off-diagonal elements of the *a priori* covariance matrix are set to zero, i.e., no inter-level

correlations are assumed. The averaging kernels for the case where the correlation length scale is 5–6 km are shown in figure 5.7. In both figures alternate rows of the averaging kernel matrix are plotted. For the case where

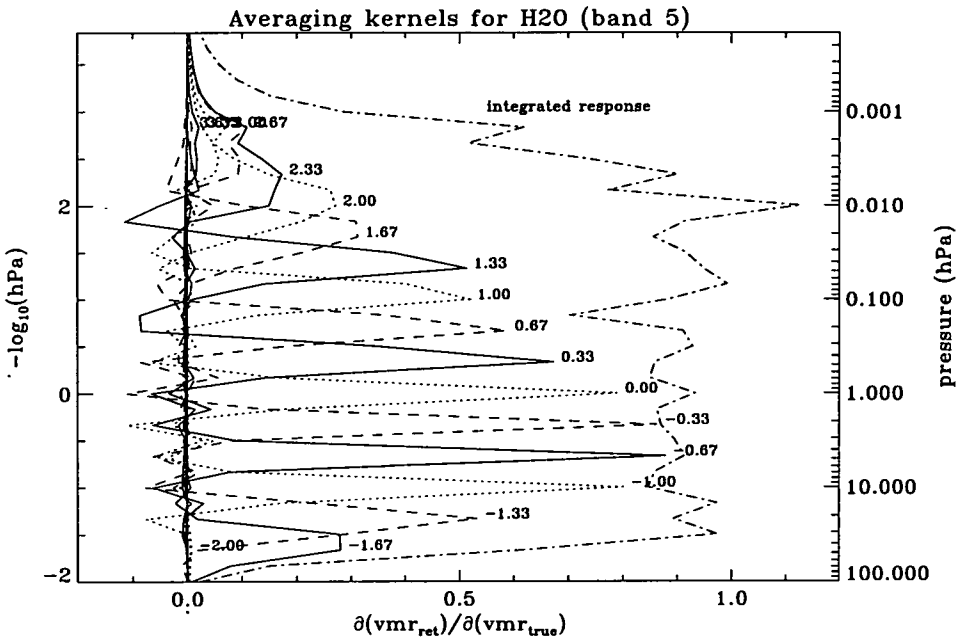

Figure 5.6: Averaging kernels for H_2O retrieval on a grid of twice the nominal resolution. No inter-level correlations have been assumed. Alternate rows of the averaging kernel matrix are plotted.

no inter-level correlations are assumed, the averaging kernels are reasonably well-peaked functions in the range 20–0.046 hPa. In the upper stratosphere the peak values are close to 1 and the averaging kernels have smallest width in this region. The introduction of a correlation length scale of 5–6 km to the *a priori* covariance matrix tends to widen the averaging kernels and reduce the peak values. This smoothing effect is more evident for the retrieval on this higher resolution grid than it was for the retrieval on the nominal grid. As in section 5.2.1, the introduction of a correlation length scale appears to induce oscillations in the integrated response. Thus, the whole retrieved profile overresponds to perturbations in the real atmosphere at some levels, e.g. 22 hPa, and the response to perturbations at other levels is reduced, e.g. 0.0046 hPa. For the case where the correlation length scale is 2.5–3 km, the smoothing

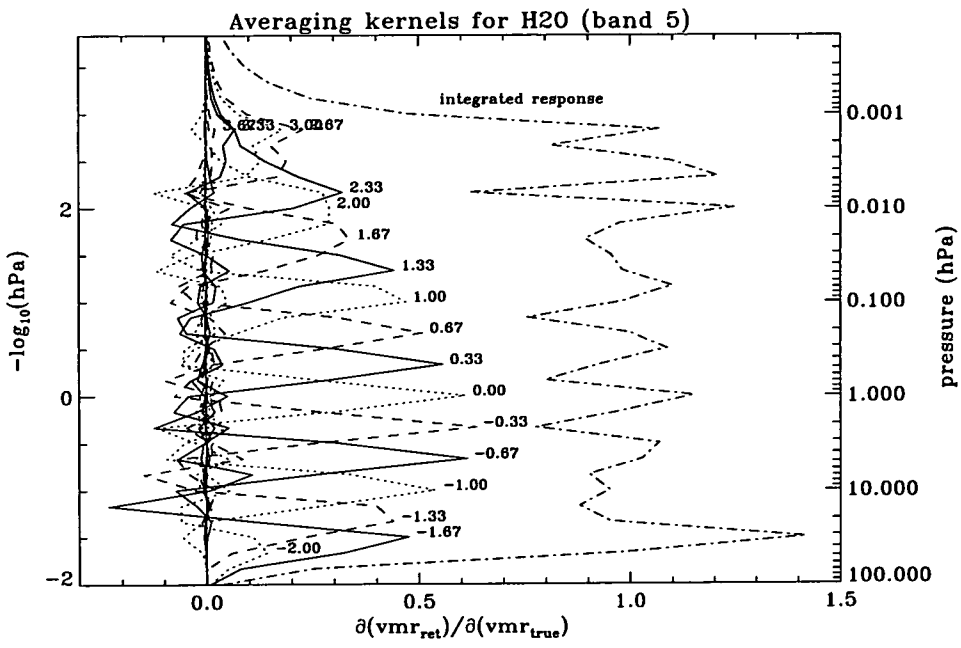

Figure 5.7: Averaging kernels for H_2O retrieval on a grid of twice the nominal resolution. A correlation length scale equivalent to 5–6 km has been assumed. Alternate rows of the averaging kernel matrix are plotted.

effect on the averaging kernels is not as great as that with a length scale of 5–6 km, which is to be expected, and the peak values lie somewhere between those in figures 5.6 and 5.7.

The vertical resolution of the H_2O retrievals for the three cases are plotted in figure 5.8 and the corresponding estimated retrieval errors are plotted in figure 5.9. In both figures the line labelled (a) corresponds to the case where no inter-level correlations are assumed, the line labelled (b) corresponds to the case where a correlation length scale of 2.5–3 km is assumed, and the line labelled (c) corresponds to the case where the assumed correlation length scale is 5–6 km. The vertical resolution in figure 5.8 is represented by the full-width at half-maximum, $\Delta_{\frac{1}{2}}$, of the averaging kernels and is plotted over the range 46–0.0046 hPa where the functions are reasonably well peaked. From figure 5.8 it can be seen that a vertical resolution of 3–4 km appears to be attainable for the cases where no inter-level correlations are assumed and where a correlation length of 2.5–3 km is assumed, the vertical resolution being slightly poorer for

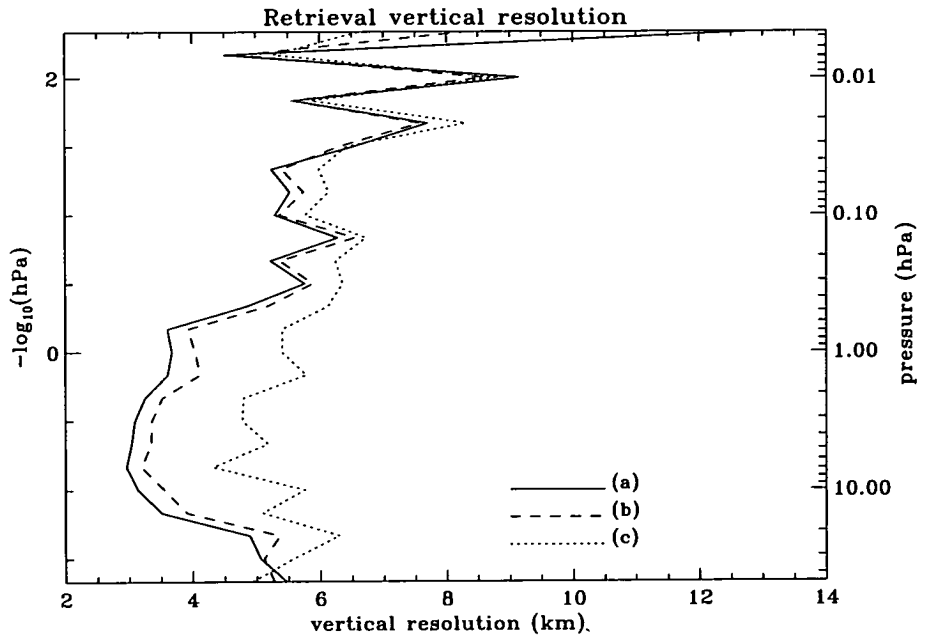

Figure 5.8: Vertical resolution of H_2O retrieval on a grid of twice the nominal resolution; (a) no inter-level correlations, (b) correlation length of 2.5–3 km, (c) correlation length of 5–6 km.

the latter of these two cases. For the case (c), the smoothing effect of the correlation length of 5–6 km is such that the vertical resolution in this region is degraded to 4.5–6 km. It can be seen from figure 5.9 that the introduction of inter-level correlations in the *a priori* covariance matrix has the effect of reducing the retrieval error. In the case where a correlation length of 5–6 km is assumed, a considerable reduction in retrieval error is obtained, but at the expense of a loss in vertical resolution (see figure 5.8) which is particularly significant in the upper stratosphere. This reduction in retrieval error is mainly due to a significant reduction in the smoothing error (not shown here) which reflects a reduction in the contribution of the *a priori* error to the retrieved error.

In summary, for the retrieval of H_2O on a grid with inter-level separation 2.5–3 km, which is twice the resolution of the nominal grid, it appears that this vertical resolution is not attainable. However, for a retrieval which assumes that no inter-level correlations are present or one which assumes a correlation

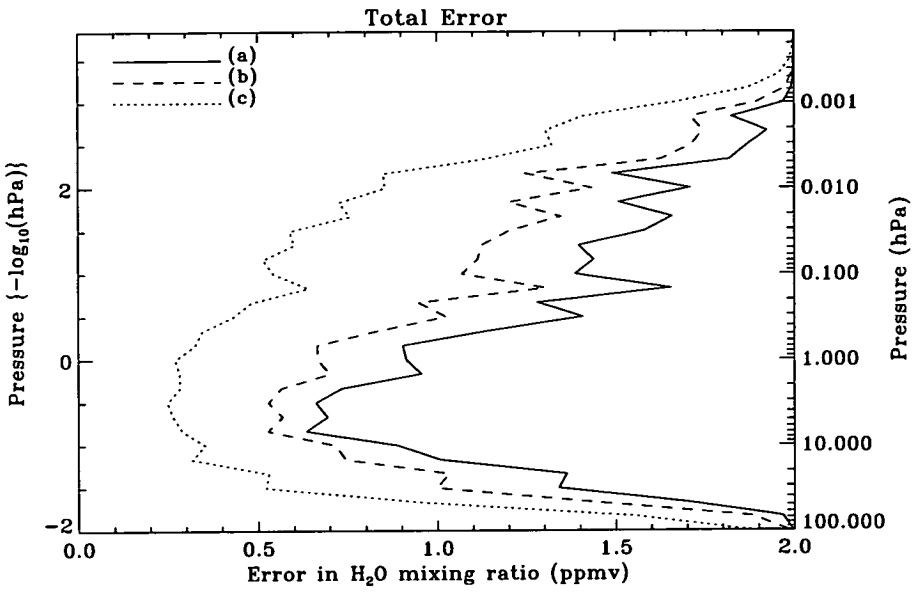

Figure 5.9: Total error for H_2O retrieval on a grid of twice the nominal resolution; (a) no inter-level correlations, (b) correlation length of 2.5–3 km, (c) correlation length of 5–6 km.

length of 2.5–3 km, it appears that a vertical resolution of 3–4 km is possible in the range 15–0.7 hPa with a corresponding retrieval error of less than 1 ppmv. In this region of the atmosphere the separation of limb views for the nominal MLS scan is $\sim$3 km. Above, this region the limb views are separated by $\sim$6 km and the vertical resolution of the retrievals appears to be limited to $\sim$6 km. The introduction of inter-level correlations in the *a priori* covariance matrix gives a reduction in the retrieval error at the expense of a loss of vertical resolution due to smoothing of the averaging kernels. The larger the assumed correlation length, the greater the reduction in error and the greater the corresponding loss in vertical resolution.

5.2.3 Retrieval grid of resolution 4 x nominal

In this section the possibility of retrieving H_2O on a grid of four times the vertical resolution as the nominal grid using measurements on the nominal MLS scan pattern is investigated. This retrieval grid has an inter-level separation

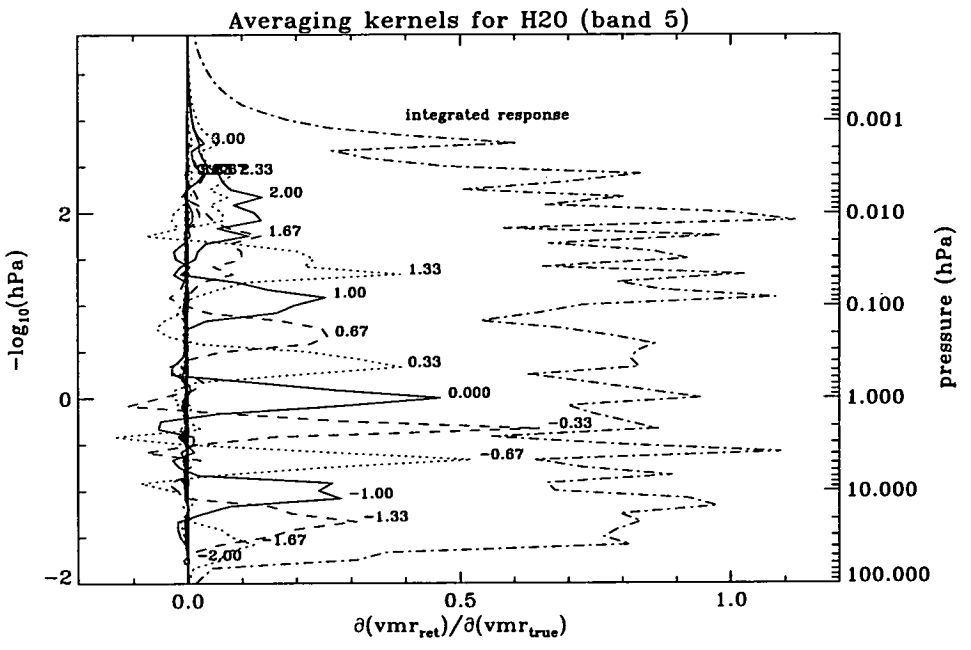

Figure 5.10: Selected averaging kernels for H_2O retrieval on a grid of four times the nominal resolution. No inter-level correlations have been assumed.

of $\frac{1}{12}$ [$-\log_{10}$(hPa)] which is equivalent to ~ 1.5 km. Influence functions (**K**-matrices) were evaluated using a basis representation for H_2O profiles which was four times the resolution of that for the nominal retrieval. The effects of including non-zero off-diagonal elements in the *a priori* covariance matrix are also studied. Two different correlation length scales have been employed separately as in section 5.2.2. Equation (5.1) was used to construct two *a priori* covariance matrices; one assuming a length scale of $l = \frac{1}{6}$ [$-\log_{10}$(hPa)] which is equivalent to 2.5–3 km and the other assuming $l = \frac{1}{3}$ [$-\log_{10}$(hPa)] which is equivalent to 5–6 km.

Selected rows of the averaging kernel matrix for the retrieval of H_2O on a grid of four times the resolution of the nominal grid are plotted in figures 5.10 and 5.11. Figure 5.10 corresponds to the case when no inter-level correlations are assumed and figure 5.11 corresponds to the case where a correlation length of 5–6 km is assumed. The averaging kernels in figure 5.10 generally have peak values of less than 0.5 and have width somewhat greater than the inter-level separation of the retrieval grid. This shows that the retrieval cannot

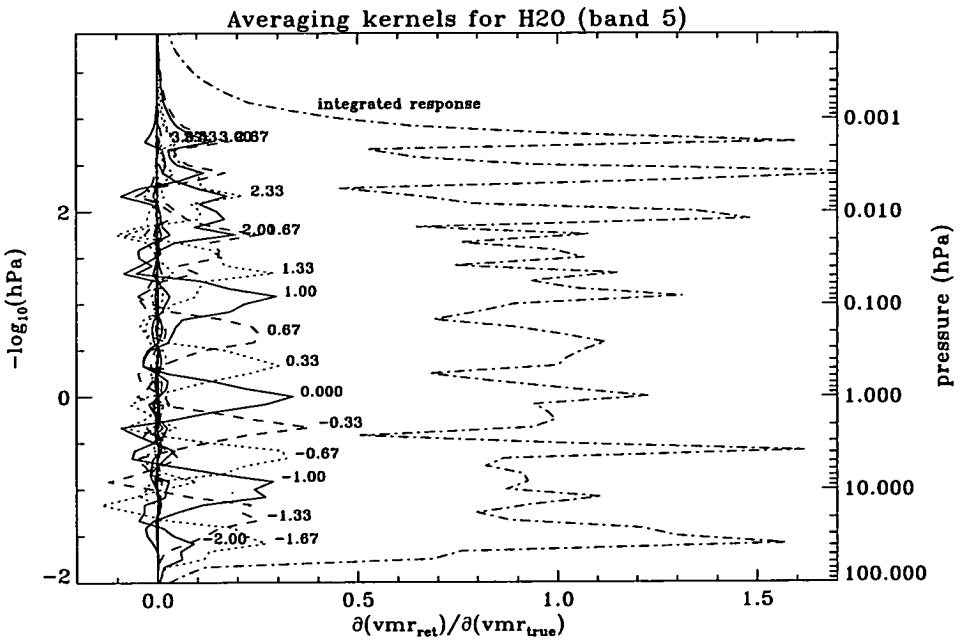

Figure 5.11: Selected averaging kernels for H_2O retrieval on a grid of four times the nominal resolution. A correlation length scale of 5–6 km has been assumed.

resolve structures on such a small vertical scale. The integrated response, which reflects the response of the whole retrieved profile to a perturbation in the real atmosphere at a particular pressure level, is highly oscillatory in nature and oscillates about a value of 0.8 throughout the stratosphere and mesosphere. From figure 5.11 it can be seen that assuming the presence of inter-level correlations of length scale 5–6 km tends to reduce the peak values of the averaging kernels and produces some smearing in the vertical. The amplitude of oscillation of the integrated response is also increased. For the case where a correlation length of 2.5–3 km is assumed, the peak values of the averaging kernels lie between those in figures 5.10 and 5.11 and the vertical smearing of the averaging kernels is less than that when a correlation length of 5–6 km is used.

The vertical resolution of the retrieval is shown in figure 5.12 and the estimated retrieval error is plotted in figure 5.13. In both of these figures, the line labelled (a) corresponds to the case where no inter-level correlations

are assumed, the line labelled (b) corresponds to the case where inter-level correlations of length scale 2.5–3 km are assumed, and the line labelled (c) corresponds to the case where the assumed correlation length scale is 5–6 km. The vertical resolution is represented by the full-width at half-maximum, $\Delta_{\frac{1}{2}}$,

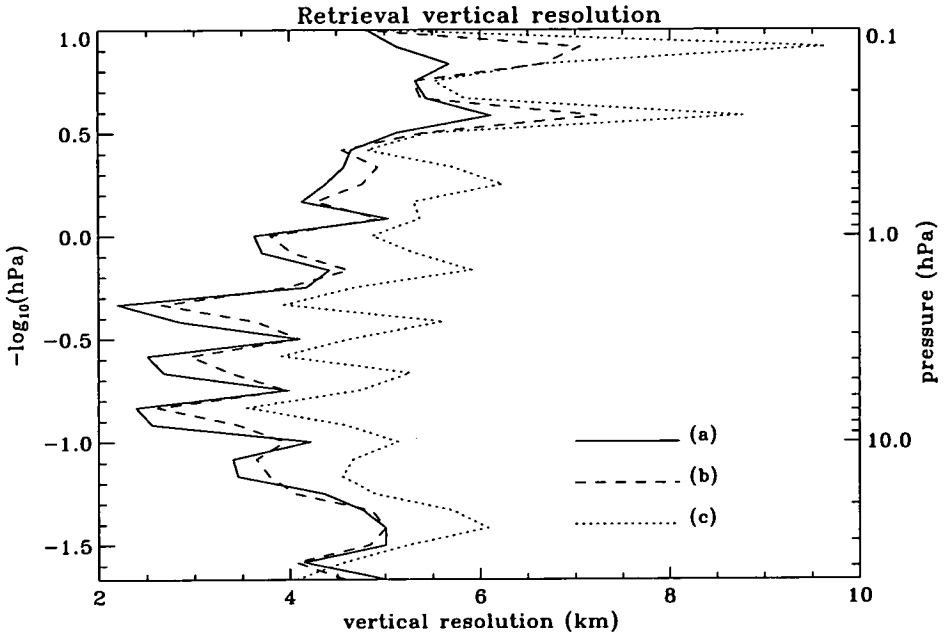

Figure 5.12: Vertical resolution of H_2O retrieval on a grid of four times the nominal resolution; (a) no inter-level correlations, (b) correlation length of 2.5–3 km, (c) correlation length of 5–6 km.

of the averaging kernels and is plotted in figure 5.12 over the range 46–0.1 hPa where the averaging kernels are reasonably well peaked functions. In all three cases the vertical resolution tends to oscillate. For the case with no assumed inter-level correlations it appears that a vertical resolution of 2.5–4 km may be attainable in the range 15–2 hPa. Over this same pressure range, the retrieval assuming a correlation length of 2.5–3 km appears to achieve a vertical resolution of 3–4 km. When a correlation length of 5–6 km is assumed, the vertical resolution oscillates between 4 and 6 km over the range 46–0.3 hPa. Vertical resolutions equivalent to the retrieval grid spacing of ~ 1.5 km do not seem to be possible. This implies that the retrieval cannot resolve structures on such a small vertical scale. For all three cases the estimated errors in the retrieval of

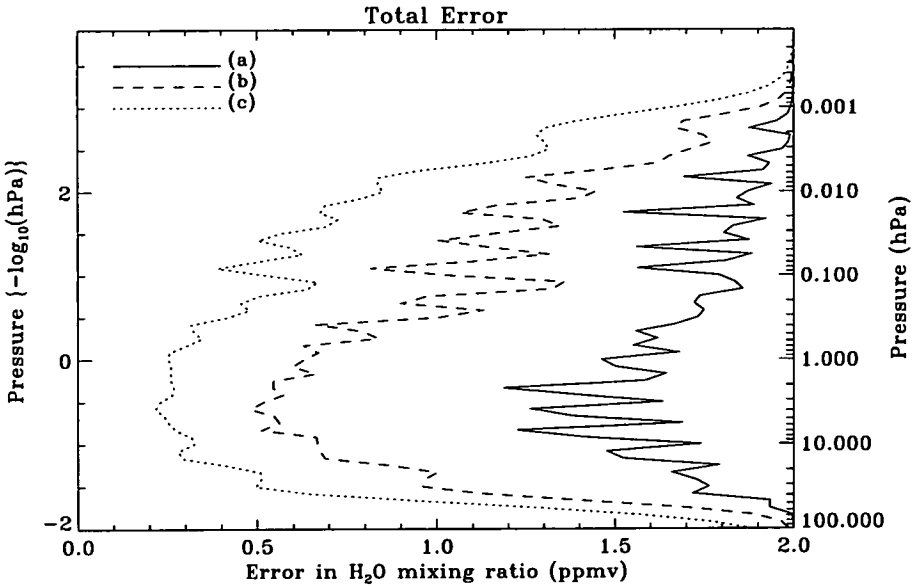

Figure 5.13: Total error for H_2O retrieval on a grid of four times the nominal resolution; (a) no inter-level correlations, (b) correlation length of 2.5–3 km, (c) correlation length of 5–6 km.

H_2O on the grid of resolution four times that of the nominal grid are plotted in figure 5.13. When no inter-level correlations are assumed the retrieved error is rather oscillatory in nature and the error is not much less than the *a priori* error, remembering that the *a priori* error is set to 2 ppmv at 100 hPa and above. Introducing inter-level correlations into the *a priori* covariance matrix has the effect of smoothing the error profile and significantly reducing the size of the retrieved error. This is mainly due to a reduction in the smoothing error (not shown here).

Thus, if a retrieval grid of resolution ~ 1.5 km is used then inter-level correlations are required to reduce the retrieved error to satisfactory values, i.e., less than half the value of the *a priori* error. However, it appears that using a retrieval grid of such high resolution is unnecessary since this level of vertical resolution seems unattainable.

5.3 With simulated high resolution scan pattern

In this section the effect of performing radiance measurements at higher vertical resolution than the nominal MLS scan pattern is investigated. A higher resolution scan pattern is simulated and the resulting effects on the vertical resolution and the estimated error for retrieved H_2O are studied.

Radiance measurements at higher vertical resolution have been simulated by simply taking typical MLS band 5 measured radiances and associated noise values and linearly interpolating them onto a grid representing the tangent pressures of the high resolution scan. This high resolution grid is defined as $z = -3.0 + \frac{n}{12}$, where n = 0,...,84 and z is in units of $-\log_{10}$(hPa). This simulates a limb scan from 0 km (1000 hPa) to 106 km (0.0001 hPa) with each limb view separated by $\sim$ 1.5 km. This compares to the nominal MLS scan which ranges from $\sim$ 3 km to $\sim$ 90 km and has a vertical resolution of 1.5–2 km in the lower stratosphere, 3–4 km in the upper stratosphere and lower mesosphere and 6 km in the upper mesosphere (see Table 1.3). Linearly interpolating the radiance noise in this manner makes the assumption that the integration time for each limb view is equivalent to that for the nominal scan, i.e., 1.8 seconds. For the high resolution scan defined above, this would result in one complete limb scan being performed in 183 seconds (allowing 0.2 seconds for the FOV to move between limb views and a total of 13 seconds per limb scan for calibration, equivalent to the nominal scan), as opposed to $\sim$ 65 seconds for the nominal scan. The UARS orbital motion (7 km/s) would therefore smear the measurement of one profile with the high resolution scan by $\sim$ 1300 km in a direction perpendicular to the line of sight compared to $\sim$ 400 km nominally. Thus, in order to perform a limb scan with such a high vertical resolution and to maintain the nominal horizontal resolution, the integration time for each limb view would have to be reduced to $\sim$ 0.4 seconds. A limb scan, on the high resolution grid defined above, with an integration time of 0.4 seconds for each limb view has also been simulated by scaling the radiance noise appropriately. From *Meeks, [1976]*, the root-mean-square (rms) noise, ϵ, of a radiometric

measurement is inversely proportional to the square root of the integration time, t, for the measurement, i.e., $\epsilon \propto t^{-1/2}$. Using this relationship, the radiance noise, which was interpolated onto the high resolution grid, must be doubled to correspond to an integration time of 0.4 seconds.

In the work presented below, the effects on the retrieval of H_2O using measurements on the simulated high resolution limb scan, with integration times for limb views of 1.8 seconds and 0.4 seconds, are investigated. Firstly, the effects on a retrieval at the nominal resolution are studied and then the possibility of performing retrievals on grids of resolution twice and four times that of the nominal grid is considered. In the following work the effect of the opacity criterion (see Chapter 2) is included and inter-level correlations of length scale $\frac{1}{3}$ [$-\log_{10}$(hPa)], which is equivalent to 5–6 km in height, are assumed.

5.3.1 Nominal retrieval grid

In this section the effect on the retrieval of H_2O on the nominal grid when using simulated measurements on the high resolution scan pattern described above is investigated. Both cases where the integration time of each limb view is 1.8 seconds and 0.4 seconds are considered.

Figure 5.14 shows the resulting averaging kernels for the H_2O retrieval using measurements with an integration time of 1.8 seconds. These are to be compared with those of figure 5.1 which used measurements on the nominal scan pattern and assumed the presence of inter-level correlations with a length scale of 5–6 km. The main difference is that, above 0.1 hPa, the peak values of the averaging kernels have increased. This reflects the extra information that is added by the higher resolution measurements in this region where the separation of limb views is ~ 1.5 km for the simulated scan compared to ~ 6 km for the nominal scan. The peak values of the averaging kernels at 22 hPa and 46 hPa have also increased slightly. The averaging kernels for the case where the integration time of each limb view is 0.4 seconds are similar to those in figure 5.14 except that the peak values are reduced slightly due to the increased

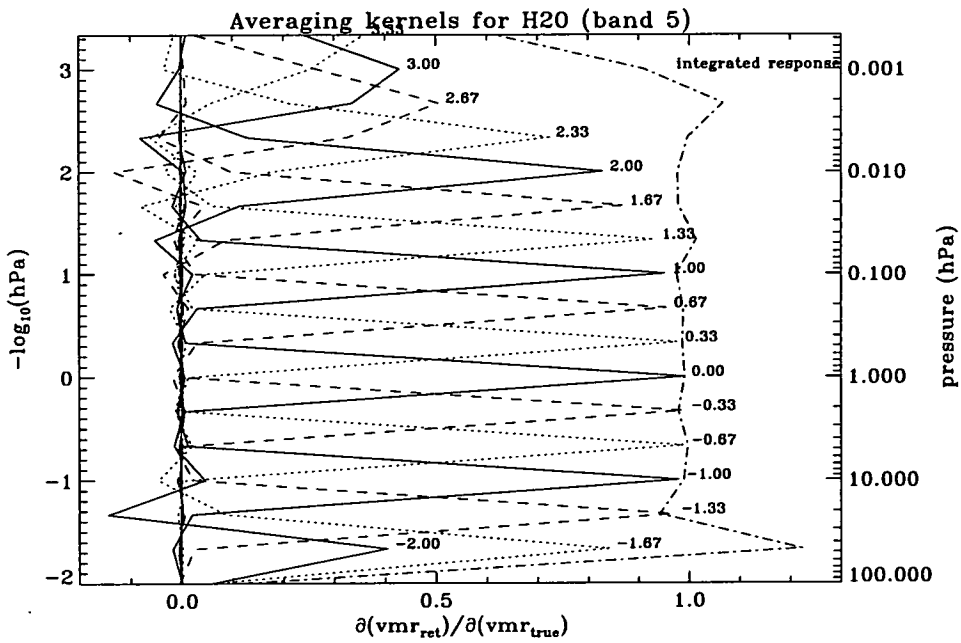

Figure 5.14: Averaging kernels for H_2O retrieval on nominal grid. Measurements from a limb scan of ~ 1.5 km resolution have been simulated. The integration time for each limb view is 1.8 seconds. A correlation length scale of 5–6 km has been assumed.

measurement noise resulting from the shorter integration time.

Figures 5.15, 5.16, 5.17 and 5.18 show the vertical resolution, the smoothing error, the error due to measurement noise and the total retrieval error, respectively, for the retrieval of H_2O on the nominal grid using simulated measurements on the high resolution scan. In all of these figures the line labelled (a) corresponds to the case where measurements on the nominal MLS scan are used, the line labelled (b) corresponds to the case where simulated measurements with an integration time of 1.8 seconds on the high resolution scan are used and the line labelled (c) is for the case which is similar to that for (b) but the integration time is 0.4 seconds. In figure 5.15 the vertical resolution of the retrieval is represented by the full-width at half-maximum, $\Delta_{\frac{1}{2}}$, of the averaging kernels. It can be seen that, above 0.46 hPa, the vertical resolution of the retrieval is greatly improved by the inclusion of radiance measurements at 1.5 km intervals, e.g. at 0.02 hPa the resolution of the retrieval has improved

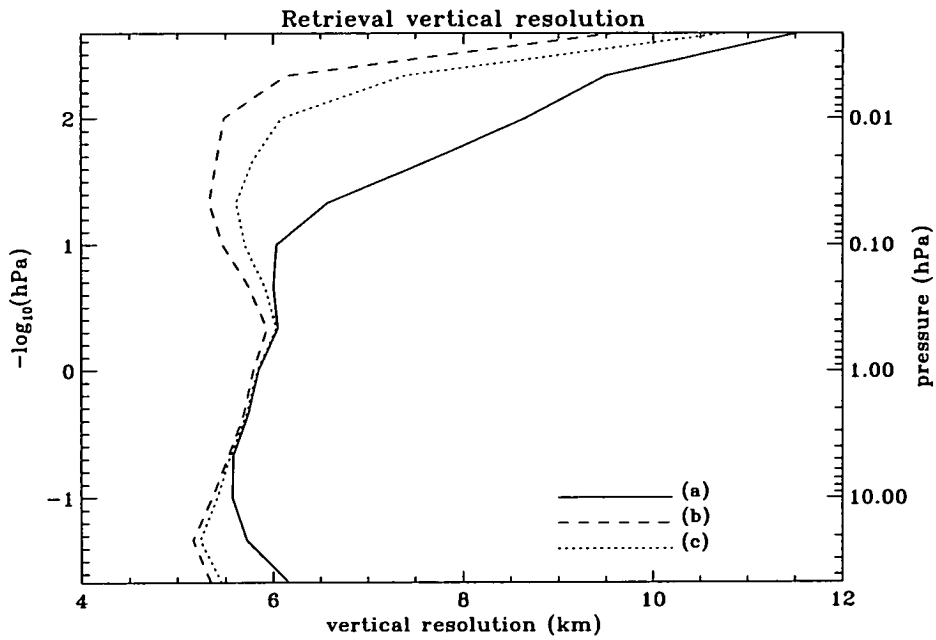

Figure 5.15: Vertical resolution of H_2O retrieval on nominal grid; (a) measurements on nominal MLS limb scan, (b) simulated measurements with integration time of 1.8 seconds on limb scan of resolution 1.5 km, (c) as for (b) but integration time of 0.4 seconds.

from 7.7 km to 5.5 km. Also, between 46 hPa and 4.6 hPa, the resolution of the retrieval has improved by up to 0.5 km. In the range 4.6–0.46 hPa the vertical resolution of the retrieval is practically unchanged. In this region the vertical resolution of the retrieval is close to the resolution of the basis representation for H_2O which was used in the evaluation of the influence functions and this resolution sets an upper limit on the resolution of the retrieval. Using measurements with an integration time of 0.4 seconds, as opposed to 1.8 seconds, degrades the vertical resolution slightly but significant improvements in the resolution are still apparent when compared to that using the nominal MLS scan pattern.

From figure 5.16 it can be seen that the smoothing error is reduced at most pressure levels when the simulated measurements with an integration time of 1.8 seconds on the high resolution limb scan are used in place of the measurements from the nominal limb scan. The reduction in smoothing error

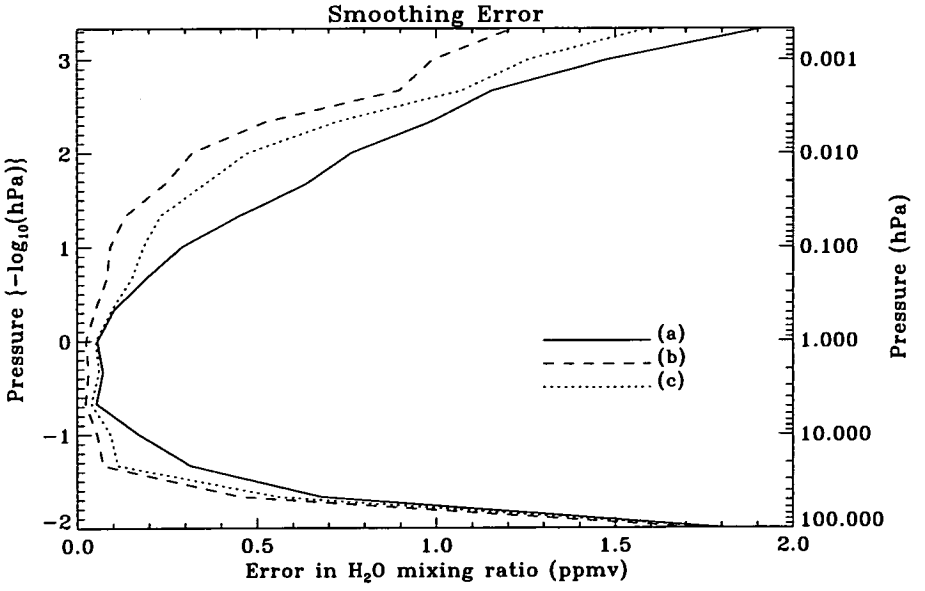

Figure 5.16: Smoothing error for H_2O retrieval on nominal grid; (a) measurements on nominal MLS limb scan, (b) simulated measurements with integration time of 1.8 seconds on limb scan of resolution 1.5 km, (c) as for (b) but integration time of 0.4 seconds.

is most significant above 0.46 hPa and between 46 hPa and 4.6 hPa. Thus, the measurements on the high resolution scan pattern appear to be adding useful information to the retrieval which reduces the weight on the *a priori* information and hence reduces the smoothing error. When measurements with an integration time of 0.4 seconds, as opposed to 1.8 seconds, are used, the reduction in smoothing error is not as great due to the increased noise on the measurements resulting from the shorter integration time. However, a significant reduction in smoothing error is still achieved above 0.46 hPa and between 46 hPa and 4.6 hPa.

A comparison of the errors due to measurement noise are shown in figure 5.17. Using measurements with an integration time of 1.8 seconds on the high resolution limb scan tends to decrease the error due to measurement noise between 46 hPa and 0.002 hPa. Using measurements with an integration time of 0.4 seconds on the high resolution limb scan gives an error due to

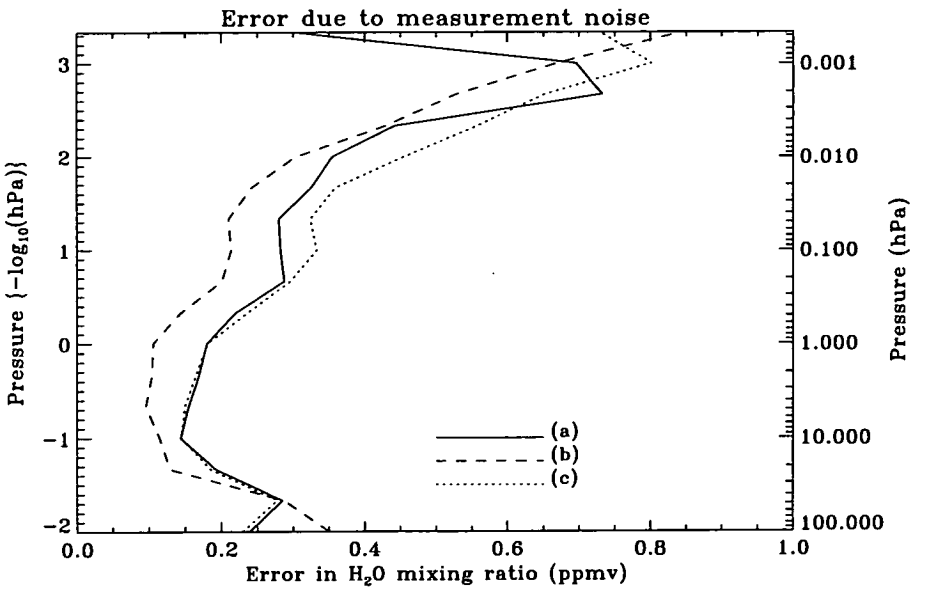

Figure 5.17: Error due to measurement noise for H_2O retrieval on nominal grid; (a) measurements on nominal MLS limb scan, (b) simulated measurements with integration time of 1.8 seconds on limb scan of resolution 1.5 km, (c) as for (b) but integration time of 0.4 seconds.

measurement noise equivalent to that from the nominal MLS limb scan for retrievals below 0.2 hPa. Above 0.2 hPa, the error due to measurement noise tends to be greater for the high resolution measurements with integration time of 0.4 seconds.

Figure 5.18 shows the total error for the retrieval of H_2O on the nominal grid. For the case where the high resolution measurements with an integration time of 1.8 seconds are used in place of the measurements from the nominal limb scan, the total retrieval error is reduced at 46 hPa and above. When the high resolution measurements with an integration time of 0.4 seconds are used the reduction in total retrieval error is not as great but remains significant at levels above 0.2 hPa and between 46 hPa and 4.6 hPa.

To summarise, using measurements with an integration time of 1.8 seconds from a limb scan of vertical resolution ~ 1.5 km, in place of measurements from the nominal MLS limb scan, would appear to significantly reduce the

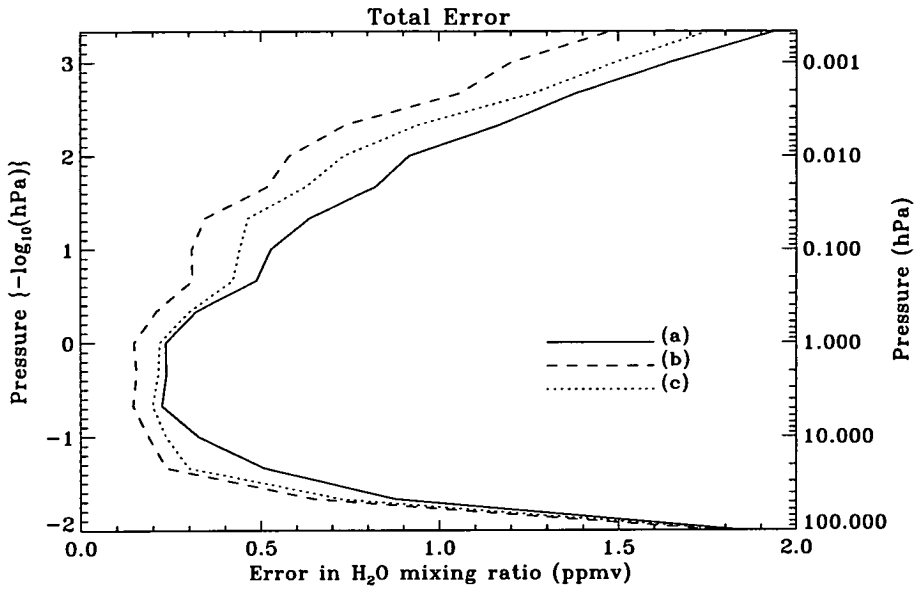

Figure 5.18: Total error for H_2O retrieval on nominal grid; (a) measurements on nominal MLS limb scan, (b) simulated measurements with integration time of 1.8 seconds on limb scan of resolution 1.5 km, (c) as for (b) but integration time of 0.4 seconds.

error in retrieved H_2O at 46 hPa and above and would also appear to improve the vertical resolution of the retrieval above 0.46 hPa and between 46 hPa and 4.6 hPa. However, as mentioned above, utilising such a limb scan would reduce the horizontal resolution of a retrieved profile by approximately three times. To maintain the same horizontal resolution as that obtained with the nominal scan, an integration time of 0.4 seconds for each limb view is required. Using measurements from such a limb scan would still improve both the retrieved error and the vertical resolution of the retrieval, but the improvement would not be as great.

5.3.2 Retrieval grid of resolution 2 x nominal

In this section the possibility of performing retrievals of H_2O on a grid of resolution twice that of the nominal grid, whilst using measurements from a limb scan of resolution 1.5 km, is investigated. This retrieval grid is defined in sec-

tion 5.2 and the high resolution limb scan is described above. Measurements with integration times of 1.8 seconds and 0.4 seconds are both considered. The *a priori* covariance matrix used in the calculations includes off-diagonal elements which assume the presence of inter-level correlations of length scale 5–6 km.

Figure 5.19 shows the resulting averaging kernels for the retrieval of H_2O using the simulated measurements with an integration time of 1.8 seconds on the high resolution limb scan. Comparing these averaging kernels with those

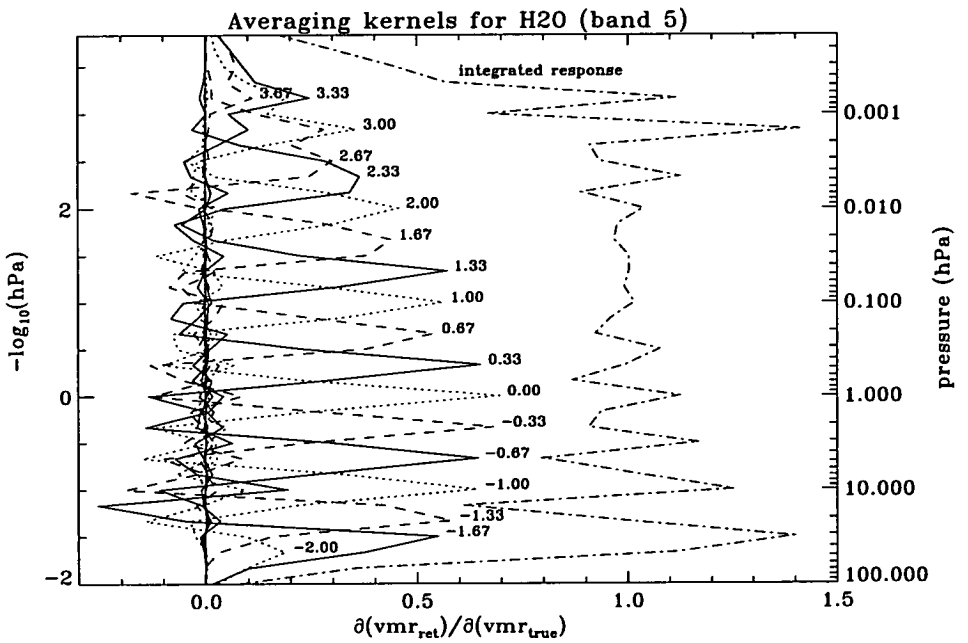

Figure 5.19: Averaging kernels for H_2O retrieval on a grid of twice the nominal resolution. Measurements from a limb scan of ~ 1.5 km resolution have been simulated. The integration time for each limb view is 1.8 seconds. A correlation length scale of 5–6 km has been assumed.

in figure 5.7 it can be seen that the overall effect of using measurements from the high resolution limb scan is to produce a small increase in the peak values of the averaging kernels. When measurements with an integration time of 0.4 seconds are used the averaging kernels (not shown) have peak values somewhere between those in figure 5.19 and those in figure 5.7.

As a measure of the vertical resolution of the retrievals, the full-width at

half-maximum, $\Delta_{\frac{1}{2}}$, is plotted in figure 5.20. The estimated retrieval error is plotted in figure 5.21. In both of these figures, the line labelled (a) corresponds to the case where measurements from the nominal MLS limb scan are used, the line labelled (b) corresponds to the case where simulated measurements with an integration time of 1.8 seconds on the high resolution limb scan are used, and the line labelled (c) corresponds to the case where simulated measurements similar to those for (b), but with an integration time of 0.4 seconds are used. In figure 5.20 it can be seen that using measurements with an in-

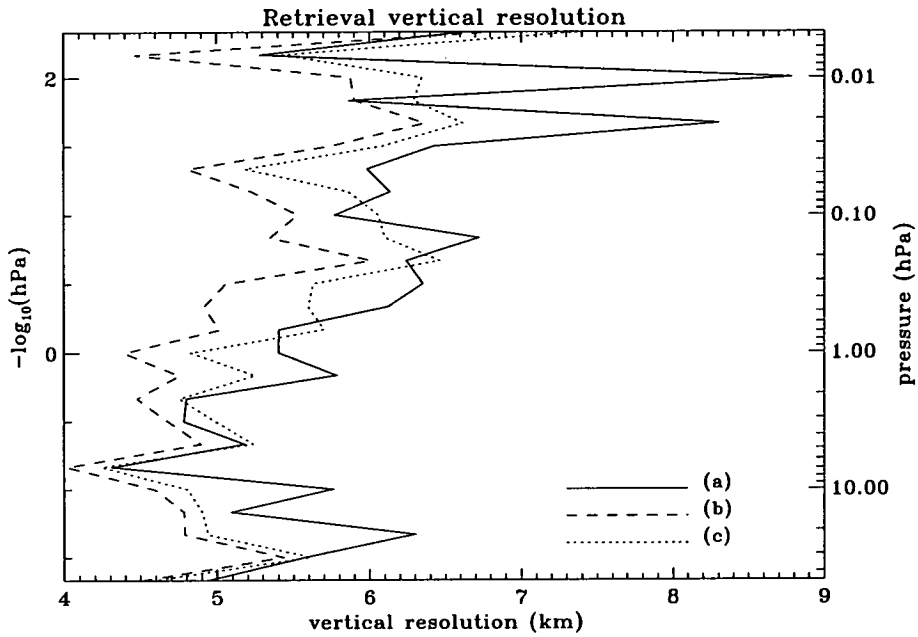

Figure 5.20: Vertical resolution of H_2O retrieval on a grid of twice the nominal resolution; (a) measurements on nominal MLS limb scan, (b) simulated measurements with integration time of 1.8 seconds on limb scan of resolution 1.5 km, (c) as for (b) but integration time of 0.4 seconds.

tegration time of 1.8 seconds on the high resolution limb scan gives a general improvement of up to 1 km in the vertical resolution of the retrieval between 46 hPa and 0.007 hPa. However, when the integration time of these measurements is reduced to 0.4 seconds, the improvement in vertical resolution is not so clear; there is some improvement, for example, between 30 hPa and 7 hPa and at 0.02 hPa and 0.01 hPa.

Using measurements on the high resolution limb scan, as opposed to the nominal MLS limb scan, reduces the smoothing error (not shown), this reduction being greater for measurements with an integration time of 1.8 seconds than for those with an integration time of 0.4 seconds. The error due to measurement noise (not shown) is reduced between 30 hPa and 0.001 hPa when the high resolution measurements with an integration time of 1.8 seconds are used instead of those from the nominal limb scan. When the integration time of the high resolution measurements is 0.4 seconds, the error due to measurement noise, below 0.002 hPa, is of a similar size to that which arises when measurements from the nominal limb scan are used.

Figure 5.21 shows the estimated total error for the retrieval of H_2O on a grid of resolution twice that of the nominal grid. It is evident that using mea-

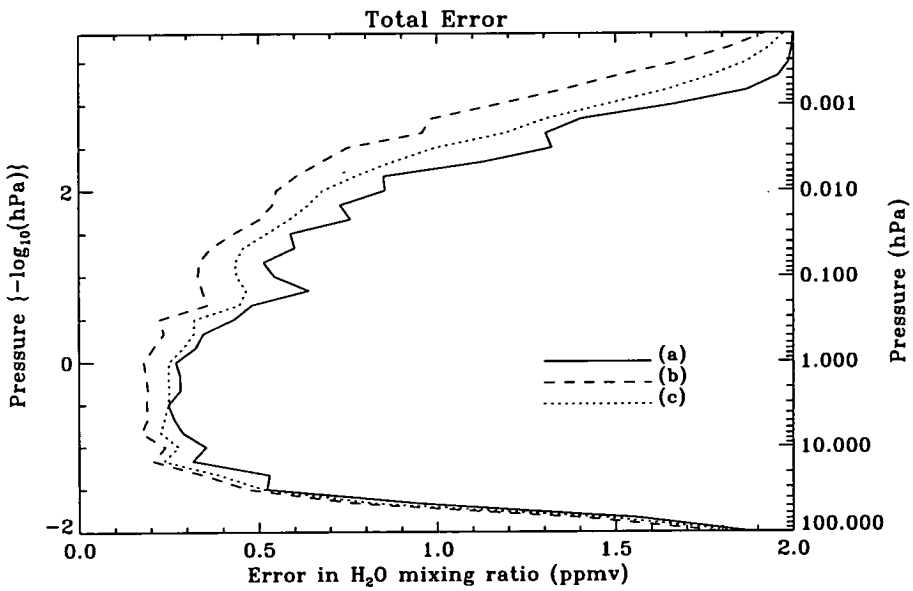

Figure 5.21: Total error for H_2O retrieval on a grid of twice the nominal resolution; (a) measurements on nominal MLS limb scan, (b) simulated measurements with integration time of 1.8 seconds on limb scan of resolution 1.5 km, (c) as for (b) but integration time of 0.4 seconds.

surements with an integration time of 1.8 seconds on the high resolution limb scan gives a significant reduction in the retrieved error. When the integration

time is decreased to 0.4 seconds, a reduction in retrieved error is still apparent, but is not as great due to the increased measurement noise resulting from the shorter integration time.

In summary, using measurements with an integration time of 1.8 seconds on the high resolution limb scan gives a general improvement of up to 1 km in the vertical resolution of the retrieval of H_2O on a grid of resolution twice that of the nominal grid and produces a significant reduction in the retrieved error. When the integration time of these high resolution measurements is reduced to 0.4 seconds, in order to maintain the nominal horizontal resolution of a retrieved profile, the resulting improvement in vertical resolution of the retrieval is not so clear, although there are improvements at some levels. A reduction in retrieved error, over the use of measurements from the nominal limb scan, is still evident, but is not as great as that which occurs when the integration time of the high resolution measurements is 1.8 seconds.

5.3.3 Retrieval grid of resolution 4 x nominal

In this section the possibility of retrieving H_2O on a grid of resolution four times that of the nominal grid using measurements on a limb scan of higher resolution than the nominal MLS scan is investigated. The retrieval grid is defined in section 5.2 and the high resolution limb scan is described above. Measurements with integration times of 1.8 seconds and 0.4 seconds are both considered. As in sections 5.3.1 and 5.3.2, the *a priori* covariance matrix contains non-zero off-diagonal elements which assume that inter-level correlations of length scale 5–6 km are present.

Figure 5.22 shows the resulting averaging kernels for the retrieval of H_2O on a grid of resolution four times that of the nominal grid using simulated measurements with an integration time of 1.8 seconds on the high resolution limb scan. These averaging kernels are similar to those in figure 5.11 but, on the whole, tend to have peak values that are slightly larger. The integrated response remains highly oscillatory and reaches a value of 2 at 8 hPa and at 0.0018 hPa. Thus, the whole retrieved profile greatly over-responds to pertur-

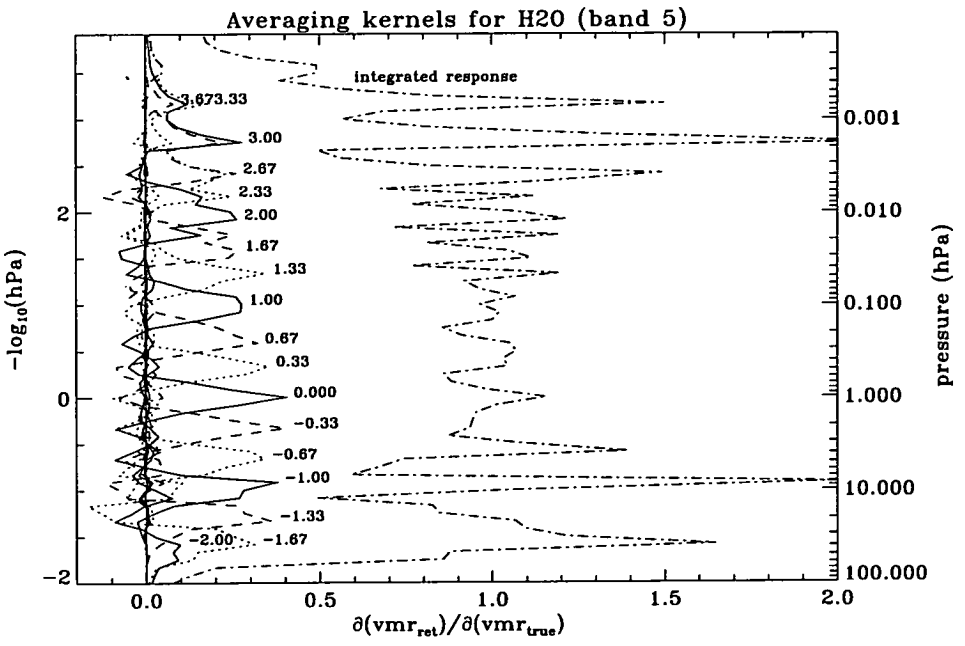

Figure 5.22: Averaging kernels for H_2O retrieval on a grid of four times the nominal resolution. Measurements from a limb scan of ~ 1.5 km resolution have been simulated. The integration time for each limb view is 1.8 seconds. A correlation length scale of 5–6 km has been assumed.

bations in H_2O at these two pressure levels. The averaging kernels for the case when the high resolution measurements have an integration time of 0.4 seconds (not shown) are similar to those of figure 5.22 with peak values reduced by a small amount.

The vertical resolution of the retrievals is plotted in figure 5.23 and the estimated retrieval error is plotted in figure 5.24. In both of these figures, the line labelled (a) corresponds to the case where measurements from the nominal MLS limb scan are used, the line labelled (b) corresponds to the case where simulated measurements with an integration time of 1.8 seconds on the high resolution limb scan are used, and the line labelled (c) corresponds to the case where measurements similar to those for (b), but with an integration time of 0.4 seconds, are used.

In figure 5.23 the vertical resolution is given by the full-width at half-maximum, $\Delta_{\frac{1}{2}}$, and is plotted over the range 46–0.1 hPa, where the averag-

ing kernels are reasonably well peaked functions. It can be seen that using

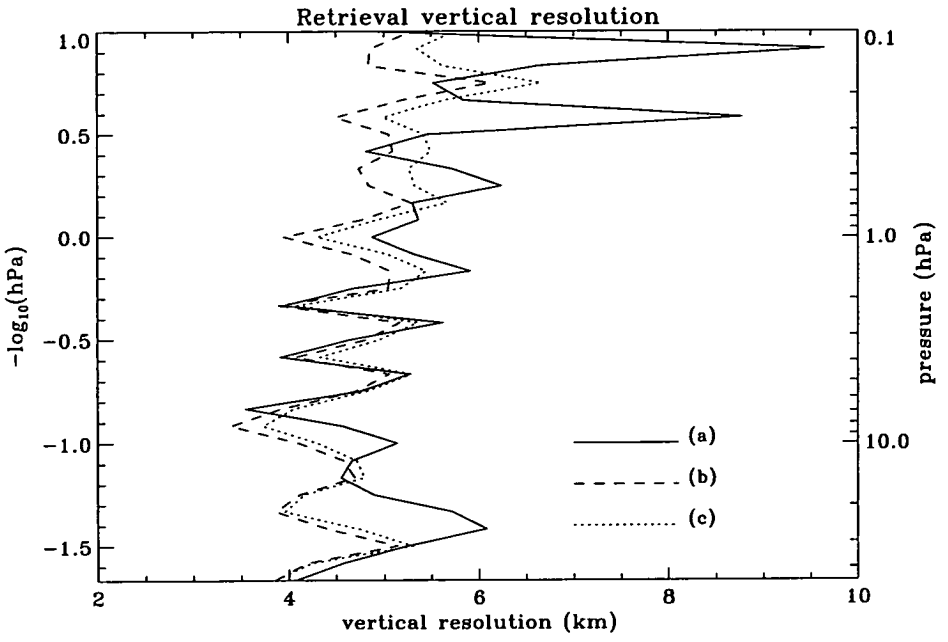

Figure 5.23: Vertical resolution of H_2O retrieval on a grid of four times the nominal resolution; (a) measurements on nominal MLS limb scan, (b) simulated measurements with integration time of 1.8 seconds on limb scan of resolution 1.5 km, (c) as for (b) but integration time of 0.4 seconds.

measurements from the high resolution limb scan in place of measurements from the nominal MLS scan gives some improvement to the vertical resolution of the retrieval between 30 hPa and 8 hPa and at most levels between 2 hPa and 0.1 hPa. The high resolution measurements with an integration time of 0.4 seconds give rise to a slightly poorer vertical resolution than the measurements with an integration time of 1.8 seconds. Although the separation of the retrieval levels is ~ 1.5 km, it appears that such a high vertical resolution is unattainable. This was also the case when using measurements from the nominal limb scan, even when no inter-level correlations were assumed which cause a certain amount of smoothing over the profile (see section 5.2).

The smoothing error (not shown) for the retrieval of H_2O on a grid of resolution four times that of the nominal grid is generally reduced over the whole profile when measurements on the high resolution limb scan are used

in place of the measurements from the nominal scan. For the high resolution measurements with an integration time of 0.4 seconds, the reduction in smoothing error is not as great as that with measurements having an integration time of 1.8 seconds, due to the shorter integration time resulting in an increase in measurement noise. This increase in measurement noise results in more weight being put on the *a priori* information which therefore increases the smoothing error. The error due to measurement noise (not shown), when the high resolution measurements with an integration time of 1.8 seconds are used in place of the measurements from the nominal limb scan, is reduced between 30 hPa and 0.001 hPa. When the high resolution measurements with an integration time of 0.4 seconds are used, the error due to measurement noise is similar to that produced by the measurements from the nominal limb scan. In figure 5.24 the estimated total error for the retrieval of H_2O on a grid of resolution four times that of the nominal grid, is plotted. It can be seen that

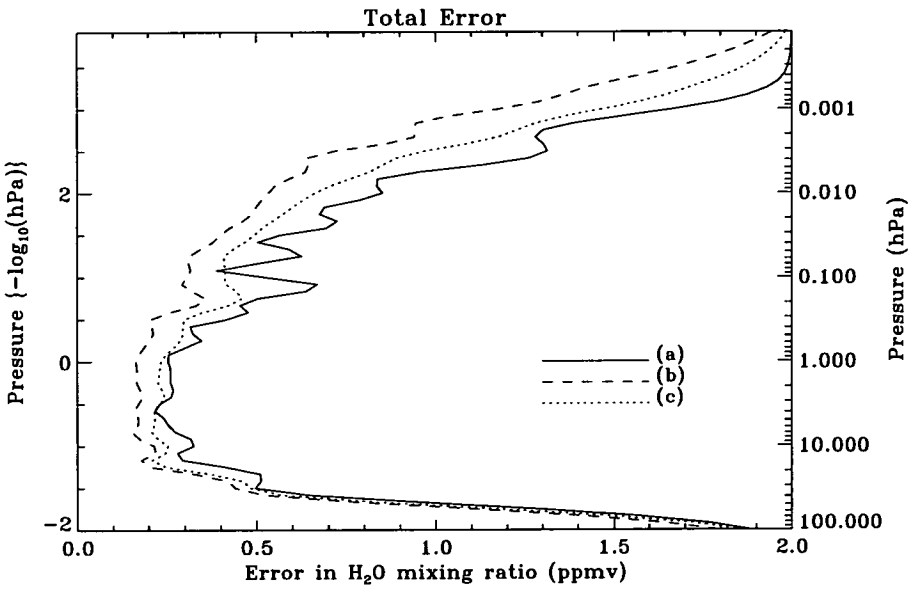

Figure 5.24: Total error for H_2O retrieval on a grid of four times the nominal resolution; (a) measurements on nominal MLS limb scan, (b) simulated measurements with integration time of 1.8 seconds on limb scan of resolution 1.5 km, (c) as for (b) but integration time of 0.4 seconds.

there is a general reduction in the retrieval error when the measurements on the high resolution limb scan are used in place of those from the nominal scan. However, when the high resolution measurements have an integration time of 0.4 seconds, this reduction in error is not as great as that which results when the measurements have an integration time of 1.8 seconds.

In summary, it appears that a vertical resolution of ~ 1.5 km is unattainable, even when the resolution of the limb scan is ~ 1.5 km. This may be expected as inter-level correlations with a length scale of 5–6 km were assumed which cause a certain amount of smoothing over the profile. However, it was found, in section 5.2.3, that in order to produce retrievals on a grid of resolution four times that of the nominal grid with errors significantly reduced from the *a priori* error, it is necessary to include inter-level correlations. By using measurements on the high resolution limb scan, the vertical resolution of the retrieval is improved between 30 hPa and 8 hPa and at most levels between 2 hPa and 0.1 hPa, but is rarely better than 4 km. Using the high resolution measurements also reduces the retrieval error; more so with measurements having an integration time of 1.8 seconds but at the expense of degrading the horizontal resolution of a profile by three times.

5.4 Discussion and Summary

In this chapter the possibility of retrieving H_2O at higher vertical resolution than nominal was investigated. Firstly, retrievals using measurements from the nominal MLS limb scan were studied. Such retrievals would only involve reprocessing of the existing data and would not require new measurements to be performed. In conjunction with this study, the effect of including information on inter-level correlations was investigated.

The off-diagonal elements of the *a priori* covariance matrix represent the believed covariance between different levels in the atmosphere for the quantity to be retrieved. For MLS Version 3 retrievals, these off-diagonal elements are set to zero, which assumes no knowledge of inter-level correlations. The

possibility of correlations being present between H_2O at different pressure levels was taken account of by including non-zero off-diagonal elements in the *a priori* covariance matrix. These elements were constructed using equation (5.1), which assumes that correlations are present with a Gaussian decay of specified length scale.

Two different correlation length scales were assumed; one of length $\frac{1}{6}$ [$-\log_{10}$(hPa)], which is equivalent to 2.5–3 km in height, and one of length $\frac{1}{3}$ [$-\log_{10}$(hPa)], which is equivalent to 5–6 km. It was found that, in general, assuming the presence of inter-level correlations tends to reduce the retrieval error but at the expense of a loss of vertical resolution. The longer the assumed correlation length scale, the greater was the reduction in error but also the greater was the loss of vertical resolution. This loss of vertical resolution is due to a certain amount of smoothing over the profile, as seen by the widening of the averaging kernels. These results are qualitatively consistent with those of other workers [*inter alia Backus and Gilbert, 1970, Conrath, 1972, Rodgers, 1976a, and Roscoe et al., 1992*] where a trade-off is found between resolution and retrieval error.

For the retrieval of H_2O on the nominal grid, assuming the presence of correlations with length scale of 5–6 km gave a reduction in the retrieval error, particularly above 0.1 hPa where the MLS measurements are separated by $\sim$ 6 km in height, with an associated small loss of vertical resolution. Retrievals on a grid of resolution twice that of the nominal grid were investigated. The levels of this retrieval grid are separated by 2.5–3 km in height. It was found that when no inter-level correlations were assumed or when a correlation length of 2.5–3 km was assumed, a vertical resolution of 3–4 km was possible in the range 15–0.7 hPa with a corresponding retrieval error of less than 1 ppmv. It appears that a vertical resolution 2.5–3 km is unattainable. For the retrieval of H_2O on a grid of resolution four times that of the nominal grid (separation of retrieval levels is $\sim$ 1.5 km), it appears that the assumption of the presence of inter-level correlations is necessary in order to produce a retrieval error which is sufficiently less than the *a priori* error. When a correlation length of 2.5–

3 km was assumed, a vertical resolution of 3–4 km was achieved over the range 15–2 hPa. Thus, it appears that there is no advantage in performing retrievals on a grid of resolution four times that of the nominal grid as the vertical resolution of the retrievals is no better than that achieved by retrieving on a grid of resolution twice that of the nominal grid.

The above discussion should be borne in mind when any future reprocessing of the MLS data is performed in order to attempt to retrieve H_2O to a higher vertical resolution.

Also in this chapter, an investigation into the possibility of using measurements from a limb scan of higher resolution than the nominal MLS scan was performed. In practice, this would involve performing measurements with a new scan pattern as opposed to simply reprocessing the existing data. At the time of writing, the 183 GHz radiometer was no longer functioning and so the results of this study may be more relevant to future instruments such as EOS MLS (Earth Observing System Microwave Limb Sounder), [*Waters, 1988*].

Two sets of measurements from a limb scan of resolution ~ 1.5 km were simulated. The first set of measurements having an integration time of 1.8 seconds for each limb view which is equivalent to that of the nominal scan but would lead to a loss of horizontal resolution from ~ 400 km to ~ 1300 km. The second set of measurements had an integration time of 0.4 seconds for each limb view. This integration time would be required in order to maintain a horizontal resolution of ~ 400 km for a retrieved profile using a limb scan of such a high vertical resolution. In the lower stratosphere, the nominal MLS limb scan has a vertical resolution of 1.5–2 km which is close to that of the simulated limb scan, but elsewhere the nominal scan is more sparse; 3–4 km resolution in the upper stratosphere and lower mesosphere and 6 km in the upper mesosphere. In this study the presence of inter-level correlations with a length scale of 5–6 km was assumed.

For the retrieval of H_2O on the nominal grid it was found that using measurements with an integration time of 1.8 seconds from a limb scan of vertical resolution ~ 1.5 km, in place of measurements from the nominal scan, would

appear to significantly reduce the retrieval error at 46 hPa and above and would also appear to improve the vertical resolution of the retrieval above 0.46 hPa and between 46 hPa and 4.6 hPa. If measurements with an integration time of 0.4 seconds from the high resolution limb scan were used, in order to maintain the horizontal resolution of a retrieved profile, a similar improvement in vertical resolution would be achieved with a lesser, but still significant, reduction in retrieval error.

Retrieving H_2O on a grid of twice the resolution of the nominal grid using measurements with an integration time of 1.8 seconds on the high resolution limb scan, in place of measurements from the nominal scan, would appear to give a general improvement of up to 1 km in the vertical resolution of the retrieval and result in a significant reduction in the retrieval error. However, when the integration time of the high resolution measurements was reduced to 0.4 seconds, the vertical resolution of the retrieval is degraded; at some levels there is still improvement over using measurements from the nominal scan while at other levels there is not much difference. However, a reasonable reduction in retrieval error was evident, but not as great as that when measurements with an integration time 1.8 seconds were used.

When considering the retrieval of H_2O on a grid of resolution four times that of the nominal grid, using measurements from a limb scan of resolution ~ 1.5 km, it appears that this level of vertical resolution is unattainable for the retrieved profile. Results of a brief study suggest that the FOV width may not be the limiting factor to the vertical resolution of the retrieval but that the uncertainties in other parameters, such as temperature and tangent pressure play an important role. In this brief study, averaging kernels and retrieval errors were evaluated for a retrieval similar to that in Section 5.3.3. The main differences being that no inter-level correlations were assumed for H_2O and the uncertainties in temperature and tangent pressure were reduced by 100 times. This led to a vertical resolution for the retrieval which oscillated between 1.8 km and 4 km in the range 46 hPa to 1 hPa, giving an average value of ~ 3 km, although, the resulting retrieval error oscillated between 1 ppmv and

1.7 ppmv which is not a large reduction from the *a priori* error. Thus, it would appear that retrievals with a vertical resolution somewhat narrower than the FOV width may be possible, but that the uncertainties in parameters, such as temperature and tangent pressure, may have to be unrealistically small in order to achieve such a vertical resolution.

Studies of the type described in this chapter should ideally be performed during the design of a remote sensing instrument in order to establish the required limb scan (both resolution and integration time) and suitable retrieval grid to achieve the desired vertical resolution and accuracy of the retrieved profile. In the work describe above, only the retrieval of H_2O was considered, but making changes to the resolution and integration time of measurements would also affect other retrieved quantities, such as temperature, ozone and chlorine monoxide, in the case of MLS.

Chapter 6

Discussion and Further Work

In this thesis, the method of characterisation and error analysis formalised by *Rodgers, [1990]* has been applied to the retrieval of H_2O from the radiance measurements of MLS band 5. Possible improvements to the H_2O retrieval were also investigated employing the above mentioned formal method as a diagnostic tool.

Characterisation and Error Analysis of MLS H_2O

In Chapter 3 a characterisation and error analysis of the UARS MLS 183 GHz H_2O retrieval was presented. A study of the averaging kernels suggested that the useful vertical range for the Version 3 H_2O retrievals is 46–0.01 hPa. However, due to known artefacts in the data, a restricted vertical range for useful scientific studies is given as 22-0.2 hPa at high latitudes and 46–0.2 hPa elsewhere. For this useful vertical range, the vertical resolution of the H_2O retrievals, given by the width of the averaging kernels, is 5–6 km. An error analysis was performed which produced estimates of the contributions of both random errors, including the smoothing error, and systematic uncertainties to the overall error in retrieved H_2O. From this analysis, a summary of the estimated precision and overall accuracy of the MLS Version 3 H_2O retrievals was presented (see Table 3.1). The estimated precision was given by the rss random error, excluding the smoothing error, from the formal error analysis. It was found that the rss random error was 0.1–0.2 ppmv larger than

the observed variability of the H_2O retrievals between 46 hPa and 5 hPa. This is thought to be due to the assumed error in tangent pressure which was used in the error analysis. This error was taken from typical errors in MLS retrieved tangent pressure which contain a systematic component. The precision estimate for H_2O should be recalculated using an estimate of the total random error in tangent pressure, and the comparison with the measured variability revisited.

Possible improvements to the retrieval of H_2O in the lower stratosphere

In Chapter 4, a problem with the retrieval of H_2O in the lower stratosphere at high latitudes during winter was highlighted. It was found that the retrievals at 46 hPa and 22 hPa contained an increased contribution from the *a priori* information at high latitudes during the polar winter and that the areas covered by these poor retrievals were highly correlated with the regions of cold air associated with the polar vortex. The increase in the contribution from the *a priori* information was found to be due to a corresponding loss of information from the radiance measurements. This was caused by the use of an opacity criterion which excludes from the retrieval any radiance measurements which are deemed to arise from limb paths of optical thickness greater than a prescribed critical value. The opacity criterion for the MLS Version 3 retrievals is independent of spectral channel. In an attempt to reduce the contribution from the *a priori* information, a channel-dependent opacity criterion was developed to allow radiance measurements in channels 1, 2, 14 and 15, arising from limb paths of greater optical thickness to be included in the retrieval.

For retrievals based on simulated radiances, the use of the new opacity criterion produced a substantial increase in the contribution from the measurements at both 46 hPa and 22 hPa, with an improved ability, at 46 hPa, to track the true mixing ratio. For retrievals based on MLS measured radiances, a similar increase in the contribution from the measurements was found to

be possible at both 46 hPa and 22 hPa. However, in some cases, a significant increase in the retrieved mixing ratio (up to 1 ppmv) at 22 hPa was found. This effect was not in evidence for the retrievals based on simulated radiances and needs more investigation to discover the exact cause of the increase. It is possible that the only effective solution to improving the H_2O retrievals in the lower stratosphere is the development of a nonlinear retrieval scheme.

Possibility of retrieving H_2O at higher vertical resolution

In Chapter 5 the possibility of retrieving H_2O at higher vertical resolution than nominal was investigated. Firstly, retrievals using measurements from the nominal MLS limb scan were studied. Such retrievals would only involve reprocessing of the existing data and would not require new measurements to be performed. In conjunction with this study, the effect of including information on possible inter-level correlations was investigated.

In general, it was found that assuming the presence of inter-level correlations tends to reduce the retrieval error but at the expense of a loss of vertical resolution. This was found to be consistent with the results of other workers.

When using measurements from the nominal MLS limb scan a vertical resolution of 3–4 km was attainable in the range 15–0.7 hPa with a corresponding retrieval error of less than 1 ppmv. A vertical resolution of less than 3 km was not attainable. This should be borne in mind when any future reprocessing of MLS data is performed.

An investigation into the possibility of using measurements from a limb scan of higher vertical resolution than that of the nominal MLS scan was performed. In practice, this would involve performing measurements with a new scan pattern as opposed to simply reprocessing the existing data. At the time of writing, the 183 GHz radiometer was no longer functioning and so the results of this study may be more relevant to future instruments.

Measurements from an MLS limb scan of vertical resolution ~ 1.5 km were simulated for this study. Using these measurements gave a significant reduction in the retrieval error at 46 hPa and above and also improved the vertical

resolution of the retrieval above 0.46 hPa and between 46 hPa and 4.6 hPa. It appears that a retrieval with vertical resolution comparable with the high resolution limb scan is unattainable.

This study should be taken further to investigate the effects of the FOV width on the vertical resolution of the retrievals. This would involve simulating radiances and evaluating influence functions from the forward model assuming various FOV widths, then evaluating the corresponding averaging kernels. The vertical resolution of the retrieval being derived from the width of the averaging kernels.

In this thesis it has been shown that the formal method of characterisation and error analysis is not only an important technique in estimating the precision and accuracy of retrieved profiles from remote measurements, but can also be used to great effect as a diagnostic tool in investigating problems with retrievals and exploring the possibilities of various retrieval scenarios. Ideally, the types of analyses described above should, if possible, be performed during the design stage of an instrument to investigate the effects of various instrument parameters on the desired retrieved quantity, and also to compare the results of various potential retrieval techniques.

Appendix A

Transformation of Optimal Estimation Equations

This appendix explains the transformation of equations (2.14) and (2.15) into equations (2.16) and (2.17), respectively.

Equation (2.14) gives the optimal estimate of the state vector as

$$\hat{\mathbf{x}} = (\mathbf{S}_a^{-1} + \mathbf{K}^T\mathbf{S}_\epsilon^{-1}\mathbf{K})^{-1}(\mathbf{S}_a^{-1}\mathbf{x}_a + \mathbf{K}^T\mathbf{S}_\epsilon^{-1}\mathbf{y}) \tag{A.1}$$

Multiplying both sides of (A.1) on the left by $(\mathbf{S}_a^{-1} + \mathbf{K}^T\mathbf{S}_\epsilon^{-1}\mathbf{K})$ gives

$$(\mathbf{S}_a^{-1} + \mathbf{K}^T\mathbf{S}_\epsilon^{-1}\mathbf{K})\hat{\mathbf{x}} = (\mathbf{S}_a^{-1}\mathbf{x}_a + \mathbf{K}^T\mathbf{S}_\epsilon^{-1}\mathbf{y}) \tag{A.2}$$

Rearranging (A.2) gives

$$\mathbf{S}_a^{-1}(\hat{\mathbf{x}} - \mathbf{x}_a) + \mathbf{K}^T\mathbf{S}_\epsilon^{-1}\mathbf{K}\hat{\mathbf{x}} = \mathbf{K}^T\mathbf{S}_\epsilon^{-1}\mathbf{y} \tag{A.3}$$

Subtracting $\mathbf{K}^T\mathbf{S}_\epsilon^{-1}\mathbf{K}\mathbf{x}_a$ from both sides of (A.3) gives

$$(\mathbf{S}_a^{-1} + \mathbf{K}^T\mathbf{S}_\epsilon^{-1}\mathbf{K})(\hat{\mathbf{x}} - \mathbf{x}_a) = \mathbf{K}^T\mathbf{S}_\epsilon^{-1}(\mathbf{y} - \mathbf{K}\mathbf{x}_a) \tag{A.4}$$

Rearranging (A.4) gives

$$\hat{\mathbf{x}} = \mathbf{x}_a + (\mathbf{S}_a^{-1} + \mathbf{K}^T\mathbf{S}_\epsilon^{-1}\mathbf{K})^{-1}\mathbf{K}^T\mathbf{S}_\epsilon^{-1}(\mathbf{y} - \mathbf{K}\mathbf{x}_a) \tag{A.5}$$

Now note that

$$\begin{aligned}(\mathbf{S}_a^{-1} + \mathbf{K}^T\mathbf{S}_\epsilon^{-1}\mathbf{K})\mathbf{S}_a\mathbf{K}^T &= \mathbf{K}^T + \mathbf{K}^T\mathbf{S}_\epsilon^{-1}\mathbf{K}\mathbf{S}_a\mathbf{K}^T \\ &= \mathbf{K}^T\mathbf{S}_\epsilon^{-1}(\mathbf{S}_\epsilon + \mathbf{K}\mathbf{S}_a\mathbf{K}^T)\end{aligned} \tag{A.6}$$

Multiplying each side of (A.6) by $(\mathbf{S}_a^{-1} + \mathbf{K}^T\mathbf{S}_\epsilon^{-1}\mathbf{K})^{-1}$ on the left and by $(\mathbf{S}_\epsilon + \mathbf{K}\mathbf{S}_a\mathbf{K}^T)^{-1}$ on the right gives

$$\mathbf{S}_a\mathbf{K}^T(\mathbf{S}_\epsilon + \mathbf{K}\mathbf{S}_a\mathbf{K}^T)^{-1} = (\mathbf{S}_a^{-1} + \mathbf{K}^T\mathbf{S}_\epsilon^{-1}\mathbf{K})^{-1}\mathbf{K}^T\mathbf{S}_\epsilon^{-1} \tag{A.7}$$

Now, substituting (A.7) into (A.5) gives

$$\hat{\mathbf{x}} = \mathbf{x}_a + \mathbf{S}_a\mathbf{K}^T(\mathbf{K}\mathbf{S}_a\mathbf{K}^T + \mathbf{S}_\epsilon)^{-1}(\mathbf{y} - \mathbf{K}\mathbf{x}_a) \tag{A.8}$$

This is the form of the solution expressed in equation (2.16).

The error covariance is given in (2.15) by

$$\hat{\mathbf{S}} = (\mathbf{S}_a^{-1} + \mathbf{K}^T\mathbf{S}_\epsilon^{-1}\mathbf{K})^{-1} \tag{A.9}$$

Multiplying both sides of (A.9) by $(\mathbf{S}_a^{-1} + \mathbf{K}^T\mathbf{S}_\epsilon^{-1}\mathbf{K})$ gives

$$\hat{\mathbf{S}}(\mathbf{S}_a^{-1} + \mathbf{K}^T\mathbf{S}_\epsilon^{-1}\mathbf{K}) = \mathbf{I} \tag{A.10}$$

where $\mathbf{I}$ is the identity matrix. (A.10) can be rewritten as

$$\hat{\mathbf{S}}(\mathbf{I} + \mathbf{K}^T\mathbf{S}_\epsilon^{-1}\mathbf{K}\mathbf{S}_a)\mathbf{S}_a^{-1} = \mathbf{I} \tag{A.11}$$

Now multiplying both sides of (A.11) on the right by $\mathbf{S}_a$ gives

$$\hat{\mathbf{S}}(\mathbf{I} + \mathbf{K}^T\mathbf{S}_\epsilon^{-1}\mathbf{K}\mathbf{S}_a) = \mathbf{S}_a \tag{A.12}$$

Multiplying out the brackets in (A.12) and rearranging gives

$$\hat{\mathbf{S}} = \mathbf{S}_a - \hat{\mathbf{S}}\mathbf{K}^T\mathbf{S}_\epsilon^{-1}\mathbf{K}\mathbf{S}_a \tag{A.13}$$

Replacing $\hat{\mathbf{S}}$, on the right-hand side of (A.13), by the expression for $\hat{\mathbf{S}}$ in (A.9) gives

$$\hat{\mathbf{S}} = \mathbf{S}_a - (\mathbf{S}_a^{-1} + \mathbf{K}^T\mathbf{S}_\epsilon^{-1}\mathbf{K})^{-1}\mathbf{K}^T\mathbf{S}_\epsilon^{-1}\mathbf{K}\mathbf{S}_a \tag{A.14}$$

Now substituting (A.7) into (A.14) gives

$$\hat{\mathbf{S}} = \mathbf{S}_a - \mathbf{S}_a\mathbf{K}^T(\mathbf{K}\mathbf{S}_a\mathbf{K}^T + \mathbf{S}_\epsilon)^{-1}\mathbf{K}\mathbf{S}_a \tag{A.15}$$

This is the form of the error covariance given in equation (2.17).

References

Backus, G.E., and J.F. Gilbert, Uniqueness in the inversion of inaccurate gross Earth data, *Philos. Trans. R. Soc. London, Ser. A 266*, 123–192, 1970.

Baldecchi, M., B. Carli, F. Mencaraglia, A. Bonetti, and M. Carlotti, Atlas of stratospheric submillimeter lines: 1. The 7–20 cm^{-1} interval, *J. Geophys. Res. 89*, 11689–11704, 1984.

Baldecchi, M., B. Carli, F. Mencaraglia, A. Barbos, A. Bonetti, and M. Carlotti, Atlas of stratospheric submillimeter lines: 2. The 20–40 cm^{-1} interval, *J. Geophys. Res. 93*, 5303–5318, 1988.

Barath, F.T., M.C. Chavez, R.E. Cofield, D.A. Flower, M.A. Frerking, M.B. Gram, W.M. Harris, J.R. Holden, R.F. Jarnot, W.G. Kloezeman, G.J. Klose, G.K. Lau, M.S. Loo, B.J. Maddison, R.J. Mattauch, R.P. McKinney, G.E. Peckham, H.M. Pickett, G. Siebes, F.S. Soltis, R.A. Suttie, J.A. Tarsala, J.W. Waters, and W.J. Wilson, The Upper Atmosphere Research Satellite Microwave Limb Sounder instrument, *J. Geophys. Res. 98*, D6, 10751–10762, 1993.

Bauer, A., M. Godon, M. Kheddar, and J.M. Hartmann, Temperature and perturber dependences of water vapor line-broadening. Experiments at 183 GHz; calculations below 1000 GHz, *J. Quant. Spectrosc. Radiat. Transfer 41*, No. 1, 49–54, 1989.

Bevilacqua, R.M., W.J. Wilson, W.B. Ricketts, P.R. Schwartz, and R.J. Howard, Possible seasonal variability of mesospheric water vapor, *Geophys. Res. Lett. 12*, 397–400, 1985.

Bevilacqua, R.M., W.J. Wilson, and P.R. Schwartz, Measurements of mesospheric water vapor in 1984 and 1985: results and implications for middle atmospheric transport, *J. Geophys. Res. 92*, D6, 6679–6690, 1987.

Brasseur, G., and S. Solomon, *Aeronomy of the Middle Atmosphere*, D. Reidel Publishing Co., Dordrecht, 1984.

Chandrasekhar, S., *Radiative Transfer*, New York: Dover Publications, 1960

Conrath, B.J., Vertical resolution of temperature profiles obtained from remote radiation measurements, *J. Atmos. Sci. 29*, 1262–1271, 1972.

Deepak, A. (ed.), *Inversion Methods in Atmospheric Remote Sounding*, Academic Press, New York, 1977.

Deepak, A., H.E. Fleming, and M.T. Chahine (eds.), *Advances in Remote Sensing Retrieval Methods*, A. Deepak Publishing, Hampton, Virginia, 1985.

Drummond, J.R., J.T. Houghton, G.D. Peskett, C.D. Rodgers, M.J. Whale, J. Whitney, and E.J. Williamson, The stratospheric and mesospheric sounder on Nimbus 7, *Proc. Roy. Soc. London, Ser. A 296*, 219–241, 1980.

Farman, J., B. Gardiner, and J. Shanklin, Large losses of total ozone in Antarctica reveal seasonal ClO_x/NO_x interaction, *Nature 315*, 207–210, 1985.

Fishbein, E.F., W.G. Read, L. Froidevaux, and J.W. Waters, Validation of temperature and pressure measurements by the Upper Atmosphere Research Satellite Microwave Limb Sounder, *J. Geophys. Res.*, submitted, 1994.

Gandrud, B.W., J.E. Dye, D. Baumgardner, G.V. Ferry, M. Loewenstein, K.R. Chan, L. Sanford, B. Gary, and K. Kelly, The January 30, 1989 Arctic polar stratospheric clouds (PSC) event: evidence for a mechanism of dehydration, *Geophys. Res. Lett. 17*, No. 4, 457–460, 1990.

Gille, J.C., P.L. Bailey, and J.M. Russell, Temperature and composition measurements from LRIR and LIMS experiments on Nimbus 6 and 7, *Phil. Trans. Roy. Soc. London, Ser. A 296*, 205–218, 1980.

Goyette, T.M. and F.C. De Lucia, The pressure broadening of the $3_{1,3}$–$2_{2,0}$ transition of water between 80 K and 600 K, *J. Mol. Spectroscopy 143*, No. 2, 346–358, 1990.

Houghton, J.T., Taylor, F.W., and Rodgers, C.D., *Remote Sounding of Atmospheres*, Cambridge University Press, 1984.

Jarnot, R.F., R.E. Cofield, G.E. Peckham, and J.W. Waters, Calibration of UARS MLS, *J. Geophys. Res.*, submitted, 1994.

Kelly, K.K., A.F. Tuck, D.M. Murphey, M.H. Proffitt, D.W. Fahey, R.L. Jones, D.S. McKenna, M. Loewenstein, J.R. Podolske, S.E. Strahan, G.V. Ferry, K.R. Chan, J.F. Vedder, G.L. Gregory, W.D. Hypes, M.P. McCormick, E.V. Browell, and L.E. Heidt, Dehydration in the lower Antarctic stratosphere during late winter and early spring, 1987, *J. Geophys. Res. 94*, D9, 11317–11357, 1989.

Lahoz, W.A., M.R. Suttie, L. Froidevaux, R.S. Harwood, C.L. Lau, T.A. Lungu, G.E. Peckham, H.C. Pumphrey, W.G. Read, Z. Shippony, R.A. Suttie, J.W. Waters, G.E. Nedoluha, S.J. Oltmans, J.M. Russell III, and W.A. Traub, Validation of UARS MLS 183 GHz H_2O measurements, *submitted to J. Geophys. Res.*, 1994.

Le Texier, H., S. Solomon, and R.R. Garcia, The role of molecular hydrogen in the water vapour budget of the stratosphere, *Q. J. Roy. Met. Soc. 114*, 281–295, 1988.

Manney, G.L., L. Froidevaux, J.W. Waters, R.W. Zurek, W.G. Read, L.S. Elson, J.B. Kumer, J.L. Mergenthaler, A.E. Roche, A. O'Neill, R.S. Harwood, I. MacKenzie, and R, Swinbank, Chemical depletion of ozone in the Arctic lower stratosphere during winter 1992–93, *Nature 370*, 429–434, 1994.

MAP, J.J. Barnett, and M. Corney, Handbook for Middle Atmosphere Program (MAP), SCOSTEP Secretariat, University of Illinois, Urbana, USA, 1989.

Meeks, M.L., Essentials of radiometric measurements, in *Methods of Experimental Physics, 12B*, (L. Meeks, ed.), 1–6, Academic Press, New York, 1976.

Menke, W., *Geophysical Data Analysis: Discrete Inverse Theory*, Academic Press, San Diego, Calif., 1984.

Molina, M., and F. Rowland, Stratospheric sink for chlorofluoromethanes: chlorine atom catalysed destruction of ozone, *Nature 249*, 810–812, 1974.

Molina, M., T. Tso, L. Molina, and F. Wang, Antarctic stratospheric chemistry of chlorine nitrate, hydrogen chloride, and ice: release of active chlorine, *Science 238*, 1253–1260, 1987a.

Molina, L.T., and M.J. Molina, Production of Cl_2O_2 from the self-reaction of the ClO radical, *J. phys. Chem 91*, 433–436, 1987b.

Mood, A.M., F.A. Graybill, and D.C. Boes, *Introduction to the Theory of Statistics*, McGraw-Hill International Editions, 1974.

Mote, P.W., K.H. Rosenlof, J.R. Holton, R.S. Harwood, and J.W. Waters, Seasonal variations of water vapor in the tropical lower stratosphere, *Geophys. Res. Lett. 22*, No. 9, 1093–1096, 1995.

Peckham, G., An optimum calibration procedure for radiometers, *Int. J. Remote Sens. 10*, 227–236, 1989.

Pickett, H., and A. Chiou, Folded fabry-perot quasi-optical ring resonator diplexer: theory and experiment, *IEEE Trans. Microwave Theory Tech. MT-31*, 373–380, 1983.

Pickett, H.M., R.L. Poynter, and E.A. Cohen, Submillimeter, millimeter and microwave spectral line catalog, Technical report 8023, Revision 3, Jet Propulsion Laboratory, 1992.

Proffitt, M.H, J.J. Margitan, K.K. Kelly, M. Loewenstein, J.R. Podolske, K.R. Chan, Ozone loss in the Arctic polar vortex inferred from high altitude aircraft measurements, *Nature 347*, 31–36, 1990.

Read, W.G., J.W. Waters, L. Froidevaux, D.A. Flower, R.F. Jarnot, D.L. Hartmann, R.S. Harwood, and R.B. Rood, Upper tropospheric water vapor from UARS MLS, *Bull. Amer. Met. Soc.*, submitted, 1994.

Reber, C.A., C.E. Trevathan, R.J. McNeal, and M.R. Luther, The Upper Atmosphere Research Satellite (UARS) Mission, *J. Geophys. Res. 98*, 10643–10647, 1993.

Remsberg, E.E., J.M. Russell III, and C.-Y. Wu, An interim reference model for the variability of the middle atmosphere water vapor distribution, *Adv. Space Res. 10*, 51–64, 1990.

Robbins, D., J. Waters, P. Zimmermann, R. Jarnot, J. Hardy, H. Pickett, S. Pollitt, W. Traub, K. Chance, N. Louisnard, W. Evans, and J. Kerr, Ozone measurements from the balloon intercomparison campaign, *J. Atmos. Chem. 10*, 181–218, 1990.

Roche, A.E., J.B. Kumer, J.L. Mergenthaler, G.A. Ely, W.G. Uplinger, J.F. Potter, T.C. James, and L.W. Sterritt, The Cryogenic Limb Array Etalon Spectrometer (CLAES) on UARS: Experiment description and performance, *J. Geophys. Res. 98*, 10763–10775, 1993.

Rodgers, C.D., The vertical resolution of remotely sounded temperature profiles with *a priori* statistics, *J. Atmos. Sci. 33*, 707–709, 1976a.

Rodgers, C.D., Retrieval of atmospheric temperature and composition from remote measurements of thermal radiation, *Rev Geophys. and Space Phys. 14*, 609–624, 1976b.

Rodgers, C.D., Characterization and error analysis of profiles retrieved from remote sounding measurements, *J. Geophys. Res. 95*, D5, 5587–5595, 1990.

Roscoe, H.K., D.R. Barber, D.J. Oldham, and J.A.C. Squires, Vertical resolution of upward-looking atmospheric remote sensors – I. Performance of hypothetical instruments with well-behaved input kernels, *J. Quant. Spectrosc. Radiat. Transfer 48*, No. 4, 363–375, 1992.

Russell III, J.M., J.C. Gille, E.E. Remsberg, L.L. Gordley, P.L. Bailey, H. Fischer, A. Girard, S.R. Drayson, W.F.J. Evans, and J.E. Harries, Validation of water vapor results measured by the Limb Infrared Monitor of the Stratosphere (LIMS) experiment on NIMBUS 7, *J. Geophys. Res. 89*, D4, 5115–5124, 1984.

Santee, M.L., W.G. Read, J.W. Waters, L. Froidevaux, G.L. Manney, D.A. Flower, R.F. Jarnot, R.S. Harwood, and G.E. Peckham, Interhemispheric differences in polar stratospheric HNO_3, H_2O, ClO, and O_3, *Science 267*, 849–852, 1995.

Shimazaki, T., *Minor Constituents in the Middle Atmosphere*, D. Reidel Publishing Co., 1985.

Solomon, S., Progress towards a quantitative understanding of Antarctic ozone depletion, *Nature 347*, 347–354, 1990.

Taylor, F.W., C.D. Rodgers, J.G. Whitney, S.T. Werret, J.J Barnett, G.D. Peskett, P. Venters, J. Ballard, C.W.P. Palmer, R.J. Knight, P.E. Morris, and T.J. Nightingale, Remote sensing of atmospheric structure and composition by pressure modulator radiometry from space: The ISAMS experiment on UARS, *J. Geophys. Res. 98*, 10799–10814, 1993

Townes, C.H., and A.L. Schawlow, *Microwave Spectroscopy*, Dover Publications Inc., 1975.

Tsou, J-J., J.J. Olivero, and C.L. Croskey, Study of variability of mesospheric H_2O during spring 1984 by ground-based microwave radiometric observations, *J. Geophys. Res. 93*, D5, 5255–5266, 1988.

Turco, R.P., O.B. Toon, and P. Hamill, Heterogeneous physicochemistry of the polar ozone hole, *J. Geophys. Res. 94*, 16493–16510, 1989.

Waters, J.W., Absorption and emission by atmospheric gases, in *Methods of Experimental Physics, 12B*, (L. Meeks, ed.), 142–176, Academic Press, New York, 1976.

Waters,J., J. Gustincic, R. Kakar, H. Roscoe, P. Swanson, T.G. Phillips, T. DeGraauw, A. Kerr, and R. Mattauch, Aircraft search for millimeter wavelength emission by stratospheric ClO, *J. Geophys. Res. 84*, 6934–7049, 1979.

Waters, J., J. Gustincic, P. Swanson, and A. Kerr, Measurements of upper atmospheric H_2O emission, in *Atmospheric Water Vapor*, Wilkerson and Ruhnke, eds., Academic Press, New York, 229–240, 1980.

Waters, J., J. Hardy, R. Jarnot, and H. Pickett, Chlorine monoxide radical, ozone, and hydrogen peroxide: stratospheric measurements by microwave limb sounding, *Science 214*, 61–64, 1981.

Waters, J., J. Hardy, R. Jarnot, H. Pickett, and P. Zimmermann, A balloon-borne microwave limb sounder for stratospheric measurements, *J. Quant. Spectrosc. Radiat. Transfer 32*, 407–433, 1984.

Waters, J., R. Stachnik, J. Hardy, and R. Jarnot, ClO and O_3 stratospheric profiles: balloon microwave measurements, *Geophys. Res. Lett. 15*, 780–783, 1988a.

Waters, J.W., A proposal for the Earth Observing System Microwave Limb Sounder, submitted to NASA A.O. No. OSSA-1-88, 1988b.

Waters, J.W., Submillimeter-wavelength heterodyne spectroscopy and remote sensing of the upper atmosphere, *Proc. IEEE 80*, 11, 1679–1701, 1992.

Waters, J.W., Microwave Limb Sounding, in *Atmospheric Remote Sensing by Microwave Radiometry*, (M.A. Janssen, ed.), ch. 8, John Wiley & Sons, New York, 1993.

Waters, J.W., L. Froidevaux, W.G. Read, G.L. Manney, L.S. Elson, D.A. Flower, R.F. Jarnot, and R.S. Harwood, Stratospheric ClO and ozone from the Microwave Limb Sounder on the Upper Atmosphere Research Satellite, *Nature 362*, 597–602, 1993.

World Meteorological Organisation (WMO) Report, No. 20, vol. 1, 1990.